DIGITAL ACCESS TO SCHOLARSHIP AT HARVARD
DASH.HARVARD.EDU

HARVARD LIBRARY
Office for Scholarly Communication

Magnetism, Reactivity and Metal Ion Lability in Trigonal Iron Clusters

Citation

Eames, Emily. 2012. Magnetism, Reactivity and Metal Ion Lability in Trigonal Iron Clusters. Doctoral dissertation, Harvard University.

Permanent link

http://nrs.harvard.edu/urn-3:HUL.InstRepos:9548613

Terms of Use

This article was downloaded from Harvard University's DASH repository, and is made available under the terms and conditions applicable to Other Posted Material, as set forth at http://nrs.harvard.edu/urn-3:HUL.InstRepos:dash.current.terms-of-use#LAA

Share Your Story

The Harvard community has made this article openly available.
Please share how this access benefits you. Submit a story .

Accessibility

© 2012 - Emily V Eames
All rights reserved.

Dissertation Advisor: Professor Theodore A. Betley Emily V Eames

Magnetism, Reactivity and Metal Ion Lability in Trigonal Iron Clusters

Abstract

Important reactions are catalyzed by enzymes employing polynuclear cofactors, often characterized by weak-field ligands and transition metal ions within the sum of the van der Waals radii. While the overall stoichiometries and, in many cases, the structures, of the cofactors are known, the roles of the individual metal ions remain uncertain. Our approach is to investigate model clusters stabilized by a hexadentate, trinucleating ligand. The hexaamine ligand (MeC $(CH_2NHC_6H_4$-*o*-$NHPh)_3$) ($^{Ph}LH_6$) allows facile synthesis of the clusters ($^{Ph}L)Fe_3(thf)_3$, ($^{Ph}L)Fe_3(py)_3$, and ($^{Ph}L)Fe_3(PMe_2Ph)_3$ (thf = tetrahydrofuran, py = pyridine). The phenyl substituents on the ligand sterically prevent strong M–M bonding, but permit weaker M–M orbital interactions, with Fe–Fe distances near those found in Fe metal. The complex ($^{Ph}L)Fe_3(thf)_3$ exhibits a well-isolated $S = 5$ or $S = 6$ ground state over 5 - 300 K, as evidenced by magnetic susceptibility and reduced magnetization data. However, in the stronger-field pyridine and phosphine complexes, temperature dependent susceptibility is observed which is best modeled as a spin state transition from $S = 2$ to $S = 4$. Variable-temperature crystallography and Mössbauer spectroscopy reveal a whole-molecule, rather than site-isolated, spin transition.

The all-ferrous cluster ($^{Ph}L)Fe_3(thf)_3$ can be oxidized with triphenylmethyl halides or iodine to give singly-oxidized clusters of the form ($^{Ph}L)Fe_3X(L)$ and $[(^{Ph}L)Fe_3(\mu\text{-}X)]_2$ (X = Cl, Br, I; L = thf, py), in which one Fe–Fe distance contracts to 2.30 Å and the others lengthen to

2.6-2.7 Å. The halide and solvent ligands coordinate a unique Fe, but Mössbauer spectroscopy shows that the diiron pair bears the oxidation. Magnetic data can be modeled by considering a high-spin ferrous ion ferromagnetically coupled to an $S = {}^{3}/_{2}$ $[Fe_2]^{5+}$ unit. When $[(^{Ph}L)Fe_3(\mu\text{-}Cl)]_2$ is reacted with two or five equivalents of $CoCl_2$ in tetrahydrofuran, the fully-substituted complexes $(^{Ph}L)Fe_2CoCl(acn)$ and $(^{Ph}L)FeCo_2Cl(acn)$ (acn = acetonitrile) can be isolated. ^1H nuclear magnetic resonance shows that they are distinct species, not a mixture, and the elemental ratios are confirmed by X-ray fluorescence spectroscopy. Mössbauer spectroscopy shows that the Co preferentially substitutes into the $[M_2]^{5+}$ unit, as the ferrous site doublet is completely absent in $(^{Ph}L)FeCo_2Cl(acn)$.

Table of Contents

List of Figures

List of Tables

List of Equations

$$\chi = \frac{\boldsymbol{M}}{\boldsymbol{H}}$$

Equation 1.1

$$\chi T = \frac{N\mu_B^2}{3k_B} g^2 S(S+1)$$

Equation 1.2

$$\hat{H} = DS_z^2 + E(S_x^2 - S_y^2)$$

Equation 1.3

$$\hat{H} = -2J(\boldsymbol{S}_1 \cdot \boldsymbol{S}_2)$$

Equation 1.4

$$\hat{H} = -2J(\boldsymbol{S}_{\mathrm{Fe1}}\boldsymbol{S}_{\mathrm{Fe2}} + \boldsymbol{S}_{\mathrm{Fe2}}\boldsymbol{S}_{\mathrm{Fe3}} + \boldsymbol{S}_{\mathrm{Fe1}}\boldsymbol{S}_{\mathrm{Fe3}}) + D\boldsymbol{S}^2 + g\mu_{\mathrm{B}}\boldsymbol{S}\cdot\boldsymbol{B}$$

Equation 2.1

$$\hat{H} = D\hat{S}_z^2 + E(\hat{S}_x^2 - \hat{S}_y^2) + g\mu_{\mathrm{B}}\boldsymbol{S}\cdot\boldsymbol{B}$$

Equation 2.2

$$\hat{H} = -2[J_1(\boldsymbol{S}_{\mathrm{Fe1}}\boldsymbol{S}_{\mathrm{Fe2}} + \boldsymbol{S}_{\mathrm{Fe2}}\boldsymbol{S}_{\mathrm{Fe3}}) + J_2\boldsymbol{S}_{\mathrm{Fe1}}\boldsymbol{S}_{\mathrm{Fe3}}] + D\boldsymbol{S}^2 + g\mu_{\mathrm{B}}\boldsymbol{S}\cdot\boldsymbol{B}$$

Equation 2.3

$$\hat{H} = -2(J_1\boldsymbol{S}_{\mathrm{Fe1}}\boldsymbol{S}_{\mathrm{Fe2}} + J_2\boldsymbol{S}_{\mathrm{Fe2}}\boldsymbol{S}_{\mathrm{Fe3}} + J_3\boldsymbol{S}_{\mathrm{Fe1}}\boldsymbol{S}_{\mathrm{Fe3}}) + D\boldsymbol{S}^2 + g\mu_{\mathrm{B}}\boldsymbol{S}\cdot\boldsymbol{B}$$

Equation 2.4

$$x = \frac{1}{1 + \exp[(\Delta H / R)(1/T - 1/T_C)]}$$

Equation 2.5

$$x = \frac{\chi T - (\chi T)_{LS}}{(\chi T)_{HS} - (\chi T)_{LS}}$$

Equation 2.6

$$\begin{gathered}
\phi(\omega) \propto \frac{(\Gamma/2 + \lambda)A - (\omega - p_1\varepsilon_2 - p_2\varepsilon_1)B}{A^2 + B^2} + \frac{(\Gamma/2 + \lambda)A' - (\omega - p_1\varepsilon'_2 - p_2\varepsilon'_1)B'}{A'^2 + B'^2} \\
A = (\omega - \varepsilon_1)(\omega - \varepsilon_2) - \Gamma/2(\Gamma/2 + \lambda) \\
A' = (\omega - \varepsilon'_1)(\omega - \varepsilon'_2) - \Gamma/2(\Gamma/2 + \lambda) \\
B = (\Gamma + \lambda)\omega - \Gamma/2(\varepsilon_1 + \varepsilon_2) - \lambda(p_1\varepsilon_1 + p_2\varepsilon_2) \\
B' = (\Gamma + \lambda)\omega - \Gamma/2(\varepsilon'_1 + \varepsilon'_2) - \lambda(p_1\varepsilon'_1 + p_2\varepsilon'_2) \\
\varepsilon_1 = S_1 + \Delta_1/2 \\
\varepsilon'_1 = S_1 - \Delta_1/2 \\
\varepsilon_2 = S_2 + \Delta_2/2 \\
\varepsilon'_2 = S_2 - \Delta_2/2
\end{gathered}$$

Equation 2.7

$\hat{H} = -2J(\boldsymbol{S}_1\boldsymbol{S}_2) + \Sigma D_i\boldsymbol{S}_i^2 + g\mu_B\boldsymbol{S}\cdot\boldsymbol{B}$ Equation 3.1

$\hat{H} = -2J_1(\boldsymbol{S}_{1_a}\boldsymbol{S}_{2_a} + \boldsymbol{S}_{1_b}\boldsymbol{S}_{2_b}) - 2J_2(\boldsymbol{S}_{1_a}\boldsymbol{S}_{1_b}) + \Sigma D_i\boldsymbol{S}_i^2 + g\mu_B\boldsymbol{S}\cdot\boldsymbol{B}$ Equation 3.2

$\hat{H} = -2J(\boldsymbol{S}_1\boldsymbol{S}_2) + \Sigma D_i\boldsymbol{S}_i^2 + g\mu_B\boldsymbol{S}\cdot\boldsymbol{B}$ Equation 4.1

List of Schemes

Abbreviations used

°	degrees in measure of angles
°C	degrees Celsius
^{1}H	hydrogen-1
^{57}Fe	iron-57
Å	Angstrom, 10^{-10} meters
acn	acetonitrile
Anal. Calcd.	elemental analysis calculated
av	average
$\boldsymbol{B}$	applied magnetic field
bipy	2,2'-bipyridine
BM	Bohr magneton
cm^{-1}	inverse centimeters or wavenumbers
D	axial zero-field splitting parameter
E	rhombic zero-field splitting parameter
equiv.	equivalents
FWHM	full width at half maximum
G	Gauss
g	g-factor
g	gram
$\boldsymbol{H}$	applied magnetic field
h	hour
$\hat{H}$	Hamiltonian operator
$^{H}LH_6$	$MeC(CH_2NHPh\text{-}o\text{-}NH_2)_3$
HOMO	highest occupied molecular orbital

Hz	hertz
IR	infrared
J	magnetic exchange coupling parameter
K	degrees Kelvin
k_B	Boltzmann constant
kHz	kilohertz
L	dative ligand for a transition metal
LUMO	lowest unoccupied molecular orbital
M	magnetization
M	general metal
Me	methyl
Mes	mesityl
mg	milligram
MHz	megahertz
min	minute
ml	milliliter
mmol	millimole
MO	molecular orbital
mol	mole
MPMS	magnetic properties measurement system
MS	mass spectrometry
M_{sat}	saturation magnetization
mT	millitesla
N	Avogadro’s number
NIR	near infrared
nm	nanometer
NMR	nuclear magnetic resonance

o-	*ortho* position on aryl ring
ODPA	*ortho*-phenylenediamine
Ph	phenyl
$^{Ph}LH_6$	$MeC(CH_2NHPh$-*o*-$NHPh)_3$
ppm	parts per million
py	pyridine
R	general alkyl or aryl
rt	room temperature
s	second
S	spin
SCO	spin crossover
SOMO	singly-occupied molecular orbital
SQUID	superconducting quantum interference device
T	Tesla
T	temperature
TBA	tetrabutylammonium
$^{tbs}LH_6$	1,3,5-$C_6H_9(NPh$-*o*-$NHSi^tBuMe_2)_3$
T_C	critical temperature
thf	tetrahydrofuran
TMS	trimethylsilyl
UV-vis	ultraviolet-visible
V	volume
VSM	vibrating sample magnetometer
VT	variable-temperature
X	anion ligand for a transition metal
XRD	X-ray diffraction

XRF	X-ray fluorescence
Γ	linewidth, full width at half maximum
δ	isomer shift or chemical shift
$\lvert\Delta E_Q\rvert$	quadrupole splitting
ΔH	change in enthalpy
ε	extinction coefficient
λ	wavelength
λ_{max}	wavelength of maximum absorbance in UV-vis spectroscopy
μ_{B}	Bohr magneton
μ_{eff}	effective magnetic moment
μ^n-A	bridging atom to n metal centers
ν	energy
χ	molar magnetic susceptibility

Acknowledgements

Many thanks to everyone who aided or encouraged me. First, my adviser Ted, for being so supportive and inspirational. You have a gift for sharing your passion for science, but beyond that, I learned so much more from you than I ever expected, and I'll never forget what you showed me about teaching and leading. To all of the Betley lab, past and present, you have been wonderful labmates and it has been a privilege to work with you. Kin, you were the kindest, most helpful and relentlessly good-natured person I could have imagined, and the best mentor. Evan, I have rarely admired anyone more than you. Alison, you have been a wonderful scientific resource, and your camaraderie has kept me sane for the last year at least. Mat and Dave (and Danna!), thank you for sharing your expertise with me, it was tremendously valuable. Graham, Tamara, Libby, Austin, Raul, Danielle, Matt, Benji and Denise, you have been great company and great labmates. The wondergrads, especially Guy, Max, Chris, Art, Dianne, Daphne, and Doug—it wouldn't have been the same without you. Shao, thank you for all your help and patience! Thank you to all the CCB staff, interacting with you was always a pleasure, even when I had to confess to accidentally busting holes in the wall!

Ann, you were an amazing adviser, and you were right that you can do worse than get a PhD when you are not quite sure what you want. Arthur, thank you for your patience and for sharing so many skills. Mr. Samp, Mrs. Mili, Ms. Levinstein—the PhD is probably all Mr. Samp's fault, but you all helped set me up. To my friends, you helped keep me cheerful. Mama and Papa, I have always said you were perfect. I love you, and thank you for everything, not least encouraging me to stick with it. Dan, you are my love, and you made it all worthwhile. Here's to something completely different, together!

Chapter 1: Background on the Study of Weak-Field Clusters with Direct Metal-Metal Interaction

1.1 Introduction

The study of weak-field transition metal clusters remains a critical frontier in inorganic chemistry. On a fundamental level, the types of interaction possible between open-shell metal atoms have only begun to be explored. On the practical side, precedent in heterogenous and enzyme catalysis suggests that metal clusters have the potential to facilitate many complex and important reactions using relatively abundant, inexpensive and environmentally benign first-row metals. In particular, manipulations of small molecules, including hydrogen, nitrogen, and oxygen, methane, and waste gases such as carbon dioxide and NO_x, are of particular importance to supplying society's energy needs and maintaining environmental quality. Metal clusters may also find application as magnetic materials, for use as medical imaging reagents or in data storage. Understanding the fundamental properties and reactivity of clusters should assist in the rational design of materials and catalysts, providing substantial benefits to society.

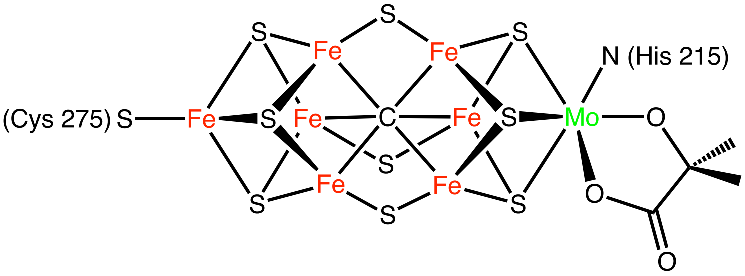

Figure 1.1. Structure of the FeMo cofactor of nitrogenase.[2] Fe-Fe distances 2.57 - 2.67 Å; Fe-Mo distances 2.67 - 2.72 Å.

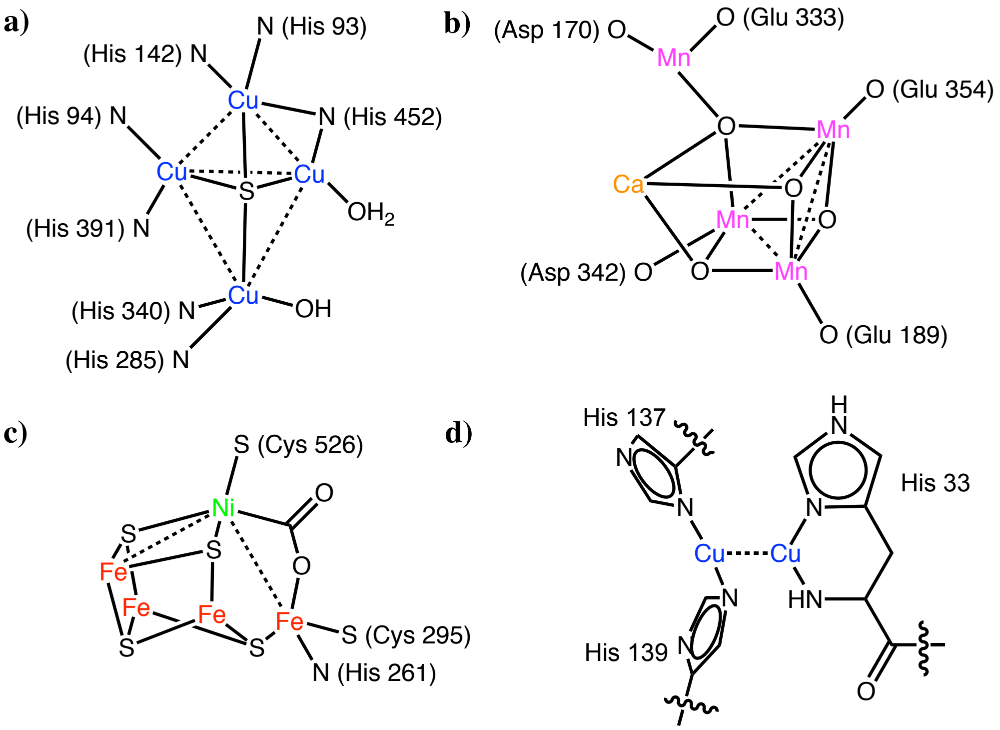

Figure 1.2. Proposed structures of enzyme active sites (metal-metal separations indicated by dotted lines). a) N_2O reductase[11] (2.44 - 3.65 Å); b) PSII OEC[13] (2.65 - 2.72 Å); c) CODH[6] (2.76 - 2.79 Å); d) pMMO[9] (2.60 Å).

1.2 Cluster Catalysis in Enzymes

Polynuclear cofactors serve as the catalytic sites in many enzymes, including the ubiquitous and diverse FeS clusters,[1] the mixed metal clusters of nitrogenase[2-4] and carbon monoxide dehydrogenase,[5-7] the copper sites of the particulate methane monooxygenase[8,9] and N_2O reductase,[10,11] and the MnO cluster of Photosystem II.[12,13] While nature accomplishes very challenging chemistry with the relatively abundant and environmentally benign first row metals, the complexity of metal uptake, regulation and chaperone systems[14-17] suggests the hypothesis that where polynuclear cofactors are used, each metal has an essential role. The essential contributions of multiple metals likely include allowing different substrate binding modes, providing an electron reservoir, and facilitating binding and activation of inert substrates.[18,19]

However, despite intense investigation, the precise roles of the metal atoms and how they modulate each other's activity are unknown.

Nature uses polynuclear cofactors to overcome particular kinetic challenges, including activation of inert substrates and selective oxidation of substrates prone to overoxidation. Many of these challenging reactions also involve coordinating the movements of multiple protons and electrons. For instance, the enzyme nitrogenase converts elemental nitrogen to bioavailable ammonia. While the overall reaction is thermodynamically favorable, dinitrogen is kinetically inert. The reaction requires six protons and electrons, but biologically eight protons and electrons are required. Additionally, (depending on the mechanism) the catalyst may be required to bind and stabilize both π-acids (e.g. N_2) and π-bases (e.g. nitride). These requirements suggest that the flexibility of a metal cluster may be valuable as an electron reservoir and to accommodate a variety of ligand types, perhaps through several binding modes. The active site for this reaction is indeed a large cofactor containing Fe and usually Mo or V. The most active form appears to be a $Fe_7MoS_9(\mu^6\text{-}C)$ cluster, called the FeMo cofactor.[2,4,20] Nitrogenase is particularly difficult to study. The reaction requires the coordination of many components: FeMo protein, the Fe protein (which binds repeatedly to the FeMo protein to provide one reducing equivalent), 16 equivalents of ATP, and eight protons and electrons. Additionally, nitrogen does not bind until several reducing equivalents have been added, but absent nitrogen, the protein can reduce protons rather than maintaining its reduced state. Accordingly, there has been a great deal of debate over the substrate binding site and mechanism, with some favoring Mo (for which there is mononuclear precedent in nitrogen fixation[21,22]) and others favoring Fe. No intermediates have been crystallographically identified, though based on alternative substrate and site-specific mutagenesis studies some researchers have proposed that both nitrogenous and alkyne substrates bind to a particular FeS face.[3]

Other examples of demanding reactions catalyzed by polynuclear cofactors have much in common with the nitrogenase chemistry. The oxygen-evolving complex (OEC) of Photosystem II catalyzes the formation of molecular oxygen using a Mn_4CaO_4 complex.[12,13] This is a four electron process requiring a very large driving force, and the mechanism by which the two oxygen atoms are coupled is not well understood. Particulate methane monooxygenase (pMMO) catalyzes the controlled oxidation of methane to methanol. While this reaction is thermodynamically favorable, the MMOs stand alone in their ability to halt the reaction at methanol, rather than over-oxidizing to CO_2. The active site of pMMO has recently been identified as a dicopper center.[8,9] Other multinuclear enzyme cofactors include the NiFe clusters of carbon monoxide dehydrogenase,[5-7] which catalyzes the reversible transformation of CO to CO_2, as well as the tetracopper site of nitrous oxide reductase.[10,11] Taken together, these enzymes control many of the key processes of the global C, N and O cycles, as well as crucial chemical energy storage processes. Fully understanding their mechanisms could help us manage our waste products and better provide for our energy needs.

Of the enzyme cofactors discussed above, most fall into the general category of weak-field clusters, suggesting that there is particular catalytic utility in groups of open-shell metals. (A notable exception is hydrogenase, which employs strong-field CO and cyanide ligands.[23,24]) Moreover, in contrast to synthetic weak-field clusters, which typically have fairly large metal-metal distances, there is evidence that many enzymes use metals within van der Waals[25] contact of each other. In fact, many of the distances illustrated in Figure 1.1 and 1.2 are within the covalent radii,[26] though not so short as to suggest multiple bonding. Unfortunately, due to the current range of synthetic model complexes available, we have very little precedent to judge what the van der Waals radii of metals are (the Cambridge Structural Database (http://www.ccdc.cam.ac.uk/products/csd/radii/) still uses the van der Waals radii proposed by Bondi[25] in 1964, but this publication does not provide values for many transition elements) and even less understanding of the effects of metal atoms sharing orbital overlap but lacking strong bonds. This suggests a need for model chemistry to illuminate the particular properties of open-shell metal centers with weak contact or weak bonds, as well as further investigation of the catalytic roles of each metal.

1.3 Molecular Magnetism

Magnetochemistry is the study of the magnetic behavior of molecular species, as opposed to extended solids. Bulk ferromagnets rely on three-dimensional lattice interactions to maintain magnetization; if any individual atomic spin flips, unfavorable interactions with its neighbors result in a higher-energy state. In discrete molecules, magnetized states are generally transient, with molecules ordering at lower temperatures in the presence of applied fields and randomizing again when the field is removed or the complex heated. This property is called paramagnetism. In quantitative terms, an applied field $\boldsymbol{H}$ induces a magnetization $\boldsymbol{M}$ proportional to the susceptibility χ of the material

$$\chi = \frac{\boldsymbol{M}}{\boldsymbol{H}} \qquad \text{Equation 1.1}$$

The susceptibility is in general a function of the temperature, and in molecular magnetism there is often a simple inverse relationship, known as Curie behavior. In transition metal complexes, interesting magnetic properties can be observed in both mononuclear and multinuclear environments.[27]

1.3.1 Mononuclear complexes. High-spin transition metal complexes are paramagnetic. Prototypical complexes contain a fixed number of unpaired electrons, which give rise to a spin magnetic moment. If orbital angular momentum is not quenched by the ligand field, this will contribute to the magnetic moment, but in most complexes it can be ignored. In current usage, magnetic data are usually reported as χT values, which can be related to the total spin S by

$$\chi T = \frac{N\mu_B^2}{3k_B} g^2 S(S+1) \qquad \text{Equation 1.2}$$

where k_B is the Boltzmann constant, N is Avogadro's number, μ_B is the Bohr magneton, and g is the g-factor. Accordingly, a plot of χT vs. T for a typical paramagnet will be horizontal over most of the temperature range. Usually a decrease is observed at low temperature arising from weak intermolecular interactions or zero-field splitting.

Zero-field splitting arises where $S > 1/2$. For example, if $S = 2$, the M_S states are 0, ±1, ±2. These states can mix with excited states through spin-orbit coupling to different extents, thus splitting their energies even in the absence of an applied field. Zero-field splitting is generally largest in low nuclearity compounds, and in elements below the first transition series. The phenomenological zero-field splitting Hamiltonian is

$$\hat{H} = DS_z^2 + E(S_x^2 - S_y^2) \qquad \text{Equation 1.3}$$

where D is the axial zero-field splitting parameter and E is the rhombic splitting parameter. Zero-field splitting is usually a relatively weak effect, noticeable at low temperatures. However, it can result in magnetic anisotropy, leading to various effects. Qualitatively, positive D describes an easy plane of magnetization, while negative D describes an easy axis. In extreme cases, large negative *D* can result in a measurable barrier to spin flipping, allowing a particular magnetic state to persist in a single molecule in the absence of a magnetic field. For instance, an effective spin-reversal barrier of 42 cm^{-1} has been observed in a tris(pyrrolylmethyl)amine Fe(II) complex, making this the first example of a single-molecule magnet based on a single transition metal ion.[28] Single molecule magnets so far discovered have spin-inversion barriers too small for any practical application, but this is an active area of research. More generally, magnetic anisotropy can cause particles to reorient themselves in a magnetic field (called torquing, which can cause artifacts in magnetic data) and if particles are physically restrained, it can prevent magnetization values reaching the full theoretical maximum at low temperatures.

A different temperature-dependent behavior can be observed in complexes where the *d*-orbital splitting is relatively small, comparable to the electron pairing energy. In such cases, a transition can occur from high-spin to low-spin as the temperature is lowered and the entropy contribution to the Gibbs free energy decreases. This is observed as a change in the effective magnetic moment, either abrupt or gradual, and is termed spin crossover (SCO). In addition to the magnetic data, SCO is often studied by variable-temperature (VT) crystallography, as high-spin metal ions are larger than low spin; heat capacity measurements, where a spike will be observed at the transition temperature; and VT Mössbauer spectroscopy if Fe is involved, as high-spin and low-spin Fe exhibit dramatically different isomer shift and quadrupole splitting. Among the first molecules known to exhibit spin crossover, $Fe(bipy)_2(NCS)_2$, (bipy = 2,2'-bipyridine) shows Fe-N bond contractions of 0.07-0.15 Å and distinct Mössbauer parameters between its $S = 2$ and $S = 0$ state.[29,30]

1.3.2 Polynuclear complexes. When more than one metal center is present, the interactions between the individual ion spins become important. There are three principle types of interaction. Magnetic superexchange coupling describes interactions between metal spins mediated by bridging ligands. Superexchange can be either ferromagnetic, resulting in parallel spin alignment and larger magnetic moments, or antiferromagnetic, resulting in antiparallel spin alignment and leading to a reduced or diamagnetic spin ground state. Superexchange is described by the Heisenberg-Dirac-Van-Vleck Hamiltonian

$$\hat{H} = -2J(\boldsymbol{S}_1 \cdot \boldsymbol{S}_2) \qquad \text{Equation 1.4}$$

where J is the coupling parameter. Whether an interaction is ferromagnetic or antiferromagnetic is determined by orbital overlap considerations. If both metals interact with a single ligand orbital, coupling will tend to be antiferromagnetic; if they interact with orthogonal orbitals, it will be ferromagnetic. The strength of the interaction will depend on the balance of orbital interactions and the length of the bridge. Practically speaking, when data is modeled using an exchange coupling Hamiltonian, the origins of the effect are irrelevant, and only the net effect is considered.

Where more than two metals are present, more complex interactions are possible. In the case of a triangular arrangement of antiferromagnetically coupled $S = {}^1/_2$ spins, all three interactions cannot be simultaneously satisfied. This leads to a degeneracy of the ground state called spin frustration. Properly speaking, when the spins are greater than ${}^1/_2$, the degeneracy is no longer present as the spins are not isotropic and can take orientations other than up and down.[31] However, such situations are still commonly described as spin-frustrated. Superexchange coupling can be applied in a conceptually straightforward (if more computationally intensive) manner to larger clusters, sometimes yielding very large spin ground states. Such molecules include the first recognized single molecule magnets, since the spin-flipping barrier is proportional to S^2.[32]

The second type of magnetic interaction is called double exchange or spin-dependent delocalization.[33,34] Double exchange occurs in mixed-valent species that are strongly coupled, and it is mediated by the itinerant electron. When the two ions' spins are aligned, the itinerant electron can move between them without flipping its spin, which leads to a ferromagnetic coupling much stronger than superexchange. This is often observed in FeS clusters.[1,35]

The final possible type of interaction is direct coupling though orbital overlap, and it has received very little attention, likely because weak-field clusters rarely have direct metal-metal interactions. In cases where such interactions are present, the compound is usually treated as having a single molecular spin corresponding to the number of unpaired electrons in the molecular orbital (MO) manifold.[36,37]

1.3.3 Measurement Techniques. Molecular magnetism can be studied by the Evans' method[38] in standard NMR instruments or with a Guoy balance, but the greatest versatility is provided by the magnetometers based on the superconducting quantum interference device (SQUID). SQUID magnetometers are capable of measuring small changes in current through a loop as a magnetic sample is moved through it. Magnetometers are generally equipped with temperature control over a large range (1.8 - 350 K) and can generate applied fields up to 7 T. Two types of experiments are employed here. Susceptibility measurements involve scanning the temperature (e.g. over 5 - 300 K) at a particular applied field (e. g. 1,000 - 20,000 G). Data are typically presented as χT vs. T plots. Susceptibility data reveal the types of magnetic behavior present: spin crossover and antiferromagnetic coupling will cause a decrease in χT with temperature, while ferromagnetic coupling or torquing will manifest as an increase in χT. The shape of a downturn at low temperature can give some indication of D, though this is not a reliable way to determine zero-field splitting parameters.

The second type of measurement is reduced magnetization, which consists of scans over 1.8 - 10 K at fields from 1 - 7 T and is the best way to determine the spin ground state. Reduced magnetization is generally presented as isofield curves plotted as magnetization vs. H/T, showing saturation behavior. In the absence of magnetic anisotropy, the isofield curves will be superimposable and reach a maximum of $M_{\mathrm{sat}} = gS$. If anisotropy is present, the curves will not be superimposable and will saturate at a lower value. Simulations of reduced magnetization data can suggest values of J, D and S.[39,40]

1.4 Synthetic Clusters

Transition metal clusters traditionally consist of three to twenty or more metal atoms supported by one or more organic (or inorganic main-group) ligands. Here cluster is used to mean a specific, uniform molecular species, rather than a mixture of similar species or nanoparticles. Dinuclear species are included in this discussion despite not falling within the definition because they provide relevant precedent in metal-metal interaction and cooperation. “Naked” clusters containing only metal atoms have been studied in the gas phase and in specialized matrices, as well as by theory, but are not stable in solution and are not considered further.[41,42]

Metal clusters occupy a position between mononuclear coordination or organometallic complexes and bulk (or nanoscale) materials. Like nanoscale materials (which are generally larger and less uniform), metal clusters have properties distinct from the bulk material, and they often display semiconductor-like band structures at mid-range nuclearity, before reaching a metallic state at high nuclearity.[43] Like mononuclear transition metal complexes, they consist of metal atoms surrounded by a coordination sphere of ligands, which determines both electronic properties and reactivity. In both mononuclear and multinuclear complexes, a distinction is made between strong-field ligands, which cause a large splitting of the metal *d* orbitals and lead to low-spin electronic ground states, and weak-field ligands, which support more labile and reactive high-spin complexes. In dinuclear or polynuclear complexes, the strength of the metal-metal interactions can vary over a wide range, from metals that are well separated and fully isolated electronically, to those that communicate solely through ligands, to the extremely strong metal-metal multiple bonds exemplified by the Cr family. The complexes that have received the most attention to date fall into three general types: metal-metal multiply-bonded species; strong-field clusters, particularly CO clusters; and weak-field clusters such the FeS cofactors and single-molecule magnets.

1.4.1 Metal-Metal Multiple Bonds. Metal-metal multiple bonds have been studied extensively, and have reached the status of an inorganic "functional group" having a recognizable, predictable structure and behavior, analogous to organic functional groups.[44,45] Such interactions are most common in the early- and mid-transition metals, and the strength of the interaction depends in a predictable way on the *d* electron count of the metals, reaching a maximum at five *d* electrons, as this allows five filled bonding MOs and five empty anti-bonding

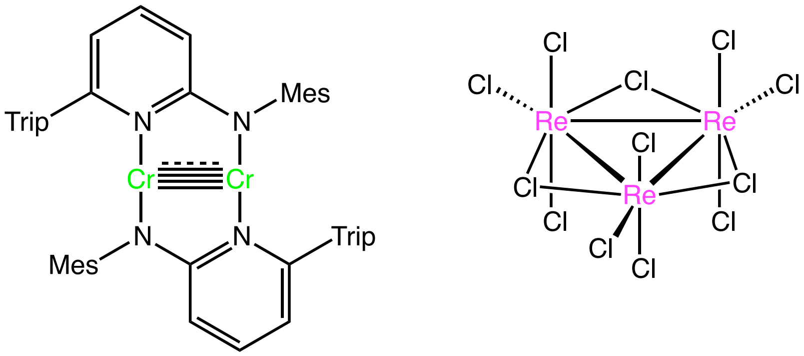

Figure 1.3. Metal-metal multiple bonds. (left) proposed Cr-Cr quintuple bond.[46] (right) $[Re_3Cl_{12}]^{3-}$ anion with Re-Re double bonds.[45]

MOs. For this reason the Cr group are ideal to form the strongest bonds, with Cr specifically proposed to exhibit quintuple bonds.[46] Experimentally, metal-metal bond strengths, as measured by bond distances in crystal structures, have been observed to increase when electrons are added to bonding MOs or removed from antibonding MOs and *vice versa*, as predicted by the MO model.[45] While such complexes provide compelling evidence of previously unknown bonding interactions (δ bonds, quadruple bonds) and a beautiful demonstration of the predictive power of MO theory, their bond strength renders them both stable and inert, and they are nearly always low spin.

1.4.2 Strong-Field Clusters. A substantial fraction of the transition metal clusters in the Cambridge Structural Database contain the classic strong-field ligand CO. CO confers low-spin,

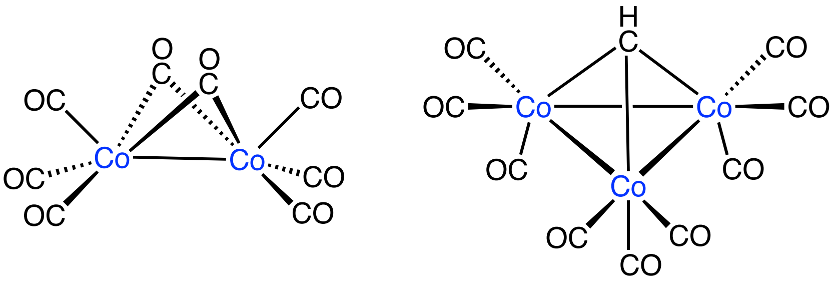

Figure 1.4. Catalytically active cobalt carbonyl clusters. (left) Pauson-Khand catalyst.[47] (right) Sugihara catalyst.[48]

closed-shell states with predictable structure. Short intermetallic distances are common, and metal-metal bonds are invoked to achieve 18-electron configurations. However, carbonyl clusters are among the few examples of metal-metal single bonds: the presence of π-acceptor ligands tends to preclude the formation of metal-metal multiple bonds.[45] The strong bonds make strong-field clusters fairly stable and convenient to work with.

Carbonyl clusters, particularly larger clusters of the second- and third-row transition metals, have been extensively studied for catalytic activity as analogues to heterogenous catalysts.[43] However, it is extremely difficult to tell, when catalytic activity is observed, whether the active species is an intact cluster, or a mononuclear or particulate species formed by decomposition of the cluster. Clusters have been extensively investigated as precursors for mononuclear or heterogenous catalysts, and have found some use. A notable example of first-row cluster catalysis is the Pauson-Khand reaction, in which a dicobalt complex catalyzes a [2+2+1] cyclization to form cyclopentenones.[47] Tricobalt complexes have also been shown to catalyze [2+2+2] cyclizations to form substituted benzenes.[48] As a rule, these complexes tend to engage in two-electron chemistry, and are used for organic transformations rather than small molecule chemistry. Strong-field ligands are quite uncommon in biological catalysis, with hydrogenase[23,24] being a notable exception.

1.4.3 Weak-Field Clusters. The final class, weak-field clusters, encompasses a great variety of both structure and function. The weak ligand fields have several general effects, principally more complex magnetic behaviour and an increase in lability and reactivity due to the number of unpaired electrons in antibonding MOs. Accordingly, weak-field clusters are much more challenging to synthesize and work with.[49,50] A perhaps accidental commonality among

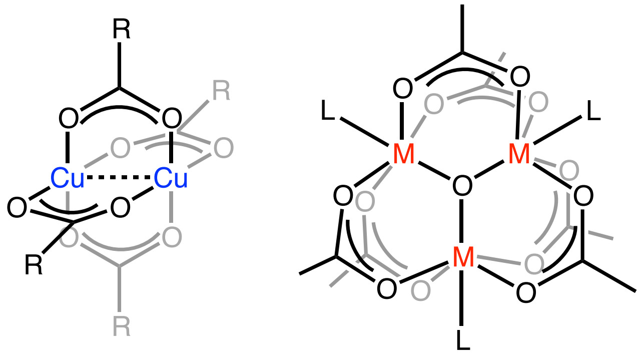

Figure 1.5. Acetate complexes. (left) Dicopper paddlewheel.[52] (right) Oxo-centered trinuclear complex.[53]

synthetic weak-field clusters is that metal atoms are usually separated by more than the van der Waals radii. Accordingly, the metal-metal interactions are based on superexchange through the ligands, rather than direct orbital overlap.

Synthetic weak field clusters include the FeS cubanes and related stuctures, which provide models of the ubiquitous and multifunctional biological cofactors.[1] Model compounds can help clarify the structure and properties of protein cofactors, and provide insight into the effect of the protein structure on the clusters. Synthetic FeS clusters display rich reaction chemistry, including a range of available oxidation states, facile ligand exchange, and a variety of cluster interconversion processes.[49] They are usually magnetically active, sometimes with non-intuitive types of interaction between centers. For instance, in Fe_3S_4 clusters, there is one localized ferric ion, and the other two Fe centers form a mixed-valent pair, with spin-dependent delocalization giving rise to a $^{9}/_{2}$ spin state.[51] Though the Fe atoms in FeS cubanes are separated by roughly the covalent radii,[26] they are typically described in terms of antiferromagnetic coupling between Fe centers that are not mixed-valent pairs, rather than Fe-Fe bonding.

The acetate paddlewheel complexes are the classic weak-field dinuclear complexes. Dicopper acetate paddlewheels provide a textbook example of magnetic exchange coupling.[52]

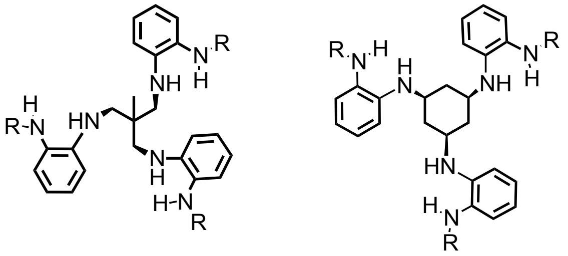

Figure 1.6. Betley group ligand architectures.

One of the most widely used dinuclear catalysts is dirhodium acetate, used industrially for carbene and nitrene transer.[53] Trinuclear oxo-centered acetate complexes provided an early example of more complex magnetic exchange between three metal centers.[54] More recently, larger MnO clusters were discovered to function as single-molecule magnets,[55] inspiring investigations into transition metal clusters as possible future data storage units.[32]

1.5 Ligand-Organized Cluster Synthesis

Previous work in metal cluster chemistry has been limited substantially by synthetic techniques, which have most often relied on self-assembly. Many clusters based on simple ligands form spontaneously, and such clusters have yielded a great deal of insight, and are relevant to many biological systems. However, weak-field clusters based on self-assembly are quite labile and can be very difficult to work with.

Our hypothesis was that we could gain significant insight into the fundamental properties and reactivity of metal clusters by using a multidentate ligand that could pre-organize multiple metals into a desired configuration. This would allow the isolation of homogenous molecules for detailed study and characterization, which is often difficult in native enzyme systems, and also allow for rational tuning of steric and electronic properties via ligand modification.

Scheme 1.1

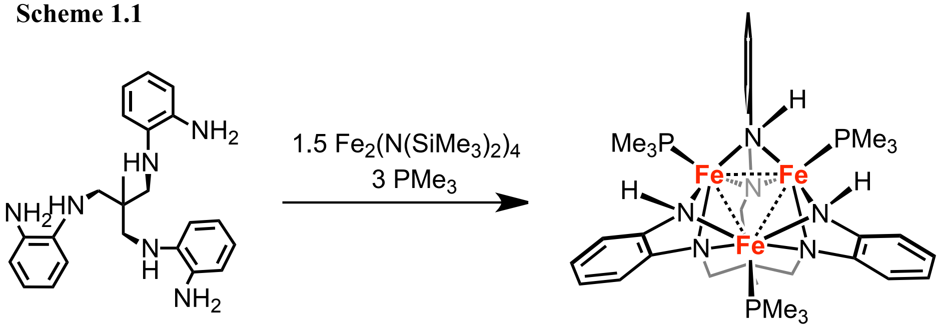

Work in the Betley group has focused on trinuclear complexes based on the hexadentate amine-based ligands $MeC(CH_2NHPh\text{-}o\text{-}NHR)_3$ and 1,3,5-$C_6H_9(NPh\text{-}o\text{-}NHR)_3$. Metallation with three equivalents of Fe(II) with internal base yields well-defined trinuclear clusters. Using the ligand $MeC(CH_2NHPh\text{-}o\text{-}NH_2)_3$, a C_3 symmetric complex results with each Fe pair bridged by two amide ligands.[56] The average Fe–Fe distance is 2.299 Å, which is very short, suggesting metal-metal bonding. The complex is $S = 1$, and Mössbauer spectroscopy shows that the Fe atoms are equivalent. When the complex is oxidized by one electron, crystallography shows little structural change beyond a contraction in the Fe–Fe bonds, to an average of 2.274 Å. The Fe sites remain equivalent by Mössbauer spectroscopy, and the spin increases to $S = 3/2$. The electronic configuration in the neutral complex is proposed to be $[(1a_1)_\sigma{}^2(2a_1)_\sigma{}^2(1e)_\pi{}^4(3a_1)_{nb}{}^2(2e)_{nb}{}^4(1a_2)_{\sigma*}{}^2(3e)_{\pi*}{}^2]$, with a bond order of two over the three metals. Upon oxidation, an electron is removed from an antibonding MO to give $[(1a_1)_\sigma{}^2(2a_1)_\sigma{}^2(1e)_\pi{}^4(3a_1)_{nb}{}^2(2e)_{nb}{}^4(1a_2)_{\sigma*}{}^1(3e)_{\pi*}{}^2]$, with a bond order of 2.5 consistent with the core contraction. This ligand is also capable of other binding modes, particularly in dimerized forms.[37,57]

Very different structures and reactivities are observed using the bulky ligand 1,3,5-$C_6H_9(NPh\text{-}o\text{-}NHSi^tBuMe_2)_3$. Upon metallation with three equivalents of ferrous iron, an asymmetrical structure is observed, in which a single solvent molecule is bound to one Fe and only four of the

Scheme 1.2

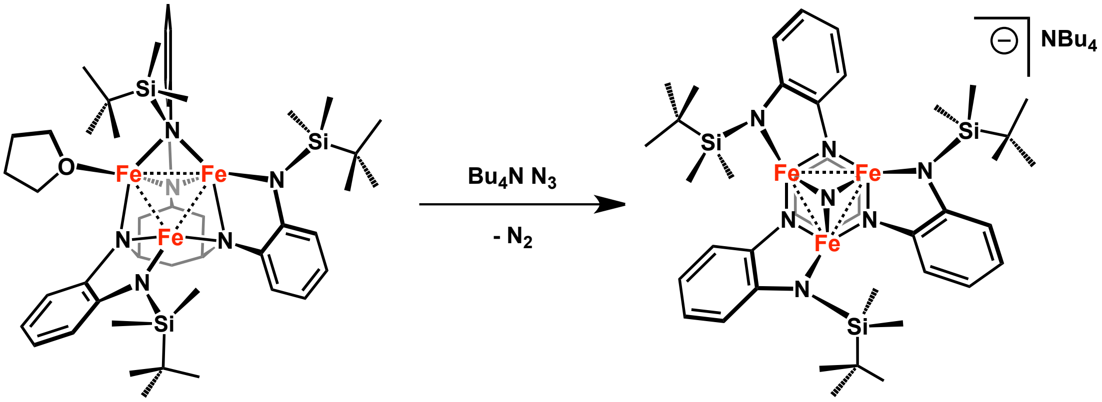

amides bridge two Fe atoms.[58] The Mössbauer spectrum reflects the asymmetry, corroborating the inequivalence of the three Fe sites. The solution magnetic moment suggests a spin of $S = 6$, consistent with the larger Fe–Fe separation of 2.577 Å. Upon addition of inorganic azide, the azide is consumed as determined by IR spectroscopy and X-ray diffraction reveals that the product is the nearly C_3 symmetric μ_3-nitride, with loss of bound solvent and only three amides bridging Fe atoms. The Fe–Fe distances contract to 2.480 Å, and the Mössbauer spectrum shows two equal doublets, with identical isomer shifts. The structure and Mössbauer data show that this is cooperative activation of substrate, with the Fe atoms sharing the oxidation and interaction with the nitride equally.

1.6 Chapter Summaries

In Chapter 2, the synthesis of the ligand MeC(CH$_2$NHPh-*o*-NHPh)$_3$, abbreviated hereafter ^{Ph}LH$_6$, and three of its Fe complexes, ((^{Ph}L)Fe$_3$L$^*_3$, L* = thf, pyridine, PMe$_2$Ph) are described. The three structures are nearly identical, with all six amides bridging and the pendant phenyl groups oriented upwards, blocking the Fe$_3$ face. SQUID data reveal that while (^{Ph}L)Fe$_3$(thf)$_3$ has the shortest Fe–Fe separations, it also has the highest spin, consistent with a maximally high-spin $S = 6$. The stronger field ligands pyridine and PMe_2Ph yield complexes that undergo a spin transition from $S = 2$ to $S = 4$, with the transition temperature higher in the stronger-field phosphine. VT Mössbauer and crystallography confirm that this is a molecular spin state change, rather than an individual ion SCO.

In Chapter 3, one-electron oxidation of $(^{Ph}L)Fe_3(thf)_3$ with iodine and trityl halides is described. The resulting complexes $(^{Ph}L)Fe_3X(L^*)$ (X = Cl, Br, I; L^* = thf, pyridine) and $[(^{Ph}L)Fe_3X]_2$ (X = Cl, Br), show a desymmetrization of the core to an isosceles structure, with two amide ligands no longer bridging and the X/L ligands bound to the unique Fe. The remaining two Fe atoms have a very short contact at 2.30 Å. Mössbauer spectroscopy shows that the oxidation is shared by the two strongly-bound Fe atoms, while the halide is coordinated to the other. SQUID magnetometry suggests that the unique high-spin ferrous ion is coupled ferromagnetically to an $S = {}^3/_2$ mixed valent pair.

In Chapter 4, metal ion lability in the oxidized complexes $[(^{Ph}L)Fe_3Cl]_2$ is described. When stirred in THF with 2 or 5 equiv $CoCl_2$, the Co substitutes in within 2 h, yielding the analytically pure compounds $(^{Ph}L)Fe_2CoCl(ACN)$ and $(^{Ph}L)FeCo_2Cl(ACN)$ in yields of better than 40% after two crystallizations. The structures are analogous to the all-Fe structure, except that the M-M distances are substantially contracted. A combination of analytical techniques including NMR, Mössbauer and XRF spectroscopies, SQUID magnetometry suggest that the Co is exclusively in the strongly-bound M_2 unit, rather than the unique site. However, degenerate exchange experiments with ^{57}Fe observed by Mössbauer spectroscopy suggest that the unique site is most labile.

References Cited

1. Beinert, H.; Holm, R.; Münck, E. *Science* **1997**, *277*, 653.
2. Spatzal, T.; Aksoyoglu, M.; Zhang, L.; Andrade, S. L. A.; Schleicher, E.; Weber, S.; Rees, D. C.; Einsle, O. *Science* **2011**, *334*, 940.
3. Seefeldt, L. C.; Hoffman, B. M.; Dean, D. R. *Annu. Rev. Biochem.* **2009**, *78*, 701.
4. Lancaster, K. M.; Roemelt, M.; Ettenhuber, P.; Hu, Y.; Ribbe, M. W.; Neese, F.; Bergmann, U.; DeBeer, S. *Science* **2011**, *334*, 974.
5. Jeoung, J. H.; Dobbek, H. *Science* **2007**, *318*, 1461.
6. Jeoung, J.-H.; Dobbek, H. *J. Am. Chem. Soc.* **2009**, *131*, 9922.
7. Kung, Y.; Drennan, C. L. *Curr. Opin. Chem. Bio.* **2011**, *15*, 276.
8. Lieberman, R. L.; Rosenzweig, A. C. *Nature* **2005**, *434*, 177.
9. Balasubramanian, R.; Smith, S. M.; Rawat, S.; Yatsunyk, L. A.; Stemmler, T. L.; Rosenzweig, A. C. *Nature* **2010**, *465*, 115.
10. Brown, K.; Tegoni, M.; Prudêncio, M.; Pereira, A. S.; Besson, S.; Moura, J. J.; Moura, I.; Cambillau, C. *Nat. Struct. Biol.* **2000**, *7*, 191.
11. Paraskevopoulos, K.; Antonyuk, S. V.; Sawers, R. G.; Eady, R. R.; Hasnain, S. S. *J. Mol. Biol.* **2006**, *362*, 55.
12. Sproviero, E. M.; Gascón, J. A.; McEvoy, J. P.; Brudvig, G. W.; Batista, V. S. *J. Am. Chem. Soc.* **2008**, *130*, 6728.
13. Ferreira, K. N.; Iverson, T. M.; Maghlaoui, K.; Barber, J.; Iwata, S. *Science* **2004**, *303*, 1831.
14. Johnson, D.; Dean, D.; Smith, A. *Annu. Rev. Biochem.* **2005**, *74*, 247.
15. Wang, J.; Pantopoulos, K. *Biochem. J.* **2011**, *434*, 365.
16. Li, Y.; Zamble, D. B. *Chem. Rev.* **2009**, *109*, 4617.
17. Kim, B.-E.; Nevitt, T.; Thiele, D. J. *Nat. Chem. Biol.* **2008**, *4*, 176.
18. Huniar, U.; Ahlrichs, R.; Coucouvanis, D. *J. Am. Chem. Soc.* **2004**, *126*, 2588.
19. Siegbahn, P. E. M. *Inorg. Chem.* **2000**, *39*, 2923.
20. Einsle, O.; Tezcan, F. A.; Andrade, S. L. A.; Schmid, B.; Yoshida, M.; Howard, J. B.; Rees, D. C. *Science* **2002**, *297*, 1696.
21. Chatt, J.; Dilworth, J.; Richards, R. *Chem. Rev.* **1978**, *78*, 589.
22. Yandulov, D. V.; Schrock, R. R. *Science* **2003**, *301*, 76.

23. Ogata, H.; Kellers, P.; Lubitz, W. *J. Mol. Biol.* **2010**, *402*, 428.

24. Fontecilla-Camps, J. C.; Volbeda, A.; Cavazza, C.; Nicolet, Y. *Chem. Rev.* **2007**, *107*, 4273.

25. Bondi, A. *J. Phys. Chem.* **1964**, *68*, 441.

26. Cordero, B.; Gómez, V.; Platero-Prats, A. E.; Revés, M.; Echeverría, J.; Cremades, E.; Barragán, F.; Alvarez, S. *Dalton Trans.* **2008**, 2832.

27. Kahn, O. *Molecular Magnetism*; VCH Publishers: New York, 1993.

28. Freedman, D. E.; Harman, W. H.; Harris, T. D.; Long, G. J.; Chang, C. J.; Long, J. R. *J. Am. Chem. Soc.* **2010**, *132*, 1224.

29. Koenig, E.; Madeja, K.; Watson, K. J. *J. Am. Chem. Soc.* **1968**, *90*, 1146.

30. Koenig, E.; Watson, K. J. *Chem. Phys. Lett.* **1970**, *6*, 457.

31. Kahn, O. *Chem. Phys. Lett.* **1997**, *265*, 109.

32. Long, J. R. "Molecular Cluster Magnets". In *The chemistry of nanostructured materials*; World Scientific, 2003.

33. Zener, C. *Phys. Rev.* **1951**, *82*, 403.

34. Anderson, P. W.; Hasegawa, H. *Phys. Rev.* **1955**, *100*, 675.

35. Noodleman, L.; Peng, C. Y.; Case, D. A.; Mouesca, J. M. *Coord. Chem. Rev.* **1995**, *144*, 199.

36. Hess, C. R.; Weyhermüller, T.; Bill, E.; Wieghardt, K. *Angew. Chem. Int. Ed.* **2009**, *48*, 3703.

37. Zhao, Q.; Harris, T. D.; Betley, T. A. *J. Am. Chem. Soc.* **2011**, *133*, 8293.

38. Evans, D. F. *J. Chem. Soc.* **1959**, 2003.

39. Shores, M. P.; Sokol, J. J.; Long, J. R. *J. Am. Chem. Soc.* **2002**, *124*, 2279–2292.

40. Borrás Almenar, J.; Clemente Juan, J.; Coronado, E.; Tsukerblat, B. *J. Comput. Chem.* **2001**, *22*, 985.

41. Morse, M. D. *Chem. Rev.* **1986**, *86*, 1049.

42. Ozin, G. A.; Mitchell, S. A. *Angew. Chem. Int. Ed. Engl.* **1983**, *22*, 674.

43. Dyson, P. J. *Coord. Chem. Rev.* **2004**, *248*, 2443.

44. Chisholm, M. *Angew. Chem. Int. Ed. Engl.* **1986**, *25*, 21.

45. Cotton, F. A.; Murillo, C. A.; Walton, R. A. *Multiple bonds between metal atoms*; Springer Science and Business Media, Inc., 2005.

46. Nguyen, T.; Sutton, A. D.; Brynda, M.; Fettinger, J. C.; Long, G. J.; Power, P. P. *Science* **2005**, *310*, 844.

47. Khand, I.; Knox, G.; Pauson, P.; Watts, W. *Perkins Trans. 1* **1973**, 977.
48. Sugihara, T.; Wakabayashi, A.; Nagai, Y.; Takao, H.; Imagawa, H.; Nishizawa, M. *Chem. Commun.* **2002**, 576.
49. Venkateswara Rao, P.; Holm, R. H. *Chem. Rev.* **2004**, *104*, 527.
50. Lee, S. C.; Holm, R. H. *Chem. Rev.* **2004**, *104*, 1135.
51. Papaefthymiou, V.; Girerd, J.; Moura, I.; Moura, J.; Münck, E. *J. Am. Chem. Soc.* **1987**, *109*, 4703.
52. Hay, P.; Thibeault, J.; Hoffman, R. *J. Am. Chem. Soc.* **1975**, *97*, 4884.
53. Davies, H. M. L.; Manning, J. R. *Nature* **2008**, *451*, 417.
54. Kambe, K. *J. Phys. Soc. Jpn.* **1950**, *5*, 48.
55. Sessoli, R.; Gatteschi, D.; Caneschi, A.; Novak, M. *Nature* **1993**, *365*, 141.
56. Zhao, Q.; Betley, T. A. *Angew. Chem. Int. Ed.* **2011**, *50*, 709.
57. Fout, A. R.; Zhao, Q.; Xiao, D. J.; Betley, T. A. *J. Am. Chem. Soc.* **2011**, *133*, 16750.
58. Powers, T. M.; Fout, A. R.; Zheng, S.-L.; Betley, T. A. *J. Am. Chem. Soc.* **2011**, *133*, 3336.

Chapter 2: Modulation of Magnetic Behavior via Ligand-Field Effects in Trigonal Clusters[1]

2.1 Introduction

Strong electronic and/or magnetic interactions between metal centers in polynuclear architectures can find significant utility in the design of various classes of magnetic materials, such as low-density permanent magnets,[2] single-molecule[3] and single-chain magnets,[4] and molecular wires.[5] The magnitude of these interactions is largely dictated by factors such as metal-metal separation and the type, if any, of bridging ligand. For instance, structurally symmetric bridging ligands, in conjunction with mixed-valence metal frameworks, can give rise to spin-dependent electron delocalization via a double exchange mechanism[6] and, consequently, well-isolated, high-spin ground states.[7] Additionally, superexchange between metal centers through diamagnetic bridging ligands, or direct exchange between a metal center and paramagnetic ligand, leads to ferromagnetic or antiferromagnetic coupling of electrons.

Alternatively, direct metal-metal interactions can arise when open-shell metal centers are not sterically prevented from engaging in direct M–M orbital overlap. The resulting interactions can range from single bond (e.g. $Rh_2(OAc)_4$)[8] to multiple bond configurations (e.g. Re_2Cl_8,[9] $(Ar^*)_2Cr_2$).[10] The vast majority of coordination complexes that feature metal-metal bonding are composed of 4*d* and 5*d* transition metal ions or 3*d* ions in strong ligand fields (e.g., CO) and in low oxidation states, giving rise to nearly exclusively low-spin ground states.[11,12] The resulting low-spin configurations preclude observation of the desired properties associated with the presence of unpaired electrons. Substituting weak field for strong field ligand sets with first-row transition ions typically leads to weak exchange interactions between metal ions, rather than metal-metal bonding, owing to their more contracted 3*d*-orbitals that preclude sufficient M–M orbital overlap. Nevertheless, the possibility does exist to enforce direct M–M orbital overlap, creating weak bonding interactions without maximal pairing of the metal valence electrons.

Within polynuclear clusters, it is often difficult to dictate predictably the coordination environments or electronic structure of the individual metal ions or the molecule as a whole.[13] One potential method for achieving these design criteria is employment of a polydentate ligand structure within which the polynuclear core can assemble.[14] Toward this end, we recently reported the synthesis of a new hexadentate ligand $MeC(CH_2NHC_6H_4$-*o*-$NH_2)_3$ ($^{H}LH_6$)[15] that permits the isolation and characterization of well-defined trinuclear[14,16] and hexanuclear iron clusters.[17] The open-shell triiron complexes exhibit Fe–Fe bonding that is strengthened upon oxidation of the [Fe_3] core.[14] In addition, the seven-member electron-transfer series of Fe_6 clusters exhibits redox-dependent physical and chemical properties, which have been rationalized in terms of a qualitative molecular orbital model based on direct, yet relatively weak, Fe–Fe interactions.[16a] We were thus intrigued by the possibility of using structural perturbations to the hexamine ligand platform to tune the degree of metal–metal interactions and thus the electronic structure within the trinuclear core. Herein, we report the synthesis and characterization of a series of triiron complexes wherein the observed Fe–Fe separation is elongated relative to its Fe_3 predecessors, thereby giving rise to complexes featuring both intermediate- and high-spin electronic configurations. Furthermore, the electronic structure of the trinuclear complexes shows a strong dependence on the σ-donor strength of peripheral ligands employed, manifesting itself as changes in the observed spin ground states and temperature-induced changes in spin state. In light of the direct metal-orbital overlap found in this family of complexes, we propose the electronic and magnetic phenomena can be explained by considering the electronic population of a single molecular orbital manifold. The magnetic and spectroscopic data are reflective of this delocalized molecular electronic structure, dictated by simple ligand-field considerations, not individual metal centers within a cluster.

2.2 Results and Discussion

2.2.1 Syntheses and Structures. Standard Pd cross-coupling methodologies were used to install phenyl substituents onto the peripheral ligand amine groups of MeC(CH$_2$NHPh-o-NH$_2$)$_3$ (^{H}LH$_6$) using bromobenzene (3.1 equiv.) and sodium tert-butoxide base (4 equiv.), catalyzed by Pd$_2$(dba)$_3$/rac-BINAP (2.2%, 6.6%, respectively) in toluene (70 °C) for 18 h to afford MeC (CH$_2$NHPh-o-NHPh)$_3$ (^{Ph}LH$_6$, 80% isolated yield). The ligand could be efficiently isolated as a

Scheme 2.1

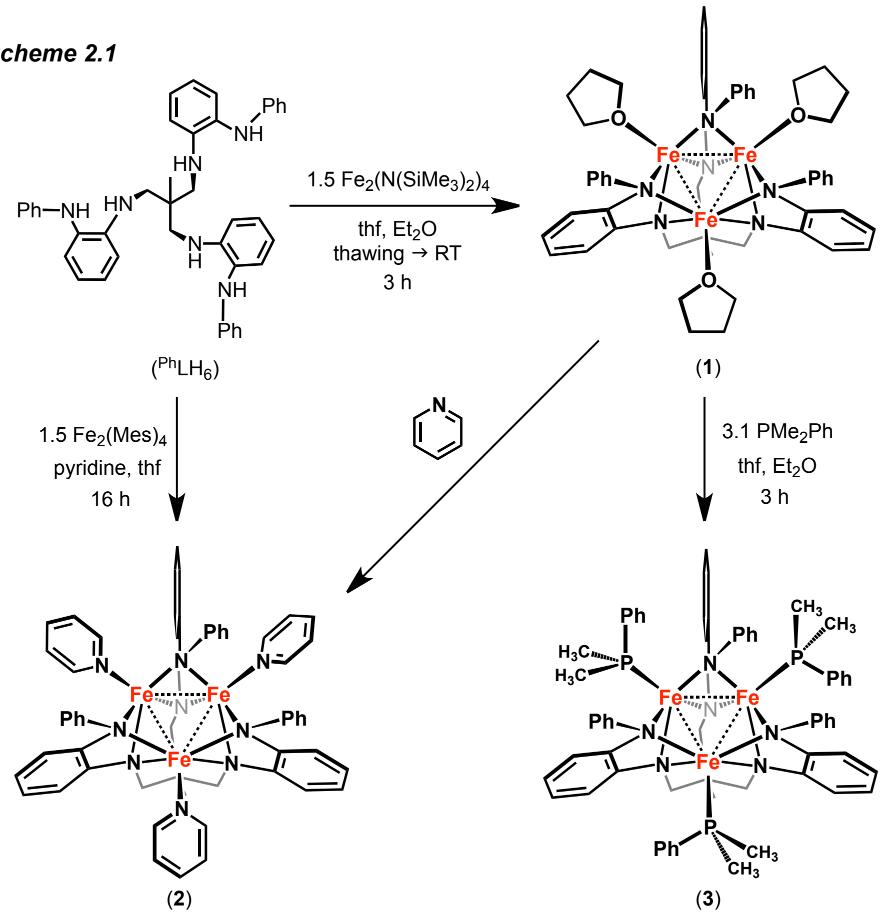

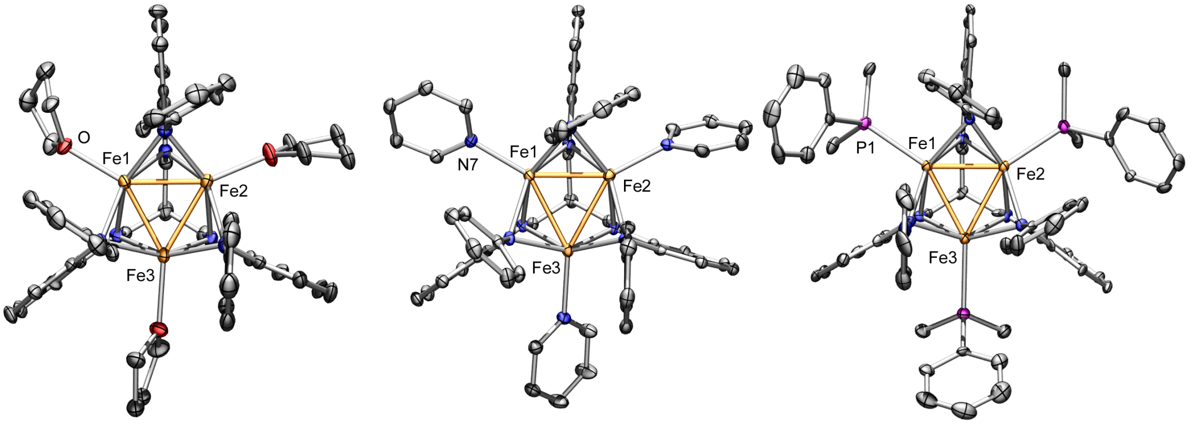

Figure 2.1. Solid-state structures for **1** (a), **2** (b), and **3** (c), with thermal ellipsoids set at the 50% probability level. Orange, magenta, red, blue and gray ellipsoids represent Fe, P, O, N, and C, respectively; hydrogen atoms are omitted for clarity. Selected mean interatomic distances (Å) and angles (°) for **1**: Fe–Fe 2.491(1), Fe–Nbase 2.158(5), Fe–NPh 2.176(5), Fe–O 2.135(4), average Fe-N-Fe 70.14(15); **2**: Fe–Fe 2.576(1), Fe–Nbase 2.139(2), Fe–NPh 2.183(2), Fe–Npy 2.108(2), average Fe-N-Fe 73.15(6); **3**: Fe–Fe 2.585(2), Fe–Nbase 2.138(6), Fe–NPh 2.190(6), Fe–P 2.446(2), average Fe-N-Fe 73.44(16).

pale yellow solid following extraction of the crude reaction mixture with dichloromethane and washing the resultant solids with copious amounts of diethyl ether.

Metallation of the ligand platform was effected using iron-based organometallic or metal-amide starting materials. Reaction of $^{Ph}LH_6$ with 1.5 equivalents of $Fe_2(N(SiMe_3)_2)_4$ in a mixture of thawing diethyl ether and tetrahydrofuran (thf) afforded the stable, brown triiron complex $(^{Ph}L)Fe_3(thf)_3$ (**1**) in good overall yield (λ_{max}/nm (ε /($M^{-1}\cdot cm^{-1}$)): 428 (5800), 590 (2000 sh), 760 (1700); 60%, Scheme 2.1). Structural data are provided in Table 2.1. Complex **1** precipitated as an analytically pure, crystalline solid upon storage at -30 °C over a period of 12 h. A similar reaction of $^{Ph}LH_6$ with $Fe_2(Mes)_4$ in thawing thf with pyridine (3 equivalents) afforded the stable, brown pyridine-ligated complex $(^{Ph}L)Fe_3(py)_3$ (**2**) in good overall yield (λ_{max}/nm (ε /($M^{-1}\cdot cm^{-1}$)) 490 (6100); 66%). Complex **2** could be purified by precipitation from tetrahydrofuran or diethyl ether at -30 °C with excess pyridine present. The labile thf ligands in **1** can be readily exchanged

Table 2.1. Selected Core Bond Distances (Å) and Angles (°) for **1**, **2** and **3**.

Compound (L)	**1** (thf)	**2** (py)	**3** (PMe$_2$Ph)
Fe(1)–Fe(2)	2.4377(11)	2.6074(6)	2.5517(13)
Fe(1)–Fe(3)	2.5114(11)	2.5466(6)	2.5986(13)
Fe(2)–Fe(3)	2.5235(11)	2.5756(6)	2.6057(13)
Fe(1)–L(1)	2.151(4)	2.091(2)	2.479(2)
Fe(2)–L(2)	2.154(4)	2.115(2)	2.461(2)
Fe(3)–L(3)	2.101(4)	2.119(2)	2.397(2)
Fe(1)–N(2)	2.114(4)	2.193(2)	2.098(5)
Fe(1)–N(3)	2.169(5)	2.137(2)	2.099(5)
Fe(1)–N(5)	2.169(5)	2.109(2)	2.161(5)
Fe(1)–N(6)	2.204(4)	2.228(2)	2.265(5)
Fe(2)–N(1)	2.153(4)	2.208(2)	2.104(5)
Fe(2)–N(3)	2.142(4)	2.126(2)	2.204(5)
Fe(2)–N(4)	2.181(4)	2.128(2)	2.196(5)
Fe(2)–N(6)	2.146(4)	2.146(2)	2.108(5)
Fe(3)–N(1)	2.169(5)	2.078(2)	2.163(5)
Fe(3)–N(2)	2.203(5)	2.093(2)	2.158(5)
Fe(3)–N(4)	2.182(4)	2.269(2)	2.196(5)
Fe(3)–N(5)	2.176(5)	2.221(2)	2.212(5)
Fe2-N1-Fe3	71.44(14)	73.81(6)	75.24(16)
Fe1-N2-Fe3	71.11(14)	72.87(6)	75.24(15)
Fe1-N3-Fe2	68.86(13)	75.42(6)	72.69(15)
Fe2-N4-Fe3	70.68(13)	71.64(6)	73.27(15)
Fe1-N5-Fe3	70.61(15)	71.99(6)	72.91(15)
Fe1-N6-Fe2	68.14(13)	73.17(6)	71.29(15)

for stronger σ-donating ligands. For example, reaction of **1** with five equivalents of dimethylphenylphosphine (PMe$_2$Ph) in a mixture of thf and diethyl ether results in formation of the tris-phosphine complex (^{Ph}L)Fe$_3$(PMe$_2$Ph)$_3$ (**3**) (λ_{max}/nm (ε /(M^{-1}·cm^{-1})): 490 (6600), 730 (2300 sh); 65%).

Complex **1** was crystallized from a concentrated solution of benzene and hexanes at -30 °C, while concentrated benzene solutions of **2** and **3** stored at room temperature produced crystals suitable for X-ray diffraction analysis. The solid-state structures for the series are shown in Figure 2.1. In all complexes **1-3**, each iron center resides in a distorted square pyramidal geometry, where four amide nitrogen atoms form a basal plane with an apical ligand (thf, py, or PMe_2Ph) trans to a di-iron unit. Each of the ligand η^2-amide residues bridge adjacent metal ions. The Fe–N bond distances to the base of the hexamide ligand (N_{base}) and diphenylamide crown (N_{Ph}) are consistent across the series (Fe– N_{base} (Å): **1** 2.158(5), **2** 2.139(3), **3** 2.138(6); Fe–N_{Ph} (Å): **1** 2.176(5), **2** 2.183(3), **3** 2.190(6); selected bond distances are provided in Table 1) and substantially elongated in comparison to the $(^{H}L)Fe_3(PMe_2R)_3$ complexes (Fe–N_{base} 1.984(8); Fe–N_H 2.024(8) Å)[14] and related hexanuclear series $[(^{H}L)_2Fe_6(NCCH_3)_m]^{n+}$ (Fe–N_{ave} = 1.961 (2)−2.067(3) Å).[16a] The bond metrics within each of the *o*-phenylenediamide (OPDA) branches are characteristic of being aromatic, closed-shell dianions (see Tables 2.2-2.4) as opposed to other potential ligand oxidation states (i.e., benzosemiquinonate diimine π-radical anion or neutral benzoquinone diimine).[18]

While the gross structural features and ligand connectivity of complexes **1**-**3** are similar to $(^{H}L)Fe_3(PMe_2R)_3$,[14] complexes **1**-**3** feature greater Fe–Fe separation (Å) than oberved in $(^{H}L)Fe_3(PMe_2R)_3$ (average Fe–Fe distance: 2.299(2)Å). Complex **1** features the shortest average Fe–Fe separation of 2.491(1) Å, followed by the pyridine complex **2** with 2.576(1) Å, and the phosphine complex **3** with 2.585(2) Å. The aryl substituents on the modified ligand (^{Ph}L) sterically prevent the Fe ions in **1**-**3** from getting as close as in $(^{H}L)Fe_3(PMe_2R)_3$, but the M–M separation is still within the range of reported Fe–Fe bonding interactions.[19]

Table 2.2. Selected Ligand Bond Distances (Å) for **1** at 193 K.

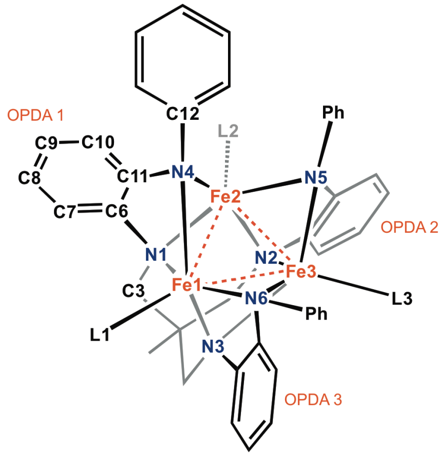

OPDA subunit	**1**	**2**	**3**
C(3)–N(1)	1.456(7)	1.465(7)	1.455(7)
N(1)–C(6)	1.398(7)	1.406(7)	1.401(7)
C(6)–C(7)	1.387(8)	1.388(8)	1.387(8)
C(7)–C(8)	1.396(8)	1.402(7)	1.394(8)
C(8)–C(9)	1.350(8)	1.361(9)	1.371(8)
C(9)–C(10)	1.404(8)	1.384(9)	1.388(8)
C(10)–C(11)	1.381(8)	1.388(8)	1.392(7)
C(6)–C(11)	1.407(7)	1.404(8)	1.422(7)
C(11)–N(4)	1.434(7)	1.417(7)	1.415(7)
N(4)–C(12)	1.425(7)	1.425(7)	1.429(7)

Table 2.3. Selected Ligand Bond Distances (Å) for **2** at 100 K.

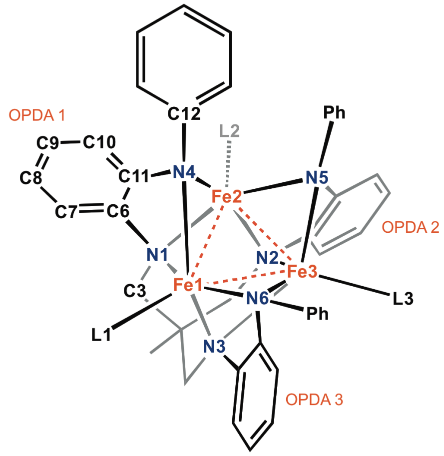

OPDA subunit	**1**	**2**	**3**
C(3)–N(1)	1.452(3)	1.450(3)	1.449(3)
N(1)–C(6)	1.392(3)	1.394(3)	1.394(3)
C(6)–C(7)	1.385(3)	1.384(3)	1.387(3)
C(7)–C(8)	1.396(3)	1.388(3)	1.395(3)
C(8)–C(9)	1.359(3)	1.373(3)	1.369(3)
C(9)–C(10)	1.383(3)	1.389(3)	1.388(3)
C(10)–C(11)	1.389(3)	1.386(3)	1.391(3)
C(6)–C(11)	1.407(3)	1.408(3)	1.404(3)
C(11)–N(4)	1.410(3)	1.409(3)	1.403(3)
N(4)–C(12)	1.420(3)	1.422(3)	1.419(3)

Table 2.4. Selected Ligand Bond Distances (Å) for **3** at 100 K.

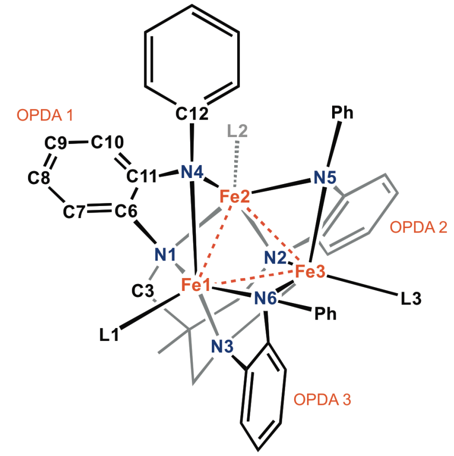

OPDA subunit	**1**	**2**	**3**
C(3)–N(1)	1.455(7)	1.469(7)	1.454(7)
N(1)–C(6)	1.387(7)	1.392(7)	1.394(7)
C(6)–C(7)	1.372(8)	1.369(8)	1.386(8)
C(7)–C(8)	1.382(8)	1.385(8)	1.381(8)
C(8)–C(9)	1.368 (8)	1.373(8)	1.365(8)
C(9)–C(10)	1.377(8)	1.380(8)	1.397(8)
C(10)–C(11)	1.364(8)	1.383(8)	1.380(8)
C(6)–C(11)	1.418(8)	1.420(8)	1.401(8)
C(11)–N(4)	1.414(7)	1.403(7)	1.401(7)
N(4)–C(12)	1.434(7)	1.393(7)	1.416(7)

2.2.2 Mössbauer Spectroscopy. The zero-field ^{57}Fe Mössbauer spectrum of **1** shows a broad asymmetric quadrupole doublet at 105 K ((δ, $|\Delta E_Q|$ ($^{mm}/_{s}$)): 0.79, *1.25*, $\Gamma_L = 0.52$ $^{mm}/_{s}$, $\Gamma_R = 0.43$ $^{mm}/_{s}$, $\Gamma_{\text{Fe foil}} = 0.31$ $^{mm}/_{s}$; see Figure 2.2). Analogous measurements on complexes **2** and **3**

reveal the presence of two quadrupole doublets at 105 K and 110 K, respectively (see Figure 2.2, data summarized in Table 2.5). The major component (70%) in the spectrum for complex **2** features an isomer shift and quadrupole splitting ((δ, $|\Delta E_Q|$ ($^{mm}/_{s}$)): 0.82, *1.48*; 71%) similar to **1**, while the minor component features a larger quadrupole splitting (δ, $|\Delta E_Q|$ ($^{mm}/_{s}$)): 0.85, *2.22*; 29%). The spectrum of complex **3** at 110 K is similar (major component 68%: δ, $|\Delta E_Q|$ ($^{mm}/_{s}$)): 0.77, *1.43*; minor component 32%: δ, $|\Delta E_Q|$ ($^{mm}/_{s}$)): 0.79, *2.30*). The spectral parameters are provided in Table 2.5. The Mössbauer parameters are consistent with a high-spin Fe^{II} electronic

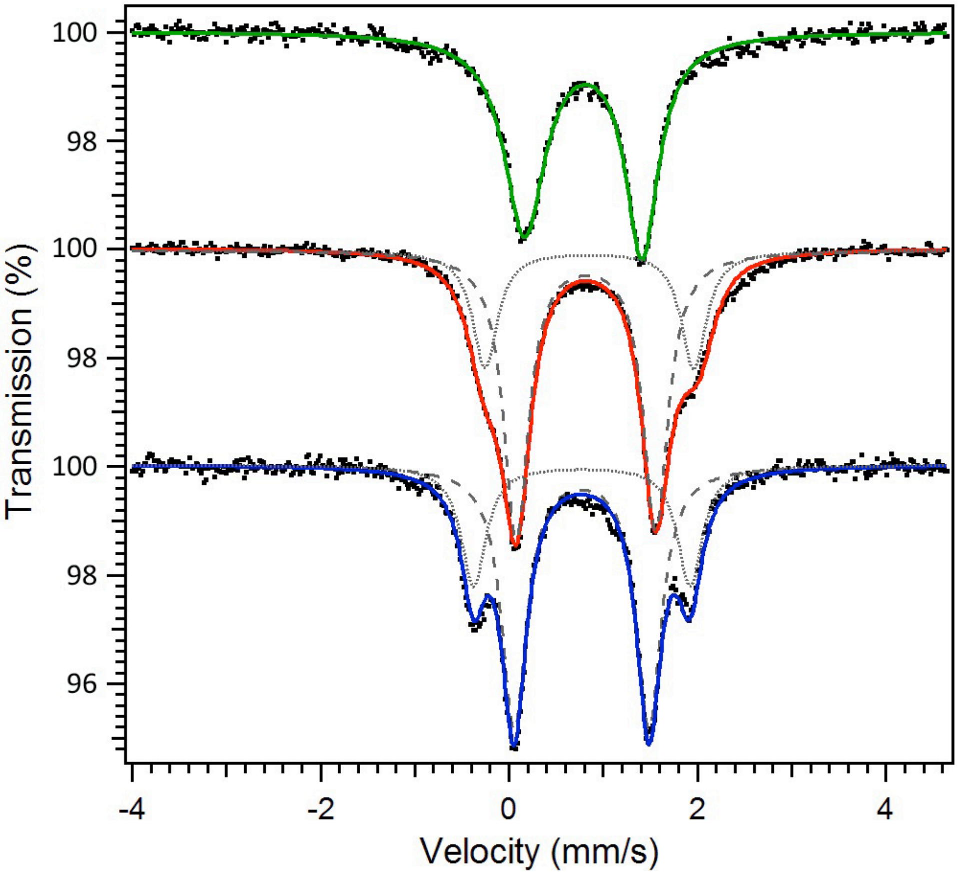

Figure 2.2. Zero-field ^{57}Fe Mössbauer spectra obtained for **1** (105 K; data black dots, spectral fit: green; δ, $|\Delta E_Q|$ ($^{mm}/_{s}$) 0.79, *1.25*); **2** (105 K; data black dots, spectral fit: red; δ, $|\Delta E_Q|$ ($^{mm}/_{s}$) 0.82, *1.48* (71%), 0.85, *2.22* (29%)), and **3** (110 K; data black dots, spectral fit: blue; δ, $|\Delta E_Q|$ ($^{mm}/_{s}$) 0.77, *1.43* (68%), 0.77, *2.30* (32%)).

configuration, however the isomer shifts exceed other five-coordinate iron complexes featuring similar coordination spheres (four *N* and one *P*-donor) with lower spin-states.[17e,20] The isomer shifts for **1-3** are much higher than the low-spin $(^{H}L)Fe_3(PMe_2R)_3$ analogues (see Table 2.5), wherein extensive M–M bonding may substantially reduce shielding of the *s*-electron density at the iron nuclei, which may contribute to the decreased isomer shift.[21]

The presence of two quadrupole doublets for complexes **2** and **3** was probed further by obtaining the Mössbauer spectra at several temperatures. Spectra were collected for a sample of **2** in the temperature range 4-180 K (see Figure 2.3) and for **3** in the range 80-250 K (see Figure 2.4). From 4-105 K, the spectrum for complex **2** exhibits two quadrupole doublets featuring nearly identical isomer shifts, but distinct splitting parameters (e.g., **2** at 4 K: component 1 (δ, |ΔE_Q| ($^{mm}/_{s}$)): 0.83, *1.57*, 64%; component 2: 0.87, *2.76*, 36%; see Table 2.6 for compiled data over all temperature ranges). At 150 K and above, the two quadrupole doublets become less

Table 2.5. Spectral and magnetic properties of complexes **1 - 3**.

compound	*S*	$\chi_M T$ (cm^3·K/mol)	λ / nm (ε / M^{-1}·cm^{-1})	δ ($^{mm}/_{s}$)	$\lvert\Delta E_Q\rvert$ ($^{mm}/_{s}$)	Γ ($^{mm}/_{s}$)^e	(%)
$(^{Ph}L)Fe_3(thf)_3$ (**1**)	6	18.38^a	428 (5800), 590 (2000, sh), 760, (1700)	0.79^f	1.25^f	0.52, 0.43	100
$(^{Ph}L)Fe_3(py)_3$ (**2**)	2	3.04^a (3.08)^b	490 (6100)	0.82^f 0.85	1.48^f 2.22	0.32, 0.32 0.32, 0.32	71 29
	4	9.76^c (12.0)^d					
$(^{Ph}L)Fe_3(PMe_2Ph)_3$ (**3**)	2	3.58^a (3.58)^b	490 (6600), 730 (2300)	0.77^g 0.77	1.43^g 2.30	0.32, 0.32 0.32, 0.32	68 32
	4	7.45^c (14.4)^d					
$(^{H}L)Fe_3(PMe_2Ph)_3$[14]	1	1.01^a	707 (900)	0.38	1.04	0.28, 0.28	100

distinct (e.g., **2** at 180 K: component 1 (δ, $|\Delta E_Q|$ ($^{mm}/_{s}$)): 0.78, *1.36*, 90%; component 2: 0.82, *1.66*, 10%). For complex **3**, the same phenomenom is observed: at and below 150 K two quadrupole doublets with nearly the same isomer shift are apparent (e.g., **3** at 80 K: component 1 (δ, $|\Delta E_Q|$ ($^{mm}/_{s}$)): 0.78, *1.43*, 67%; component 2: 0.78, *2.43*, 33%), and for temperatures at and above 200 K, the hyperfine parameters for the two quadrupole doublets nearly converge (e.g., **3** at 200 K: component 1 (δ, $|\Delta E_Q|$ ($^{mm}/_{s}$)): 0.73, *1.42*, 72%; component 2: 0.74, *1.81*, 28%). The data at each temperature have been thus modeled using two quadrupole doublets (see Table 2.6).

The isomer shifts for complex **1** and the contributing components in complexes **2** and **3** all fall within a very narrow range (δ: 0.7–0.87 $^{mm}/_{s}$). The presence of the two distinct quadrupole splitting parameters might correlate to molecular distortions present in the complexes or to a change in molecular spin-states (see below). Support for a correlation to a structural distortion arises from the isosceles distortion featured by **1-3**. At the low-temperature extreme for **2**, the quadrupole doublets are in a nearly 2:1 ratio, consistent with the geometrically distinct site manifesting a different electronic field gradient. Indeed, a similar observation was made regarding the Mössbauer spectra obtained for the related triiron compounds $(NBu_4)[(^{tbs}L)Fe_3(\mu^3\text{-}N)]$ and $(^{tbs}L)Fe_3(\mu^3\text{-}NCH_3)$.[15] Both of these compounds feature two quadrupole doublets with identical isomer shifts and differing quadrupole splitting parameters that coalesce to a single quadrupole doublet at elevated temperatures. In all of these cases, as the temperature increases, the iron nuclei within the complexes feel the same electronic charge distribution, giving rise to similar (or identical) isomer shift and quadrupole splitting parameters. Alternatively, the spectral changes observed in the Mössbauer may correlate to changes in the molecular spin state. This hypothesis is tested in the following section.

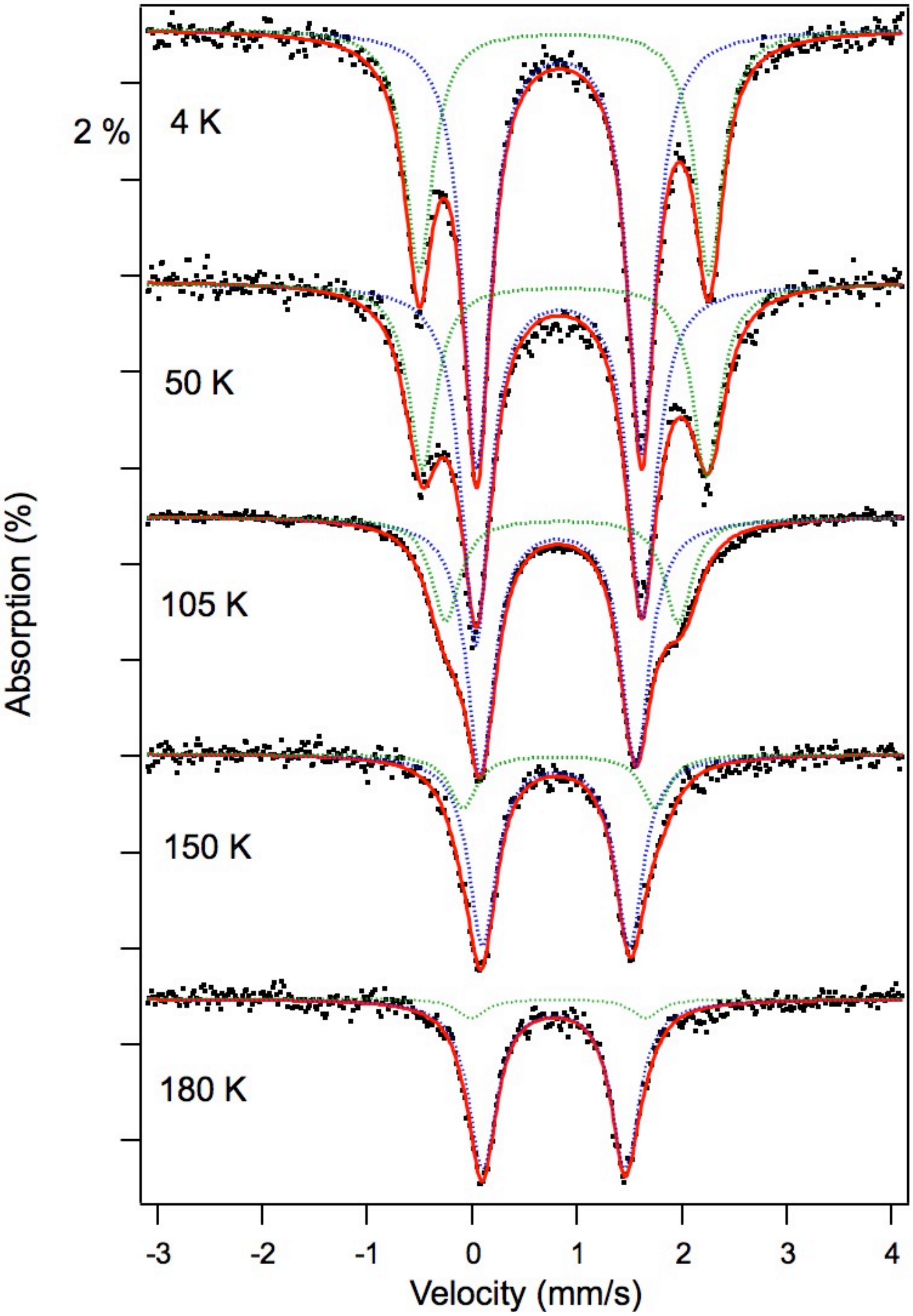

Figure 2.3. Variable-temperature zero-field ^{57}Fe Mössbauer spectra obtained for **2** represented by black dots, spectral fit as solid red line (sum of minor components at variable temperatures) (δ, |ΔE_Q| ($^{mm}/_{s}$)): 4 K 0.83, *1.57* (64%), 0.87, *2.76* (36%); 50 K 0.83, *1.59* (65%), 0.88, *2.71* (35%); 105 K 0.82, *1.48* (71%), 0.86, *2.22* (29%); 150 K 0.80, *1.40* (78%), 0.83, *1.83* (22%); 180 K 0.78, *1.36* (90%), 0.82, *1.66* (10%).

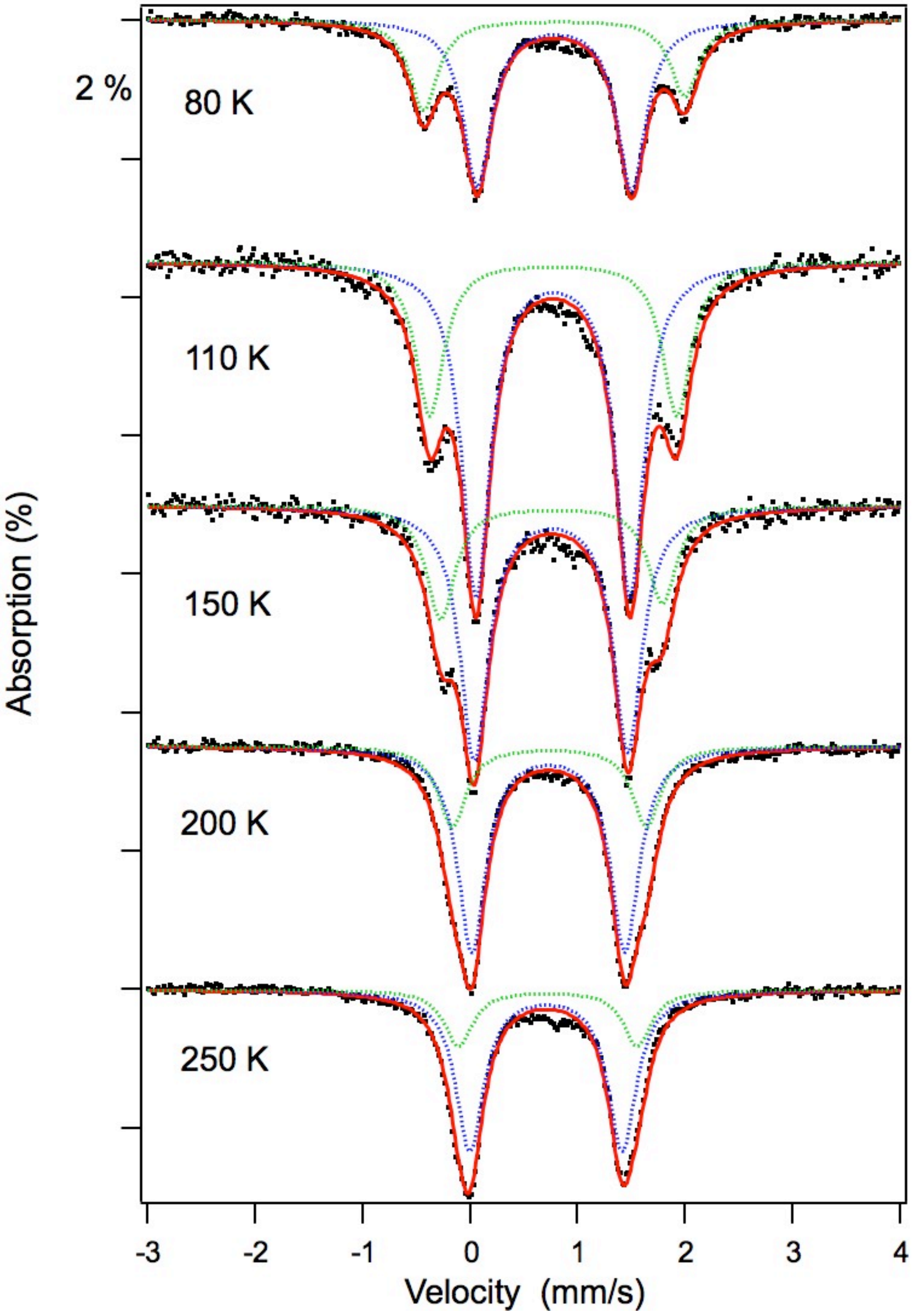

Figure 2.4. Variable-temperature zero-field ^{57}Fe Mössbauer spectra obtained for **3** represented by black dots, spectral fit as solid red line (sum of minor components at variable temperatures) (δ, |*ΔE*$_Q$| ($^{\mathrm{mm}}/_{\mathrm{s}}$)): 80 K 0.78, *1.43* (67%), 0.78, *2.43* (33%); 110 K 0.77, *1.43* (68%), 0.77, *2.30* (32%); 150 K 0.75, *1.43* (70%), 0.76, *2.06* (30%); 200 K 0.73, *1.42* (72%), 0.74, *1.81* (28%); 250 K 0.70, *1.42* (74%), 0.72, *1.66* (26%).

Table 2.6. ^{57}Fe Mössbauer fitting parameters. Errors in δ, ΔE_Q and FWHM (2γ) are <0.01 mm/s unless otherwise specified.

Compound	T (K)	Fit type	λ (kHz)	δ (mm/s)	ΔE_Q (mm/s)	%	FWHM (mm/s) (left area:right area, if allowed to vary)
1	105	lorentzian		0.79	1.25	100	0.52 (left, 47%) 0.43 (right, 53%)
2	4	relaxation	35 ± 40	0.83	1.57	64	0.32
				0.87	2.76	36	0.32
		lorentzian		0.83	1.57	64	0.32 (51:49)
				0.87	2.76	36	0.32 (50:50)
	50	relaxation	750 ± 60	0.83	1.55	64	0.32
				0.88	2.76	36	0.32
		lorentzian		0.83	1.59	65	0.32 (52:48)
				0.88	2.71	35	0.32 (49:51)
	105	relaxation	1110 ± 50	0.82	1.45	70	0.32
				0.87	2.33	30	0.32
		lorentzian		0.82	1.48	71	0.32 (51:49)
				0.85	2.22	29	0.32 (50:50)
	150	relaxation	1290 ± 350	0.80	1.37	80	0.32
				0.85 ± 0.02	2.00 ± 0.03	20	0.32
		lorentzian		0.80	1.40	78	0.32
				0.83	1.83 ± 0.02	22	0.32
	180	relaxation	0 ± 700	0.78	1.36	90	0.32
				0.82 ± 0.04	1.66 ± 0.05	10	0.32
		lorentzian		0.78	1.36	90	0.32
				0.82 ± 0.02	1.66 ± 0.06	10	0.32
3	80	relaxation	0 ± 40	0.78	1.43	67	0.32
				0.78	2.43	33	0.32
		lorentzian		0.78	1.43	67	0.32 (49:51)
				0.78	2.43	33	0.32 (54:46)
	110	relaxation	0 ± 40	0.77	1.43	68	0.32
				0.77	2.30	32	0.32
		lorentzian		0.77	1.43	68	0.32 (51:49)
				0.77	2.30	32	0.32 (54:46)
	150	relaxation	0 ± 70	0.75	1.43	70	0.32
				0.76	2.06	30	0.32
		lorentzian		0.75	1.43	70	0.32 (51:49)
				0.76	2.06	30	0.32 (54:46)

Table 2.6 (Continued).

200	relaxation	0 ± 90	0.73	1.42	72	0.32
			0.74	1.81	28	0.32
	lorentzian		0.73	1.42	72	0.32
			0.74	1.81	28	0.32
250	relaxation	0 ± 350	0.70	1.42	74	0.32
			0.72 ± 0.01	1.66 ± 0.01	26	0.32
	lorentzian		0.70	1.44	100	0.32 (51:49)

2.2.3 Magnetic Properties. To probe the magnetic behavior of complexes **1-3**, variable-temperature dc susceptibility data were collected in the temperature range of 5-300 K. In the case of **1**, $\chi_M T$ remains relatively constant from 300 K down to 30 K, with an average value of $\chi_M T$ = 18.5 cm^3·K/mol (see Figure 2.5). Below 30 K, the data undergo a downturn, likely the result of Zeeman and zero-field splitting. The value of $\chi_M T$ = 18.5 cm^3·K/mol is much larger than the 9.00 cm^3·K/mol expected for three non-interacting high-spin Fe^{II} ions with g = 2.00, indicative of ferromagnetic coupling that persists even to 300 K. Indeed, the observed value is only slightly lower than the 21.0 cm^3·K/mol expected for an S = 6 ground state with g = 2.00. Accordingly, the data were modeled according to the following spin Hamiltonian given in Eq 2.1.

$$\hat{H} = -2J(\boldsymbol{S}_{\mathrm{Fe1}}\boldsymbol{S}_{\mathrm{Fe2}} + \boldsymbol{S}_{\mathrm{Fe2}}\boldsymbol{S}_{\mathrm{Fe3}} + \boldsymbol{S}_{\mathrm{Fe1}}\boldsymbol{S}_{\mathrm{Fe3}}) + D\boldsymbol{S}^2 + g\mu_{\mathrm{B}}\boldsymbol{S}\cdot\boldsymbol{B} \qquad \text{Equation 2.1}$$

The corresponding simulation using the program MAGPACK[22] that best reproduces the data affords parameters of $J \geq +125$ cm^{-1}, $D = +3.5$ cm^{-1}, and g = 1.88. Alternatively, the average value of $\chi_M T$ (18.5 cm^3·K/mol) for the temperature range 30-300 K may correspond to an S = 5 ground state with g = 2.22. Such a strong ferromagnetic interaction likely results from superexchange between Fe centers through the bridging amide ligands and/or direct exchange between Fe centers, as the average Fe-Fe separation of 2.491(1) Å is within the range of previously reported Fe–Fe bonding interactions.[18] The presence of such a high-spin ground state that remains isolated to 300 K is exceedingly rare in multinuclear clusters. In fact, evidence of the first example of an isolated $S = 6$ ground state was only very recently reported for the related cluster compounds (^{tbs}L)Fe$_3$(thf)[15] and (^{H}L)$_2$Fe$_6$.[16a] Among other single-valence complexes, we are not aware of examples exceeding $S = 4$, which has been observed in an Fe$_4$S$_4$ cubane cluster[23] and a diiron paddlewheel complex.[24] Finally, a number of dinuclear, Class III mixed-valence [Fe$_2$]^{V} complexes have been shown to exhibit well-isolated $S = {}^{9}/_{2}$ ground states that arise from electron delocalization via a double-exchange mechanism.[6a,25]

To further probe the spin ground state and downturn of $\chi_M T$ at low temperature, variable-temperature magnetization data were collected in the temperature range 1.8-10 K at fields of 1 to 7 T. The resulting plot of reduced magnetization, shown in Figure 2.6, features a series of non-

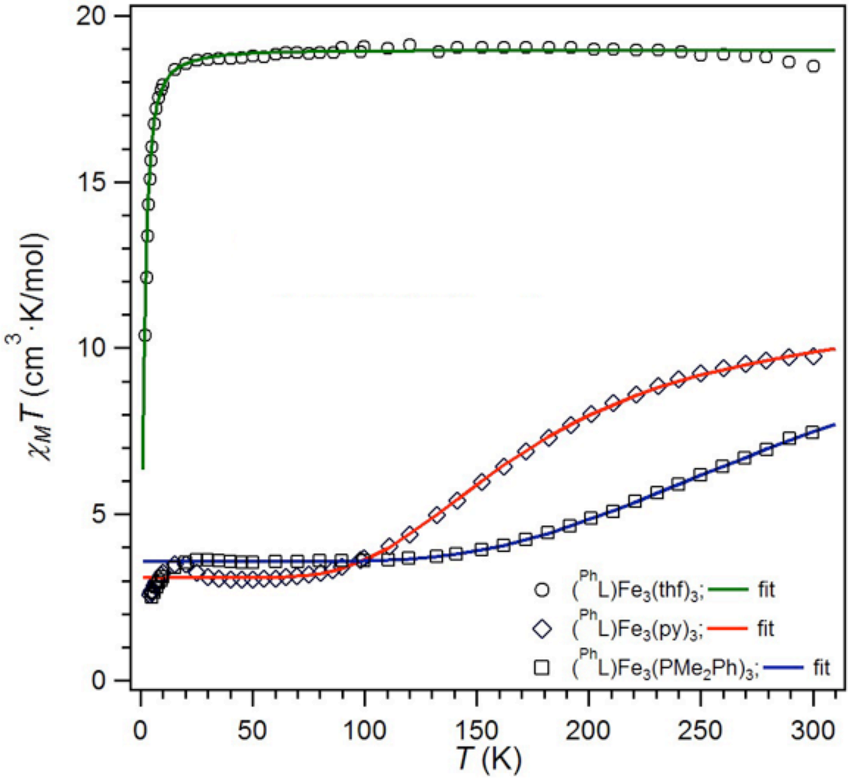

Figure 2.5. Variable-temperature magnetic susceptibility data for **1** (circles), **2** (diamonds), and **3** (squares), collected in an applied dc field of 0.1 T. Solid lines represent fits to the data as described in the text.

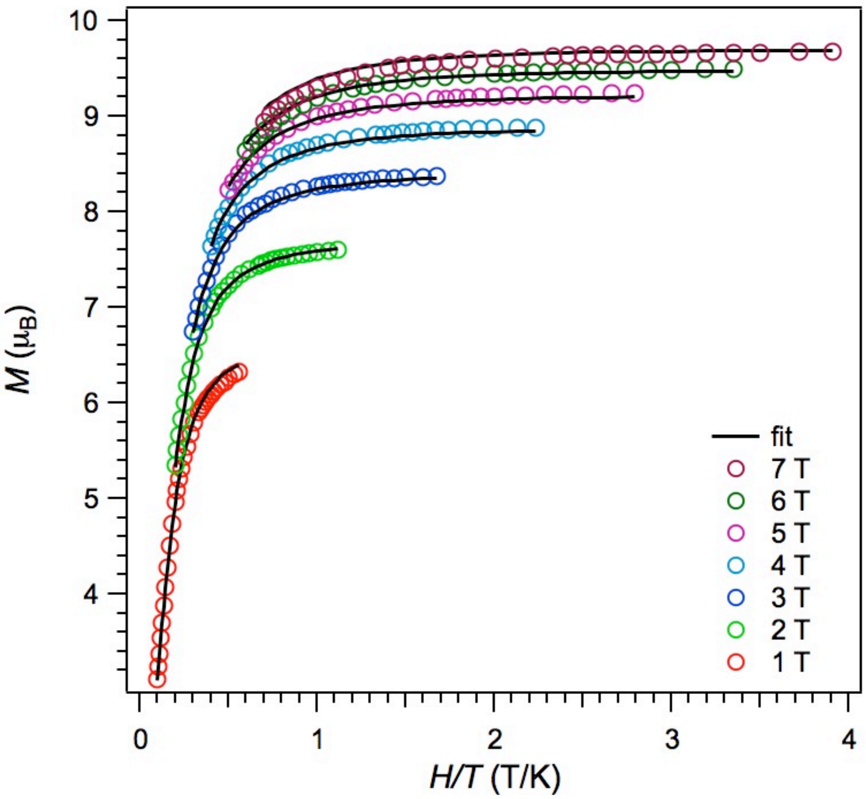

Figure 2.6. Variable-temperature magnetization data for **1** collected at various fields. Solid black lines correspond to fits to the data, as described in the text (D = +1.3 cm^{-1}, |E| = 0.2 cm^{-1}, and g = 1.9), for S = 6.

superimposable isofield curves, with the 7 T curve reaching a maximum value of M = 9.7 m$_B$ at 1.8 K. While this value falls short of the 12.0 m$_B$ expected for an S = 6 ground state, the non-superimposability of the isofield curves demonstrates that significant magnetic anisotropy is precluding saturation of the magnetization. To quantify this effect, the data were modeled according to the Hamiltonian given in Equation 2.2.

$$\hat{H} = D\hat{S}_z^2 + E(\hat{S}_x^2 - \hat{S}_y^2) + g\mu_B \boldsymbol{S}\cdot\boldsymbol{B} \qquad \text{Equation 2.2}$$

The corresponding fit to the data, obtained using ANISOFIT 2.0[26] and considering an S = 6 ground state, provides axial and transverse zero-field splitting parameters of D = +1.3 cm^{-1} and |E| = 0.2 cm^{-1}, respectively, with g = 1.9. Note that a fit of similar quality can be obtained for an S

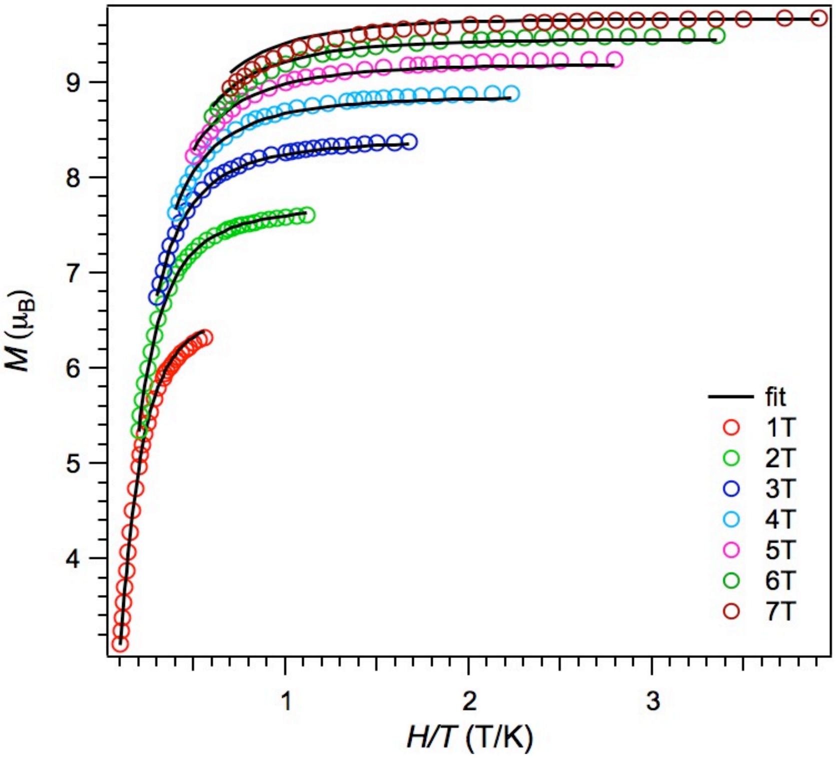

Figure 2.7. Variable-temperature magnetization data for **1** collected at various fields. Solid black lines correspond to fits to the data, as described in the text ($D = +1.7$ cm^{-1}, $|E| = 0.3$ cm^{-1}, and $g = 2.3$), for $S = 5$.

= 5 ground state, giving values of $D = +1.7$ cm^{-1}, $|E| = 0.3$ cm^{-1}, and $g = 2.3$ (see Figure 2.7).

In sharp contrast to the temperature-independent magnetic susceptibility observed for **1**, the $\chi_M T$ vs. T data for **2** undergo a gradual decline from 9.76 cm^3·K/ mol at 300 K to 3.04 cm^3·K/ mol at 40 K (see Figure 2.5). At 300 K, the value of $\chi_M T$ is reasonably close to the expected value of 9.00 for three non-interacting Fe^{II} ions with $g = 2.00$. In addition, the value at 40 K is close to the value of 3.00 expected for an $S = 2$ state. This behavior was initially interpreted as resulting from antiferromagnetic superexchange between Fe^{II} centers through the bridging amide ligands. As such, the data were first modeled according to the spin Hamilonian for an equilateral triangle of Fe^{II} centers given in Equation 1. However, using MAGPACK, this model failed to reproduce the data (see Figure 2.8). As such, the following two alternative models were also

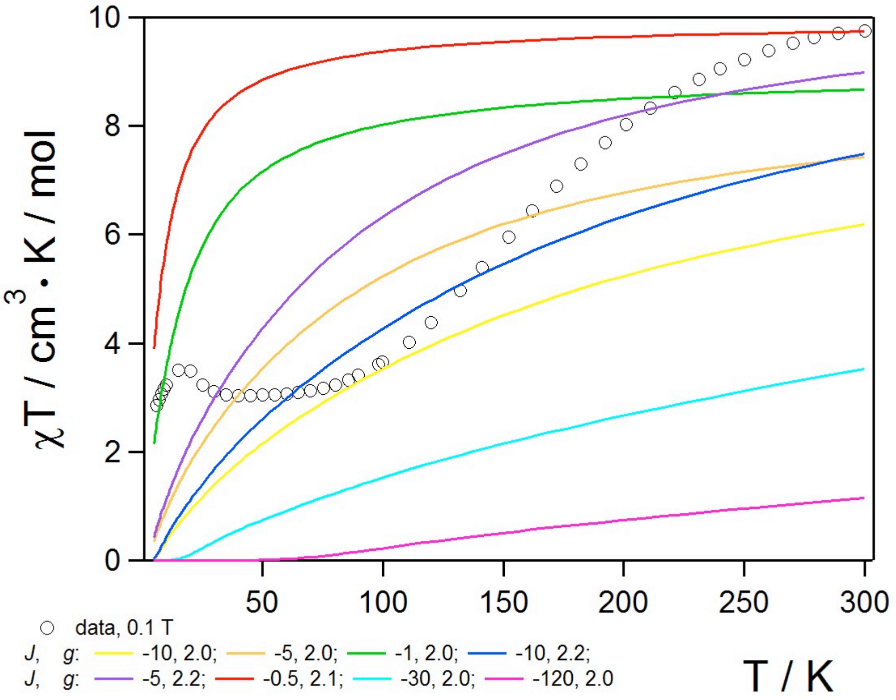

Figure 2.8. Variable-temperature magnetic susceptibility data for **2** collected under a field of 0.1 T. The solid lines correspond to various simulations, as described in the text, with *J* given in cm^{-1}.

employed, considering isosceles (2 independent *J* values) and scalar (3 independent *J* values) triangles, respectively:

$$\hat{H} = -2[J_1(\boldsymbol{S}_{\mathrm{Fe1}}\boldsymbol{S}_{\mathrm{Fe2}} + \boldsymbol{S}_{\mathrm{Fe2}}\boldsymbol{S}_{\mathrm{Fe3}}) + J_2\boldsymbol{S}_{\mathrm{Fe1}}\boldsymbol{S}_{\mathrm{Fe3}}] + D\boldsymbol{S}^2 + g\mu_{\mathrm{B}}\boldsymbol{S}\cdot\boldsymbol{B} \qquad \text{Equation 2.3}$$

$$\hat{H} = -2(J_1\boldsymbol{S}_{\mathrm{Fe1}}\boldsymbol{S}_{\mathrm{Fe2}} + J_2\boldsymbol{S}_{\mathrm{Fe2}}\boldsymbol{S}_{\mathrm{Fe3}} + J_3\boldsymbol{S}_{\mathrm{Fe1}}\boldsymbol{S}_{\mathrm{Fe3}}) + D\boldsymbol{S}^2 + g\mu_{\mathrm{B}}\boldsymbol{S}\cdot\boldsymbol{B} \qquad \text{Equation 2.4}$$

Still, neither of these models, despite the introduction of additional parameters, succeeded to reproduce the data (see Figures 2.9-2.10). Qualitative inspection of the data along with various simulations reveals the incompatibility of the high- and low-temperature regimes when considering a simple superexchange mechanism. Indeed, in order for the exchange interaction to be strong enough to provide ground state isolation at 40 K for **2**, the value of $\chi_{\mathrm{M}}T$ at 300 K must

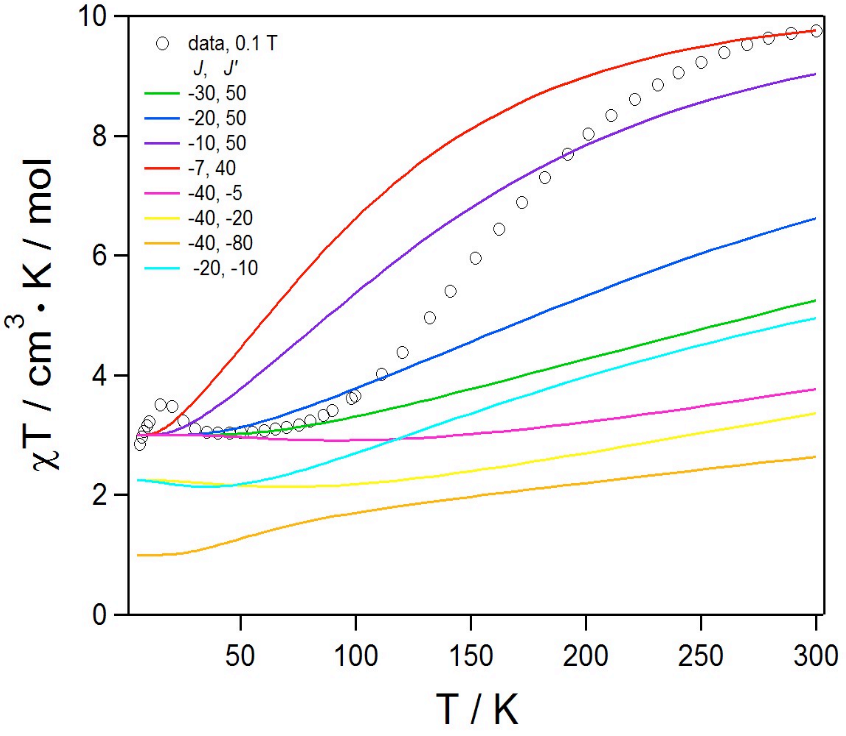

Figure 2.9. Variable-temperature magnetic susceptibility data for **2** collected under a field of 0.1 T. The solid lines correspond to various simulations, as described in the text, with *J* given in

be much lower than that observed. Furthermore, a shift from ferromagnetic superexchange in compound **1** to antiferromagnetic superexchange in compound **2** would likely be dictated by Fe–N–Fe angle. However, the mean Fe–N–Fe angle changes only from 70.14(15)° in **1** to 73.15(6)° in **2** (73.44(15)° in **3** (see Table 2.1). While dramatic magnetostructural correlation is not uncommon in dinuclear Cu^{II}–X–Cu^{II} (X = O, OH, Cl, Br) linkages, where the nature and magnitude of superexchange is dictated by Cu–X–Cu angle and the electronic properties of other ancillary ligands,[27] we are unaware of such pronounced magnetostructural dependence among iron(II) centers. Moreover, an *S* = 6 ground state, isolated at 300 K, has been observed in the related cluster (^{tbs}L)Fe_3(thf),[15] which features an even larger mean Fe–N–Fe angle of 77.95(8)°.[15] Thus, it is unlikely that the exchange in the Fe_3 core would shift from ferromagnetic to

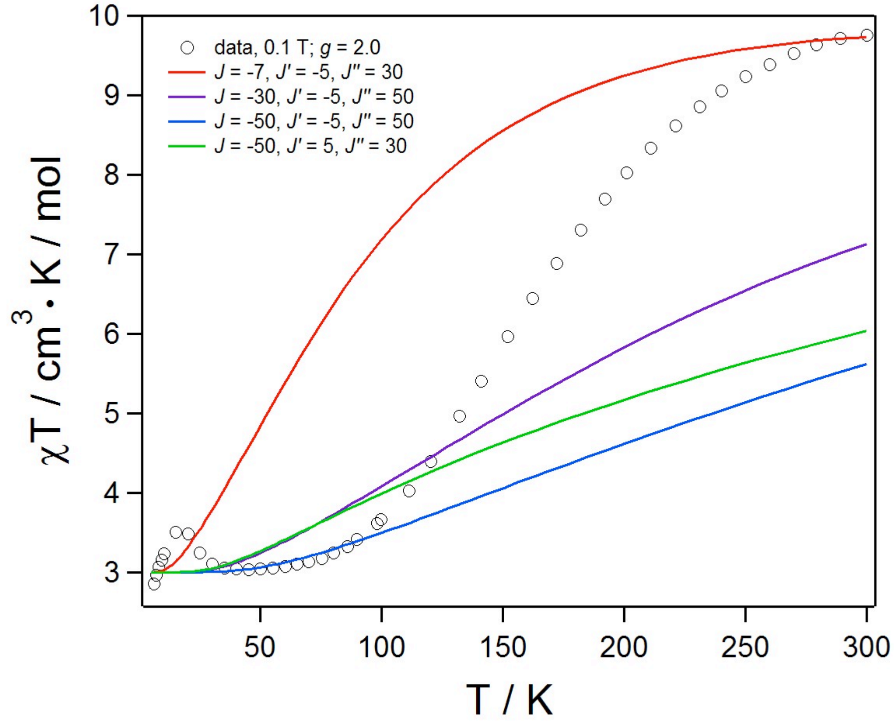

Figure 2.10. Variable-temperature magnetic susceptibility data for **2** collected under a field of 0.1 T. The solid lines correspond to various simulations, as described in the text, with *J* given in cm^{-1}.

antiferromagnetic, then back to ferromagnetic, with increasing Fe–N–Fe angle.

Another possible explanation of the temperature-dependent behavior of **2** is site-isolated spin crossover of the individual Fe^{II} centers.[28] However, spin crossover is typically accompanied by diagnostic spectroscopic and structural changes, where ferrous ions, in particular, exhibit substantial changes in the observed isomer shift and quadrupole splitting in the Mössbauer spectrum.[27a,b,d] While two quadrupole doublets are apparent in the Mössbauer spectra of **2** at temperatures below 105, respectively, the isomer shifts for both contributing components in both complexes are nearly identical in all cases and very similar for all three complexes studied. Moreover, large structural changes typically accompany Fe^{II} centers undergoing a spin crossover as the electronic configuration changes from low-spin to high-spin.[27e,29] Yet, variable-

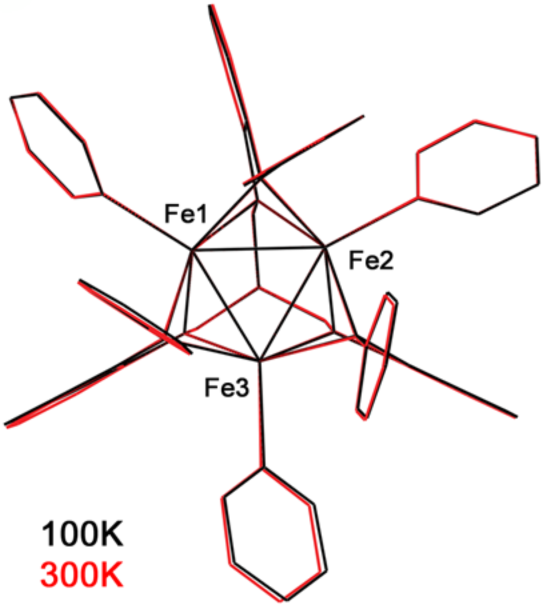

Figure 2.11. Overlay of the X-ray crystal structure for **2** obtained at 100 K (black) and 300 K (red).

temperature X-ray diffraction on a single crystal of **2** does not show evidence for any structural changes in the temperature range of 100-300 K in 50 K increments, further suggesting the individual Fe ions in **2** are not undergoing spin state transitions. The overlay of the molecular structure obtained for **2** at 100 K and 300 K is displayed in Figure 2.11. Notably, the local iron coordination environments, the bond metrics within the triiron core, and the gross structural features for the molecule as a whole are preserved over the temperature range investigated.

Since superexchange through the amide bridges or site-isolated spin crossover do not provide a satisfactory model for the magnetic behavior of **2**, we consider a thermal equilibrium between an $S = 2$ ground state and second, single excited spin state. Indeed, while the value of $\chi_M T = 9.76$ cm^3·K/mol at 300 K is close to the 9.00 expected for three isolated high-spin Fe^{II} ions, it is even closer to the expected value of 10.0 for a single, $S = 4$ spin state. Here, the Fe_3 core can be considered as a single spin unit, arising from a delocalized core electronic structure.

Along these lines, recent spectroscopic and magnetic analysis have provided evidence for a similar phenomenon in the related clusters $[(^{H}L)_2Fe_6(NCMe)_m]^{n+}$ (m = 0, 2, 4, 6; n = -1, 0, 1, 2, 3, 4, 6).[16a,b] To quantitatively probe the possiblity of a delocalized spin equilibrium, the $\chi_M T$ data were modeled from 40-300 K considering a simple Boltzmann population (see Figure 2.5) of the two states, according to the following expressions:

$$x = \frac{1}{1 + \exp[(\Delta H/R)(1/T - 1/T_C)]} \qquad \text{Equation 2.5}$$

$$x = \frac{\chi T - (\chi T)_{LS}}{(\chi T)_{HS} - (\chi T)_{LS}} \qquad \text{Equation 2.6}$$

where x is the molar fraction of high-spin (in this case $S = 4$) molecules, χH is the change in enthalpy associated with the spin state transition, R is the molar gas constant, and T_C is the critical temperature.[30] Indeed, this treatment leads to an excellent fit of the data, providing estimates of thermodynamic parameters of ΔH = 406 cm^{-1} and T_C = 187 K.[31] The population of lower S values in **2**, in contrast to the well-isolated $S = 6$ state in **1**, is likely a direct result of stronger field pyridine versus THF ancillary ligands (see below). The observation of a delocalized spin state equilibrium here is reminiscient of a class of mixed-valence dinuclear $[Ru_2]^{5+}$ species.[32] In these species, variable-temperature magnetic susceptibility data indicated a thermally-induced transition from an $S = {}^1/_2$ state to an $S = {}^3/_2$ ground state. In addition, a similar $S = {}^1/_2 \rightleftharpoons S = {}^3/_2$ equilibrium was recently reported in the dinitrogen-bridged, mixed-valence dichromium complex $[(dmpe)_4Cr^{I}Cr^{II}(C_2Si^{i}Pr_3)_2(\mu\text{-}N_2)]^{+}$.[33] Regarding examples of trinuclear clusters exhibiting such a phenomenon, a family of linear Co_3 complexes was shown to display transitions between both integer[34] and non-integer[35] spin states, depending on oxidation state.

Trigonal trinuclear Co and mixed Co/Rh complexes featuring carbonyl or chalcogenide capped trinuclear cores have been shown to feature thermally induced spin state changes analogous to those reported herein.[36]

In order to confirm the $S = 2$ ground state in **2**, low-temperature magnetization data were collected. The corresponding plot of reduced magnetization displays a set of non-superimposable isofield curves, with a maximum value of $M = 3.1\ \mu_B$ at 7 T and 1.8 K (see Figure 2.12). When treated with the Hamiltonian in Equation 2.2 and ANISOFIT 2.0, the data are modeled well in the temperature range 3-10 K for an $S = 2$ ground state, providing parameters of $D = +14.7\ \text{cm}^{-1}$, $|E| = 4.0\ \text{cm}^{-1}$, and $g = 2.2$. Note that at temperatures below 3 K, especially at low fields, the data

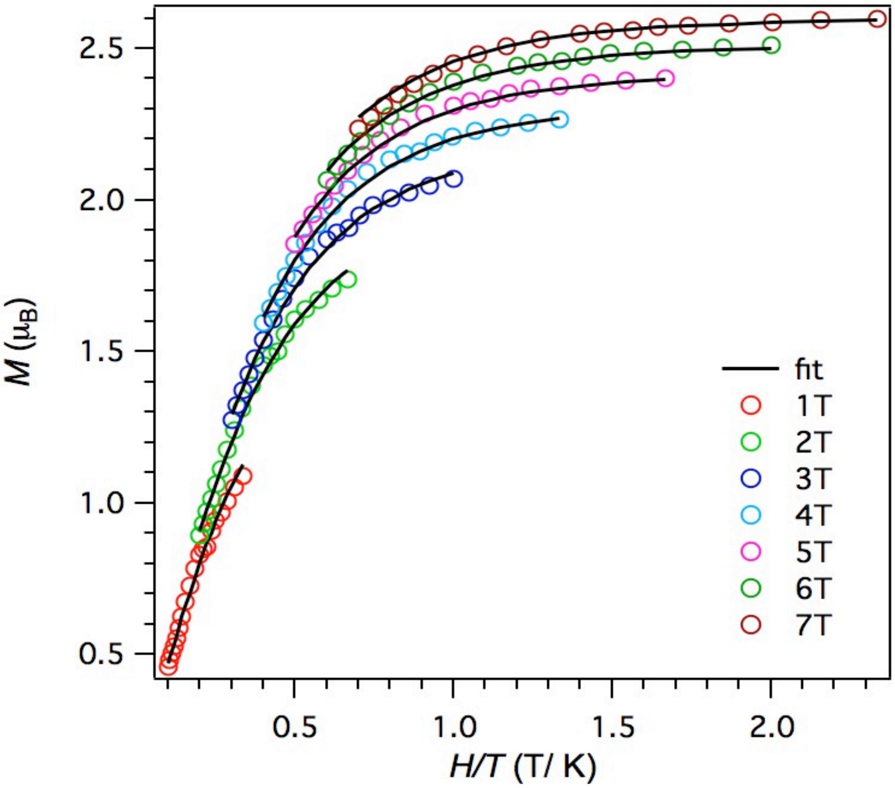

Figure 2.12. Variable-temperature magnetization data for **2** collected at various fields. Solid black lines correspond to fits to the data, as described in the text ($D = +14.7\ \text{cm}^{-1}$, $|E| = 4.0\ \text{cm}^{-1}$, and $g = 2.2$), for $S = 2$.

undergo a slight downturn, possibly stemming from weak intermolecular interactions between neighboring clusters.

The plot of $\chi_M T$ vs. T for compound **3** exhibits a profile similar to that of **2**, albeit with a transition shifted to higher temperature (see Figure 2.5).[37] Indeed, as temperature is decreased, $\chi_M T$ undergoes a gradual decline from 7.45 $cm^3 \cdot K$/ mol at 300 K to a plateau of 3.58 $cm^3 \cdot K$/mol below 100 K. The data for **3** can be treated analogously to those for **2**, according to Equations 2.6 and 2.7, to give parameters of of $\Delta H = 604\ cm^{-1}$ and $T_C = 375$ K.[38] Here, the substantial increase in transition temperature when moving from **2** to **3** is consistent with replacing pyridine ligands with stronger field phosphine ligands (see below).

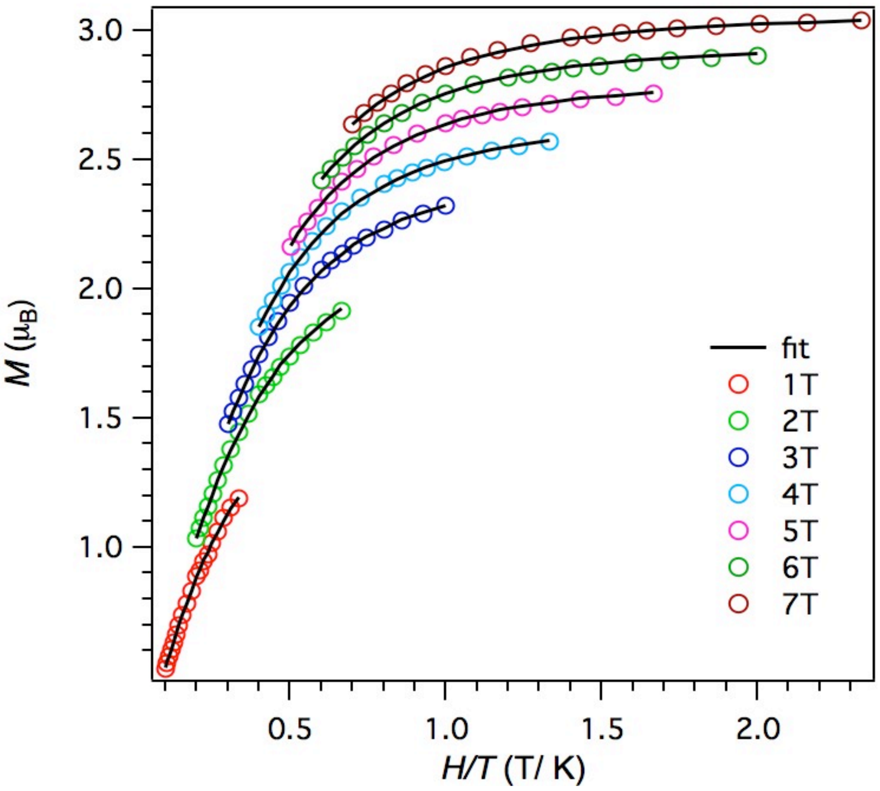

Figure 2.13. Variable-temperature magnetization data for **3** collected at various fields. Solid black lines correspond to fits to the data, as described in the text ($D = +8.5\ cm^{-1}$, $|E| = 2.0\ cm^{-1}$, and $g = 2.2$), for $S = 2$.

Low-temperature magnetization data, collected for compound **3** in the temperature range 3-10 K, are very similar to those for compound **2** (see Figure 2.13). Indeed, a plot of reduced magnetization reveals a set of non-superimposable isofield curves, with the magnetization reaching a maximum of $M = 3.1\ \mu_B$ at 7 T and 1.8 K. Accordingly, the data can be fit considering an $S = 2$ ground state to give parameters of $D = +8.5\ \text{cm}^{-1}$, $|E| = 2.0\ \text{cm}^{-1}$, and $g = 2.2$. Finally, below 3 K, the data undergo a slight downturn, akin to that observed for compound **2**.

Attempts to correlate the change in molecular spin-state with the change in observed Mössbauer parameters for complexes **2** and **3** have thus far been unsuccessful. The convergence of the two quadrupole doublets into a single quadrupole doublet does not manifest at the same temperatures where the spin-state change occurs. For both complexes the quadrupole splitting parameters have significantly converged before a substantial fraction of the $S = 4$ state should be present. For example, the Mossbauer spectrum of **3** at 150 K shows nearly superimposed quardupole doublets (Figure 2.4), whereas the susceptibility data indicate the majority of the material should remain in the ground state (Figure 2.5). Furthermore, attempts to reproduce the data using a relaxation model[39] failed to yield physically reasonable parameters (see Experimental section for details).

2.2.4 Qualitative Electronic Structure. The above analysis, based on magnetic, crystallographic, and Mössbauer spectral data, provides strong evidence that the observed behavior of the Fe_3 clusters cannot be attributed simply to superexchange through bridging amide ligands or site-isolated spin crossover. As such, we turn our attention to the possibility that the phenomena can be explained according to a simple qualitative molecular orbital scheme, where iron-iron interactions within the core give rise to a set of frontier orbitals comprised of 3d

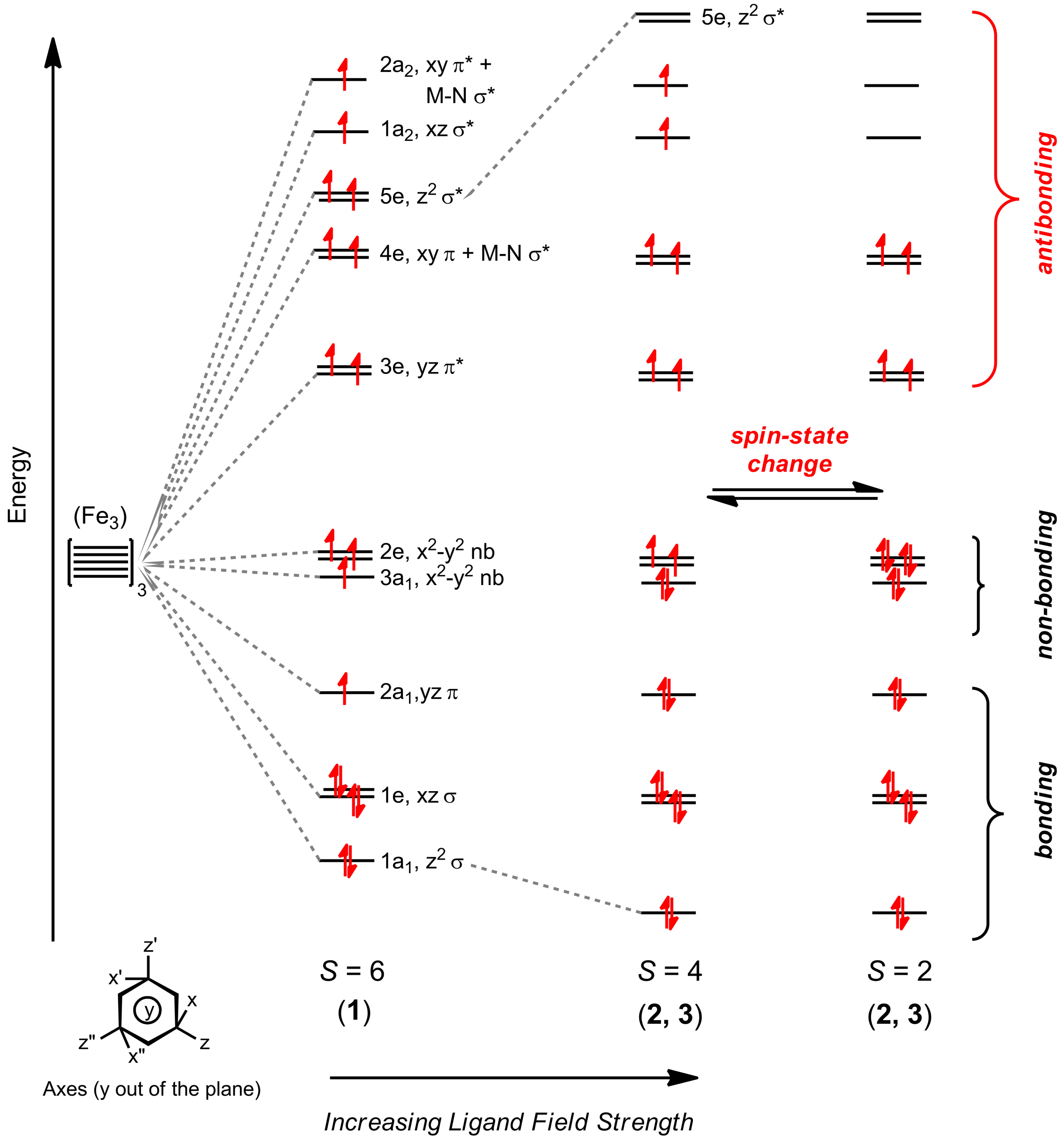

Figure 2.14. Molecular orbital representation of the 3d-orbital manifold for the trinuclear Fe complexes. Increasing the ancillary ligand strength increases the energy of the 5e orbital set, making thermal population of the $S = 6$ spin state inaccessible.

orbitals. This approach is derived following Cotton's method of describing metal-metal bonding interactions in $[Re_3Cl_9(\mu^2\text{-}Cl)_3]^3$,[40] which has also been applied to describe the M–M interactions within $(^{H}L)Fe_3(PMe_2R)_3$.[14] In addition, we recently presented a similar model, closely following previous work with octahedral M_6 clusters,[39,41] to rationalize the redox-dependent properties of an electron-transfer series of octahedral Fe_6 clusters.[16a] Mixing the frontier orbitals of the three iron centers produces six bonding (4e features M–M σ bonding overlap with M–N σ* character), three non-bonding, and six anti-bonding molecular orbital combinations with respect to the M–M interactions, qualitatively illustrated in Figure 2.14. For a trinuclear all-ferrous cluster, populating the 15 frontier *d*-orbitals with 18 valence electrons gives rise to possible spin states from $S = 0$ to $S = 6$. The combination of the weak-field bridging amide ligands and the weak-field thf ligands likely engenders the high-spin, $S = 6$ ground state in **1**. Here, the high-spin electronic configuration for **1** results from populating all available orbitals, even the highest-energy $2a_2$ ($\sigma_{Fe\text{–}N}$*) orbitals. Note, however, that the possibility of an $S = 5$ ground state, as suggested by fits to reduced magnetization data as an alternative configuration, could exist given a substantial energetic separation between the $1a_2$ and $2a_2$ orbitals.

Moving from compound **1** to compound **2**, the three ancillary thf ligands are replaced by pyridine ligands. The stronger ligand field imposed by the pyridine ligands should most significantly modulate the relative energies of Fe_3 core orbitals with d_{z^2} character, as those orbitals can engage in σ interactions with the ancillary ligand p_z orbitals. Specifically, these interactions are expected to lower the energy of the $1a_1$ bonding molecular orbital, while raising the energy of the 5e antibonding orbitals. Indeed, the energetic increase of the 5e orbital set is consistent with the lower spin ground state of **2** compared to **1**, where population of the $S = 6$ spin state is not inaccessible. Based on this rationale, **3** would be expected to exhibit similar behavior, as the even stronger-field phosphine ligands would lead to a further lowering of the $1a_1$ and raising of the 5e orbitals. Notably, though, perturbation of the d_{z^2}-based orbitals alone dose not explain the difference in T_C observed between **2** and **3**. Possibly, π-type interactions would need to be considered to rationalize this discrepancy, however, we limit our orbital treatment to σ-interactions in order to avoid overcomplication of a simple and rudimentary model.

2.3 Conclusions and Outlook

The development of polynuclear coordination complexes in our laboratory was intended to give rise to well-defined molecules with greater redox-flexibility and tunable electronic structure. Tri-iron complexes have now been observed spanning five distinct spin-states: $S = 1, {}^{3}/_{2}, 2, 4,$ and 6.[14,15] Thus it is possible to stabilize polynuclear, open-shell clusters, whose direct M–M interactions give rise to electronic configurations suggestive of delocalized bonding maintained across the spin-state series. The magnetic data and Mössbauer spectra obtained for these complexes are reflective of this delocalized *molecular* electronic state, not *individual* metal centers within a cluster. In principle, similar open-shell electronic configurations could be realized for other polynuclear complexes, encompassing other transition metal ions and with higher nuclearity. Research is currently underway to probe these possibilities and to determine how the electronic structure of polynuclear complexes changes when undergoing redox chemistry.

2.4 Experimental Section

Materials and Methods. All manipulations involving metal complexes were carried out using standard Schlenk line or glove-box techniques under a dinitrogen atmosphere. All glassware was oven-dried for a minimum of 4 h and cooled in an evacuated antechamber prior to use in the dry box. Benzene, toluene, diethyl ether, hexanes and tetrahydrofuran (THF) were dried and deoxygenated on a Glass Contour System (SG Water USA, Nashua, NH) and stored over 4 Å molecular sieves (Strem) prior to use. Dimethylsulfoxide-d_6 and chloroform-d were purchased from Cambridge Isotope Labs and used as received. Benzene-d_6 and THF-d_8 were purchased from Cambridge Isotope Labs and were degassed and stored over 4 Å molecular sieves prior to use. Non-halogenated solvents were typically tested with a standard purple solution of sodium benzophenone ketyl in THF in order to confirm effective oxygen and moisture removal. $MeC(CH_2NHC_6H_4$-*o*-$NH_2)_3$ (^HL)[42], $Fe_2(N(Si(CH_3)_2)_2)_4$[43] and Fe_2Mes_4 (Mes = 2,4,6-$Me_3C_6H_2$)[44] were prepared following published methods. Anhydrous pyridine was purchased from Aldrich and stored over 4 Å molecular sieves prior to use. $Pd_2(dba)_3$ (Strem), bromobenzene (Aldrich), sodium tert-butoxide (Aldrich), BINAP (Strem), PMe_2Ph (Strem) were used as received. All other reagents were purchased from commercial vendors and used without further purification unless explicitly stated.

Physical Measurements. All of the measurements for the metal complexes were made under anaerobic conditions. Elemental analyses were performed by Complete Analysis Laboratories, Inc., Parsippany, New Jersey or Robertson Microlit Laboratories, Madison, New Jersey. ^1H and ^{13}C NMR spectra were recorded on a Varian Unity/Inova 500B or Varian Mercury 400B NMR spectrometer with chemical shifts (δ ppm) referenced to residual NMR solvent. UV/Visible spectra were recorded on a Varian Cary 50 UV/Visible spectrometer using quartz cuvettes. NIR spectra were recorded on a PerkinElmer Lambda 750 high-performance UV-vis spectrometer. The spectrum of **3** was recorded in benzene with excess PMe_2Ph to maintain the stability of the complex and blanked appropriately with the solution used for dilution of the sample. The spectra of **1** and **2** were recorded in THF and benzene respectively for the same reason; if **2** is collected in THF the spectrum resembles that of **1**.

Magnetic measurements were recorded using a Quantum Design MPMS-5S magnetometer. Samples were suspended in the magnetometer in folded plastic bags or suspended in eicosane wax contained in Lilly #4 gel capsules, inserted into plastic straws. All manipulations were performed under an atmosphere of dinitrogen. Dc magnetic susceptibility data were collected in the temperature range 2-300 K under fields of 0.1, 0.5, 1 and 2 T. Magnetization data were acquired at 1.8-10 K under fields of 1, 2, 3, 4, 5, 6, and 7 T. Susceptibility data were corrected for the diamagnetic contribution of a blank sample consisting of the bag or wax, capsule and straw at the correct field and temperature. The magnetic susceptibilities were adjusted for diamagnetic contributions using the constitutive corrections from Pascal's constants. The molar magnetic susceptibility (χ_m) was calculated by converting the magnetization (M) obtained from the magnetometer to a molar susceptibility using the multiplication factor [molecular weight (MW)]/[sample weight (m) × field strength (H)].

Iron-57 Mössbauer spectra were measured on a constant acceleration spectrometer (SEE Co, Minneapolis, MN) with a Janis SVT-100 cryostat. Isomer shifts are quoted relative to α-Fe foil (< 25 μm thick) at room temperature. The Fe foil standard spectrum has linewidths Γ (FWHM) of 0.292 and 0.326 mm/s for the doublets within the ±4 mm/s window when measured outside the cryostat at room temperature. Samples were prepared using approximately 30 mg of sample suspended in paratone-N oil (**1** and **2**) or eicosane wax (**3**). Data for **2** and **3** were collected at multiple temperatures. Temperatures were controlled using a LakeShore 321

Autotuning temperature controller. Temperature swings were no greater than ±10 K, and were generally within ±2 K.

Data were analyzed using an in-house package written by E. R. King and modified by E. V. Eames in Igor Pro (Wavemetrics). Initially a simple model consisting of lorentzian lineshapes with optional asymmetry was used. However, both compounds **2** and **3** show temperature-dependent asymmetry in the doublet peaks, which suggests that a relaxation process between two states with differing hyperfine parameters may be present. Accordingly, the data were fit with a relaxation model following the approach of Litterst and Amthauer.[45] This model supposes that two states of differing hyperfine parameters exist for a given Fe atom, with transition probability per second λ. The fitting expression used was

$$\phi(\omega) \propto \frac{(\Gamma/2+\lambda)A-(\omega-p_1\varepsilon_2-p_2\varepsilon_1)B}{A^2+B^2}+\frac{(\Gamma/2+\lambda)A'-(\omega-p_1\varepsilon'_2-p_2\varepsilon'_1)B'}{A'^2+B'^2} \qquad \text{Equation 2.7}$$

with

$$\begin{aligned}
A &= (\omega-\varepsilon_1)(\omega-\varepsilon_2)-\Gamma/2(\Gamma/2+\lambda)\\
A' &= (\omega-\varepsilon'_1)(\omega-\varepsilon'_2)-\Gamma/2(\Gamma/2+\lambda)\\
B &= (\Gamma+\lambda)\omega-\Gamma/2(\varepsilon_1+\varepsilon_2)-\lambda(p_1\varepsilon_1+p_2\varepsilon_2)\\
B' &= (\Gamma+\lambda)\omega-\Gamma/2(\varepsilon'_1+\varepsilon'_2)-\lambda(p_1\varepsilon'_1+p_2\varepsilon'_2)\\
\varepsilon_1 &= S_1+\Delta_1/2\\
\varepsilon'_1 &= S_1-\Delta_1/2\\
\varepsilon_2 &= S_2+\Delta_2/2\\
\varepsilon'_2 &= S_2-\Delta_2/2
\end{aligned}$$

where Γ is the full width at half maximum (FWHM), and S_n is the chemical shift, Δ_n is the quadrupole splitting, and p_n is the population of state n. For comparison in all fits with both models, the linewidth Γ was held constant at 0.32 mm/s, which is the best fit FWHM observed for both compounds at the lowest temperature. In both cases, the overlap between the doublets resulted in fits of similar quality with a variety of parameter values, precluding a conclusive interpretation. Fits were attempted using both the same sign of electric field gradient for both components and opposite signs, but there was little difference between the two; fits with the same sign are shown. Compound **2** can be fit using the relaxation model to yield a plausible set of parameters, with the relaxation rate λ and the population of the major doublet increasing with temperature, and the isomer shifts and quadrupole splittings decreasing. However, the fits do not model the asymmetry of the peaks very well. Compound **3** cannot be modelled convincingly with this method, as at most temperatures fits yield a relaxation rate of zero, implying that a simple model consisting of four lorentzians is preferred.

Preparation of $\mathbf{MeC(CH_2NHC_6H_4\text{-}\textit{o}\text{-}NHPh)_3}$ ($\mathbf{^{Ph}LH_6}$): $Pd_2(dba)_3$ (103 mg, 112 μmol, 2.2 mol %) and BINAP (211 mg, 337 μmol, 6.6 mol %) were dissolved in 15 mL toluene and heated to 35 ºC for 40 min, then filtered and combined with $MeC(CH_2NHC_6H_4\text{-}\textit{o}\text{-}NH_2)_3$ (2 g, 5.12 mmol, 1 equiv), bromobenzene (2.42 g, 15.4 mmol, 3 equiv), sodium tert-butoxide (1.97 g, 20.5 mmol, 4 equiv) and toluene (200 mL) and heated in a sealed bomb at 70 ºC for 18 h. The product was extracted with dichloromethane, washed twice with water, dried over Na_2SO_4, filtered and the solvent removed under reduced pressure. The resulting pale yellow solid was washed with ether and dried under vacuum to yield 2.54 g, (80%). ^1H NMR ($CDCl_3$, 500 MHz, δ, ppm): 7.12 (t, 6H, aromatic C-*H*, *J* = 7.6 Hz), 7.06-7.04 (m, 6H, aromatic C-*H*), 6.78 (t, 3H, aromatic C-*H*, *J* = 7.5 Hz), 6.69 (d, 3H, aromatic C-*H*, *J* = 7.5 Hz), 6.58 (d, 3H, aromatic C-*H*, *J* = 8.0 Hz), 6.56 (d, 6H, aromatic C-*H*, *J* = 7.0 Hz), 3.04 (s, 6H, -NH-CH_2-C), 0.86 (s, 3H, -C-CH_3); ^{13}C NMR (C_6D_6, 500 MHz, δ, ppm): 146.21, 145.01, 129.36, 126.91, 126.41, 121.48, 119.25, 117.47, 115.06, 111.43, 49.80, 39.17, 20.53; HRMS (ESI$^+$) *m/z* calcd $C_{41}H_{37}N_6^+$ $[M+H]^+$: 619.35437, found 619.35488.

Preparation of (^{Ph}L)Fe$_3$(THF)$_3$ (1). To a frozen solution of ^{Ph}LH$_6$ (1 g, 1.6 mmol, 1 equiv) in THF (15 ml) and diethyl ether (200 mL) was added Fe$_2$(N(Si(CH$_3$)$_2$)$_2$)$_4$ (1.83 g, 4.87 mmol, 3 equiv) as a solution in diethyl ether (20 mL). The solution was allowed to thaw with stirring. After stirring for 3 h, the brown solution was concentrated to 40 mL and stored at –35 °C for 24 h. The resulting brown crystals were washed with THF. Analytical samples were recrystallized under similar conditions. Yield: 0.99 g (60%) after first crystallization; additional product could be isolated by concentrating solution and washes for a second batch of crystals. ^{1}H NMR (C$_6$D$_6$, 500 MHz, δ, ppm): 37, 17, 10, 6, -5, -46, -53, -70. UV-vis (THF) (λ_{max}/nm ((ε/ M^{-1}cm^{-1})) 428 (5800), 590 (2000, sh), 760, (1700). Anal. Calcd for C$_{53}$H$_{60}$Fe$_3$N$_6$O$_3$: C 63.87, H 6.07, N 8.43. Found: C 63.82, H 5.95, N 8.24.

Preparation of (^{Ph}L)Fe$_3$(py)$_3$ (2). To a frozen solution of Fe$_2$Mes$_4$ (2.86 g, 4.8 mmol, 1.5 equiv) in THF (100 mL) was added pyridine (842 mg, 9.6 mmol, 3 equiv). The solution was allowed to thaw with stirring, then frozen and ^{Ph}LH$_6$ (2 g, 3.2 mmol, 1 equiv) in 25 ml cold THF was added. The reaction was stirred for 18 h, then concentrated and filtered with THF or ether. The product was precipitated at –35 °C in the presence of excess pyridine as a brown powder, washed with hexanes, and dried under vacuum overnight. Yield: 2.18 g (66%). X-ray quality crystals were grown from a concentrated solution in benzene with a drop of pyridine at room temperature. ^{1}H NMR (C$_6$D$_6$, 500 MHz, δ, ppm): 88, 32, 25, 14, 12, 9, -31, -36, -39. UV-vis (benzene) (λ_{max}/nm ((ε/M^{-1}cm^{-1}) 490 (6100, sh). IR (KBr pellet) 1592, 1474, 1443, 746, 695 cm^{-1}. Anal. Calcd for C$_{56}$H$_{52}$Fe$_3$N$_9$: C 66.10, H 5.05, N 12.39. Found: C 66.04, H 5.38, N 12.36.

Preparation of (^{Ph}L)Fe$_3$(PMe$_2$Ph)$_3$ (3). (^{Ph}L)Fe$_3$(THF)$_3$ (230 mg, 231 nmol) was dissolved in THF and diethyl ether (1:1, 15 mL) and chilled. PMe$_2$Ph was added (160 mg, 5 equiv) in 2 mL diethyl ether and the brown mixture was stirred at RT for 4 h. The solution was chilled at –35 °C following the addition of 5 ml hexanes. Some crystalline product was obtained and washed with hexanes (72 mg) and additional product was precipitated by addition of the solution to 30 ml hexanes at freeze temperature (106 mg) for a total yield of 65%. X-ray quality crystals were grown from a concentrated solution of benzene at RT. Analytical samples were precipitated from concentrated THF/diether ether solution with excess phosphine at –35 °C. ^{1}H NMR (C_6D_6, 500 MHz, δ, ppm): 29, 17, 13, 11, 9, 0, -2, -9, -17, -18, -20. UV-vis (benzene) (λ_{max}/nm ((ε/M^{-1}cm^{-1}) 490 (6600, sh) 730 (2300, sh). Anal. Calcd for $C_{65}H_{69}Fe_3N_6P_3$: C 65.35, H 5.82, N 7.03. Found: C 65.27, H 5.81, N 6.92.

X-ray Structure Determinations. A single crystal suitable for X-ray analysis was mounted and centered on the tip of a cryoloop attached to a goniometer head. Data for **2** were collected at 100 K, 150 K, 200 K, 250 K and 300 K on an APEX II CCD single crystal diffractometer on a single crystal, warming at a rate of 120 K/h between collections. Cell parameters were determined using the program SMART.[46] Data reduction and integration were performed with the software package SAINT,[47] while absorption corrections were applied using the program SADABS.[48] Space groups were assigned unambiguously by analysis of symmetry, and systematic absences were determined by XPREP. The positions of the heavy atoms were found via direct methods using the program SHELXTL.[49] Subsequent cycles of least-squares refinement followed by difference Fourier syntheses revealed the positions of the remaining non-hydrogen atoms. Hydrogen atoms were added in idealized positions. Non-hydrogen atoms were refined with anisotropic displacement parameters. The space group for **3** was confirmed by

Platon. Crystallographic data are given in Tables 2.7-2.8 and selected bond distances and angles for **2** in Table 2.9.

Table 2.7. X-ray Crystallographic Data for **1**, **2** and **3**.

Chemical formula	$C_{53}H_{60}Fe_3N_6O_3 \cdot 1.75 (C_4H_8O)$	$C_{56}H_{51}Fe_3N_9 \cdot 2(C_6H_6)$	$C_{65}H_{69}Fe_3N_6P_3$
FW	1122.80	1173.82	1194.73
Space group	*C2/c*	$P\bar{1}$	*P2(1)/c*
a (Å)	21.1077(18)	11.805(2)	12.403(3)
b (Å)	15.5695(13)	12.980(2)	20.060(4)
c (Å)	33.842(3)	19.363(4)	22.036(5)
α (deg)	90	73.794(3)	90
β (deg)	98.773(6)	86.132(3)	90
γ (deg)	90	75.907(3)	90
V (Å^3)	10991.5(16)	2763.4(9)	5483(2)
Z	8	2	4
d_{calcd} (g·cm^{-3})	1.357	1.411	1.447
μ (mm^{-1})	0.835	0.83	0.920
T (K)	193(2)	100(2)	100(2)
R1^a (wR2^b)	0.0635 (0.1819)	0.0733 (0.1461)	0.0625 (0.1096)

Table 2.8. X-ray Crystallographic Data of **2** from 100-300 K.

Chemical formula	$C_{56}H_{51}Fe_3N_9 \cdot 2(C_6H_6)$	$C_{56}H_{51}Fe_3N_9 \cdot 2(C_6H_6)$	$C_{56}H_{51}Fe_3N_9 \cdot 2(C_6H_6)$	$C_{56}H_{51}Fe_3N_9 \cdot 2(C_6H_6)$	$C_{56}H_{51}Fe_3N_9 \cdot 2(C_6H_6)$	$C_{56}H_{51}Fe_3N_9 \cdot 2(C_6H_6)$
fw	1173.82	1173.82	1173.82	1173.82	1173.82	1173.82
Space group	$P\bar{1}$	$P\bar{1}$	$P\bar{1}$	$P\bar{1}$	$P\bar{1}$	$P\bar{1}$
a (Å)	11.805(2)	11.839(4)	11.8394(18)	11.888(3)	11.881(3)	11.8228(15)
b (Å)	12.980(2)	13.026(5)	13.037(2)	13.106(3)	13.093(4)	13.0025(16)
c (Å)	19.363(4)	19.436(7)	19.508(3)	19.649(4)	19.706(6)	19.398(3)
α (deg)	73.794(3)	73.818(6)	73.852(3)	73.904(4)	73.971(5)	73.786(2)
β (deg)	86.132(3)	86.197(7)	86.214(3)	86.251(4)	86.265(5)	86.134(3)
γ (deg)	75.907(3)	75.893(7)	75.811(3)	75.708(4)	75.654(5)	75.919(7)
V (Å^3)	2763.4(9)	2791.6(18)	2804.0(7)	2850.5(11)	2854.3(14)	2777.3(6)
Z	2	2	2	2	2	2
d_{calcd} (g·cm^{-3})	1.411	1.396	1.39	1.368	1.366	1.404
μ (mm^{-1})	0.83	0.822	0.818	0.805	0.804	0.826
T (K)	**100(2)**	**150(2)**	**200(2)**	**250(2)**	**300(2)**	**100(2)**
R1^a (wR2^b)	0.0733 (0.1461)	0.0678 (0.1188)	0.0568 (0.1007)	0.0597 (0.1117)	0.0691 (0.1229)	0.0954 (0.2017)

[a] $R1 = [\sum w(F_o - F_c)^2 / \sum w F_o^2]^{1/2}$.

[b] $wR2 = [\sum [w(F_o^2 - F_c^2)^2] / \sum w(F_o^2)^2]^{1/2}$, $w = 1/[\sigma^2(F_o^2) + (aP)^2 + bP]$, where $P = [\max(F_o^2, 0) + 2(F_c^2)]/3$.

Table 2.9. Selected Core Bond Distances (Å) of **2** from 100-300 K.

Temperature (K)	100	150	200	250	300
Fe(1)–Fe(2)	2.6074(6)	2.5981(10)	2.5898(6)	2.5967(7)	2.5917(8)
Fe(1)–Fe(3)	2.5466(6)	2.5327(8)	2.5254(5)	2.5357(6)	2.5370(7)
Fe(2)–Fe(3)	2.5756(6)	2.5658(10)	2.5648(6)	2.5757(7)	2.5765(8)
Fe(1)–N(1L)	2.091(2)	2.108(2)	2.110(2)	2.117(2)	2.116(2)
Fe(2)–N(2L)	2.115(2)	2.124(2)	2.126(2)	2.136(2)	2.133(2)
Fe(3)–N(3L)	2.119(2)	2.125(2)	2.128(2)	2.127(2)	2.123(3)
Fe(1)–N(2)	2.193(2)	2.194(2)	2.1972(19)	2.200(2)	2.188(2)
Fe(1)–N(3)	2.137(2)	2.138(2)	2.1392(19)	2.143(2)	2.132(2)
Fe(1)–N(5)	2.109(2)	2.111(2)	2.1020(19)	2.108(2)	2.102(2)
Fe(1)–N(6)	2.228(2)	2.224(2)	2.2281(19)	2.242(2)	2.248(2)
Fe(2)–N(1)	2.208(2)	2.203(2)	2.202(2)	2.204(2)	2.193(2)
Fe(2)–N(3)	2.1263(19)	2.134(2)	2.1337(18)	2.144(2)	2.140(2)
Fe(2)–N(4)	2.1277(19)	2.131(2)	2.1346(19)	2.146(2)	2.146(2)
Fe(2)–N(6)	2.146(2)	2.149(2)	2.1388(19)	2.141(2)	2.132(2)
Fe(3)–N(1)	2.078(2)	2.081(2)	2.0871(19)	2.090(2)	2.087(2)
Fe(3)–N(2)	2.0928(19)	2.094(2)	2.0899(19)	2.096(2)	2.092(2)
Fe(3)–N(4)	2.269(2)	2.266(2)	2.2578(19)	2.263(2)	2.250(2)
Fe(3)–N(5)	2.221(2)	2.227(2)	2.2287(19)	2.242(2)	2.243(2)

References Cited

1 This material was adapted with permission from Eames, E. V.; Harris, T. D.; Betley, T. A. *Chem. Sci.* **2012**, *3*, 407. Copyright The Royal Society of Chemistry.

2. (a) Mallah, T.; Thiebaut, S.; Verdaguer, M.; Veillet, P. *Science*, **1993**, *262*, 1554; (b) Ferlay, S.; Mallah, T.; Ouhes, R.; Veillet, P.; Verdaguer, M. *Nature*, **1995**, *378*, 701; (c) Hatlevik, O.; Buschmann, W. E.; Zhang, J.; Manson, J. L.; Miller, J. S. *Adv. Mater.*, **1999**, *11*, 914; (d) Holmes, S. M.; Girolami, G. S.; *J. Am. Chem. Soc.*, **1999**, *121*, 5593; (e) Kaye, S. S.; Choi, H. J.; Long, J. R. *J. Am. Chem. Soc.*, **2008**, *130*, 16921; (f) Dechambenoit, P.; Long, J. R. *Chem. Eur. J.*, **2011**, *40*, 3249 and references therein.

3. (a) Sessoli, R.; Tsai, H. L.; Schake, A. R.; Wang, S.; Vincent, J. B.; Folting, K.; Gatteschi, D.; Christou, G.; Hendrickson, D. N.; *J. Am. Chem. Soc.*, **1993**, *115*, 1804; (b) Sessoli, R.; Gatteschi, D.; Caneschi, A.; Novak, M. A. *Nature*, **1993**, *365*, 141; (c) Gatteschi, D.; Sessoli, R.; Villain, J. *Molecular Nanomagnets*; Oxford University Press: New York, **2006** and references therein; (d) Milios, C. J.; Vinslava, A.; Wernsdorfer, W.; Moggach, S.; Parsons, S.; Perlepes, S. P.; Christou, G.; Brechin, E. K. *J. Am. Chem. Soc.*, **2007**, *129*, 2754; (e) Yoshihara, D.; Karasawa, S.; Koga, N. *J. Am. Chem. Soc.*, **2008**, *130*, 10460; (f) Freedman, D. E.; Jenkins, D. M.; Iavarone, A. T.; Long, J. R. *J. Am. Chem. Soc.*, **2008**, *130*, 2884.

4. (a) Caneschi, A.; Gatteschi, D.; Lalioti, N.; Sangregorio, C.; Sessoli, R.; Venturi, G.; Vindigni, A.; Rettori, A.; Pini, M. G.; Novak, M. A. *Angew. Chem., Int. Ed.*, **2001**, *40*, 1760; (b) Clérac, R.; Miyasaka, H.; Yamashita, M.; Coulon, C. *J. Am. Chem. Soc.*, **2002**, *124*, 12837; (c) Lescouëzec, R.; Vaissermann, J.; Ruiz-Pérez, C.; Lloret, F.; Carrasco, R.; Julve, M.; Verdaguer, M.; Dromzée, Y.; Gatteschi, D.; Wernsdorfer, W. *Angew. Chem., Int. Ed.*, **2003**, *42*, 1483; (d) Liu, T. F.; Fu, D.; Gao, S.; Zhang, Y. Z.; Sun, H. L.; Su, G.; Liu, Y. J. *J. Am. Chem. Soc.*, **2003**, *125*, 13976; (e) Coulon, C.; Miyasaka, H.; Clérac, R. *Struct. Bonding (Berlin)*, **2006**, *122*, 163; (f) Bernot, K.; Bogani, L.; Caneschi, A.; Gatteschi, D.; Sessoli, R. *J. Am. Chem. Soc.*, **2006**, *128*, 7947; (g) Miyasaka, H.; Julve, M.; Yamashita, M.; Clérac, R. *Inorg. Chem.*, **2009**, *48*, 3420 and references therein; (h) Harris, T. D.; Bennett, M. V.; Clérac, R.; Long, J. R. *J. Am. Chem. Soc.*, **2010**, *132*, 3980.

5. (a) Clerac, R.; Cotton, F. A.; Dunbar, K. R.; Murillo, C. A.; Pascual, I.; Wang, X. *Inorg. Chem.*, **1999**, *38*, 2655; (b) Berry, J. F.; Cotton, F. A.; Lu, T.; Murillo, C. A.; Roberts, B. K.; Wang, X. *J. Am. Chem. Soc.*, **2004**, *126*, 7082; (c) Berry, J. F.; Cotton, F. A.; Lu, T.; Murillo, C. A.; Roberts, B. K.; Wang, X. *J. Am. Chem. Soc.*, **2004**, *126*, 7082; (d) Berry, J. F. *Struct. Bonding (Berlin)*, **2010**, *136*, 1 and references therein.

6. (a) Hush, N. S. *Prog. Inorg. Chem.*, **1967**, *8*, 391; (b) Creutz, C. *Prog. Inorg. Chem.*, **1983**, *30*, 1; (c) Demadis, K. D.; Hartshorn, C. M.; Meyer, T. J. *Chem. Rev.*, **2001**, *101*, 2655; (d) Brunschwig, B. S.; Creutz, C.; Sutin, N. *Chem. Soc. Rev.*, **2002**, *31*, 168; (e) D'Alessandro, D. M.; Keene, F. R. *Chem. Soc. Rev.*, **2006**, *35*, 424.

7. (a) Drüeke, S.; Chaudhuri, P.; Pohl, K.; Wieghardt, K.; Ding, X.-Q.; Bill, E.; Sawaryn, A.; Trautwein, A. X.; Winkler, H.; Gurman, S. J. *Chem. Commun.*, **1989**, 59; (b) Beissel, T.; Birkelbach, F.; Bill, E.; Glaser, T.; Kesting, F.; Krebs, C.; Weyhermüller, T.; Wieghardt, K.; Butzlaff, C.; Trautwein, A. X. *J. Am. Chem. Soc.*, **1996**, *118*, 12376; (c) Shores, M. P.; Long, J. R. *J. Am. Chem. Soc.*, **2002**, *124*, 3512; (d) Bechlars, B.; D'Alessandro, D. M.; Jenkins, D. M.; Iavarone, A. T.; Glover, S. D.;. Kubiak, C. P; Long, J. R. *Nat. Chem.*, **2010**, *2*, 362.

8. Chernyaev, I. I.; Shenderetskaya, E. V.; Koryagina, A. A. *Zh. Neorg. Khim.*, **1960**, *5*, 1163.

9. (a) Cotton, F. A.; Curtis, N. F.; Harris, C. B.; Johnson, B. F. G.; Lippard, S. J.; Mague, J. T.; Robinson, W. R.; Wood, J. S. *Science*, **1964**, *145*, 1305; (b) Cotton, F. A.; Walton, R. A. "*Multiple Bonds Between Metal Atoms*," Oxford (Oxford): **1993**.

10. Nguyen, T.; Sutton, A. D.; Brynda, M.; Fettinger, J. C.; Long, G. J.; Power, P. P. *Science*, **2005**, *310*, 844.

11. (a) Cotton, F. A. *Acc. Chem. Res.*, **1978**, *11*, 225; (b) Cotton, F. A.; Murillo, C. A.; Walton, R. A. Eds. *Multiple Bonds Between Metal Atoms. 3rd. Ed.*; Springer Science: New York, **2005**; pp. 447-451.

12. Cotton, F. A. *Acc. Chem. Res.*, **1969**, *2*, 240.

13. (a) Venkateswara Rao, P.; Holm, R. H. *Chem. Rev.*, **2004**, *104*, 527; (b) Lee, S. C.; Holm, R. H. *Chem. Rev.*, **2004**, *104*, 1135; (c) Shatruk, M.; Avendano, C.; Dunbar, K. in *Progress in Inorganic Chemistry*, ed. K. D. Karlin, John Wiley & Sons, Amsterdam, **2009**, vol. 56, pp. 155.

14. (a) Baikie, P. E.; Mills, O. S. *Inorg. Chim. Acta*, **1967**, *1*, 55; (b) Kisch, H.; Reisser, P.; Knoch, F. *Chem. Ber.*, **1991**, *124*, 1143; (c) Keen, A. L.; Doster, M.; Han, H.; Johnson, S. A. *Chem. Commun.*, **2006**, 1221; (d) Hatnean, J. A.; Raturi, R.; Lefebvre, J.; Leznoff, D. B.; Lawes, G.; Johnson, S. A. *J. Am. Chem. Soc.*, **2006**, *128*, 14992; (e) Brown, E. C.; Johnson, B.; Palavicini, S.; Kucera, B. E.; Casella, L.; Tolman, W. B. *Dalton Trans.*, **2007**, 3035; (f) Tsui, E. Y.; Day, M. W.; Agapie, T. *Angew. Chem., Int. Ed.*, **2011**, *50*, 1668.

15. Zhao, Q.; Betley, T. A. *Angew. Chem., Int. Ed.*, **2011**, *50*, 709.

16. (a) Powers, T. M.; Fout, A. R.; Zheng, S.-L.; Betley, T. A. *J. Am. Chem. Soc.*, **2011**, *133*, 3336; (b) Powers, T. M.; Betley, T. A. *Unpublished results.*

17. (a) Zhao, Q.; Harris, T. D.; Betley, T. A. *J. Am. Chem. Soc.*, **2011**, *133*, 8293; (b) Harris, T. D.; Zhao, Q.; Hernández Sánchez, R.; Betley, T. A. *Chem. Commun.*, **2011**, *47*, 6344. (c) Harris, T. D.; Betley, T. A. *J. Am. Chem. Soc.* **2011**, *133*, 13852.

18. (a) Balch, A. L.; Holm, R. H. *J. Am. Chem. Soc.*, **1966**, *88*, 5201; (b) Warren, L. F. *Inorg. Chem.*, **1977**, *16*, 2814; (c) Anillo, A.; Diaz, M. R.; Garcia-Granda, S.; Obeso-Rosete, R.; Galindo, A.; Ienco, A.; Mealli, C. *Organometallics*, **2004**, *23*, 471; (d) Bill, E.; Bothe, E.; Chaudhuri, P.; Chlopek, K.; Herebian, K.; Kokatam, S.; Ray, K.; Weyhermüller, T.; Neese, F.; Wieghardt, K. *Chem. Eur. J.*, **2005**, *11*, 204; (e) Chlopek, K.; Bill, E.; Weyhermüller, T.; Wieghardt, K. *Inorg. Chem.*, **2005**, *44*, 7087.

19. (a) Wucherer, E. J.; Tasi, M.; Hansert, B.; Powell, A. K.; Garland, M.-T.; Halet, J.-F.; Saillard, J.-Y.; Vahrenkamp, H. *Inorg Chem.*, **1989**, *28*, 3564; (b) Gao, H.-R.; Mak, T. C. W.; Kang, B.-S.; Wu, B.-M.; Xu, Y.-J.; Tong, Y.-X.; Yu, X.-L. *J. Chem. Res. S.*, **1996**, *5*, 186; (c) Kim, M.; Han, J. *Polyhedron*, **2007**, *26*, 2949; (d) Hess, C. R.; Weyhermüller, T.; Bill, E.; Wieghardt, K. *Angew. Chem. Int. Ed.*, **2009**, *48*, 3703.

20. Bart, S. C.; Lobkovsky, E.; Bill, E.; Wieghardt, K.; Chirik, P. *Inorg. Chem.*, **2007**, *46*, 7055.

21. Watson, R. E.; Freeman, A. J. *Phys. Rev.*, **1960**, *120*, 1125.

22. Borrás-Almenar, J. J.; Clemente-Juan, J. M.; Coronado, E.; Tsukerblat, B. S. *J. Comput. Chem.*, **2001**, *22*, 985.

23. Chakrabarti, M.; Deng, L.; Holm, R. H.; Münck, E.; Bominaar, E. L. *Inorg. Chem.*, **2009**, *48*, 2735.

24. Cotton, F. A.; Daniels, L. M.; Matonic, J. H.; Murillo, C. A. *Inorg. Chim. Acta*, **1997**, *256*, 277.

25. (a) Ding, X.-Q.; Bominaar, E. L.; Bill, E.; Winkler, H.; Trautwein, A. X.; Drüeke, S.; Chaudhuri, P.; Wieghardt, K. *J. Chem. Phys.*, **1990**, *92*, 178; (b) Dutta, S. K.; Ensling, J.; Werner, R.; Flörke, U.; Haase, W.; Gütlich, P.; Nag, K. *Angew. Chem., Int. Ed.*, **1997**, *36*, 152; (c) LeCloux, D. D.; Davydov, R.; Lippard, S. J. *J. Am. Chem. Soc.*, **1998**, *120*, 6810; (d) Lee, D.; Krebs, C.; Huynh, B. H.; Hendrich, M.; Lippard, S. J. *J. Am. Chem. Soc.*, **2000**, *122*, 5000; (e) Hazra, S.; Sasmal, S.; Fleck, M.; Grandjean, F.; Sougrati, M. T.; Ghosh, M.; Harris, T. D.; Bonville, P.; Long, G. J.; Mohanta, S. *J. Chem. Phys.*, **2011**, *134*, 174507.

26. Shores, M. P.; Sokol, J. J.; Long, J. R. *J. Am. Chem. Soc.*, **2002**, *124*, 2279.

27. (a) Hodgson, D. J. *Prog. Inorg. Chem.*, **1975**, *19*, 173 and references therein; (b) Hatfield, W. E. in *Magnetostructural Correlations in Exchange Coupled Systems*, NATO ASI Series. Reidel, Dordrecht, **1985**. R. D. Willett, D. Gatteschi, eds.

28. (a) Real, J. A.; Castro, I.; Bousseksou, A.; Verdaguer, M.; Burriel, R.; Castro, M.; Linares, J.; Varret, F. *Inorg. Chem.*, **1997**, *36*, 455; (b) Létard, J.-F.; Real, J. A.; Moliner, N.; Gaspar, A. B.; Capes, L.; Cador, O.; Kahn, O. *J. Am. Chem. Soc.*, **1999**, *121*, 10630; (c) Moliner, N.; Muńoz, M. C.; Létard, J.-F.; Salmon, L.; Tuchagues, J.-P.; Bousseksou, A.; Real, J. A. *Inorg. Chem.*, **2002**, *41*, 6997; (d) Shatruk, M.; Dragulescu-Andrasi, A.; Chambers, K. E.; Stoian, S. A.; Bominaar, E. L.; Achim, C.; Dunbar, K. R. *J. Am. Chem. Soc.*, **2007**, *129*, 6104.

29. Alvarez, S. *J. Am. Chem. Soc.*, **2003**, *125*, 6795.

30. Kahn, O. *Molecular Magnetism*; VCH: New York, **1993**.

31. The fit for **2** corresponds to $\chi_M T_{LS}$ = 3.08 cm^3·K/mol (g_{LS} = 2.03) and $\chi_M T_{LS}$ = 12.0 cm^3·K/mol (g_{HS} = 2.19).

32. (a) Bennett, M. J.; Caulton, K. G.; Cotton, F. A. *Inorg. Chem.*, **1969**, *8*, 1; (b) Angaridis, P.; Cotton, F. A.; Murillo, C. A.; Villagrán, D.; Wang, X. *J. Am. Chem. Soc.*, **2005**, *127*, 5008; (c) Barral, M. C.; Gallo, T.; Herrero, S.; Jiménez-Aparicio, R.; Torres, M. R.; Urbanos, F. A. *Inorg. Chem.*, **2006**, *45*, 3639; (d) Barral, M. C.; Gallo, T.; Herrero, S.; Jiménez-Aparicio, R.; Torres, M. R.; Urbanos, F. A. *Chem. Eur. J.*, **2007**, *13*, 10088.

33. Hoffert, W. A.; Rappé, A. K.; Shores, M. P. *Inorg. Chem.*, **2010**, *49*, 9497.

34. Clérac, R.; Cotton, F. A.; Dunbar, K. R.; Lu, T.; Murillo, C. A.; Wang, X. *J. Am. Chem. Soc.*, **2000**, *122*, 2272.

35. (a) Cotton, F. A.; Murillo, C. A.; Wang, X. *Inorg. Chem.*, **1999**, *38*, 6294; (b) Clérac, R.; Cotton, F. A.; Dunbar, K. R.; Lu, T.; Murillo, C. A.; Wang, X. *Inorg. Chem.*, **2000**, *39*, 3065; (c) Clérac, R.; Cotton, F. A.; Daniels, L. M.; Dunbar, K. R.; Kirschbaum, K.; Murillo, C. A.; Pinkerton, A. A.;. Schultz, A. J; Wang, X. *J. Am. Chem. Soc.*, **2000**, *122*, 6226; (d) Clérac, R.; Cotton, F. A.; Daniels, L. M.; Dunbar, K. R.; Murillo, C. A.; Wang, X. *Inorg. Chem.*, **2001**, *40*, 1256.

36. (a) Otsuka, S.; Nakamura, A.; Yoshida, T.; *Inorg. Chem.*, **1968**, 7, 261; (b) Sorai, M.; Kosaki, A.; Suga, H.; Seki, S.; Yoshida, T.; Otsuka, S. *Bull. Chem. Soc. Jap.*, **1971**, *44*, 2364; (b) Frisch, P. D.; Dahl, L. F. *J. Am. Chem. Soc.*, **1972**, *94*, 5082; (c) Barnes, C. E.; Dial, M. R. *Organometallics*, **1988**, *7*, 782; (d) Barnes, C. E.; Orvis, J. A.; Staley, D. L.; Rheingold, A. L.; Johnson, D. C. *J. Am. Chem. Soc.*, **1989**, *111*, 4992.

37. Attempts to model the magnetic susceptibility for compound **3** using various exchange models failed to reproduce the data, see Figures 2.16-2.18.

38. The fit for **3** corresponds to $\chi_M T_{LS}$ = 3.58 cm^3·K/mol (g_{LS} = 2.19) and $\chi_M T_{HS}$ = 14.4 cm^3·K/mol (g_{HS} = 2.40).

39. Litterst, F. J.; Amthauer, G. *Phys. Chem. Minerals*, **1984**, *10*, 250.

40. (a) Bertrand, J.; Cotton, F. A.; Dollase, W. A. *J. Am. Chem. Soc.*, **1963**, *85*, 1349; (b) Cotton, F. A.; Haas, T. E. *Inorg. Chem.*, **1964**, *3*, 10.

41. (a) Johansson, G.; Lipscomb, W. N. *Acta Crystallogr.*, **1958**, *11*, 594; (b) Foust, A. S.; Dahl, L. F. *J. Am. Chem. Soc.*, **1970**, *92*, 7337; (c) Simon, G. L.; Dahl, L. F. *J. Am. Chem. Soc.*, **1973**, *95*, 2164; (d) Simon, G. L.; Dahl, L. F. *J. Am. Chem. Soc.*, **1973**, *95*, 2175; (e) Chu, C. T.-W.; Gall, R. S.; Dahl, L. F. *J. Am. Chem. Soc.*, **1982**, *104*, 737; (f) Hoffman, G. G.; Bashkin, J. K.; Karplus, M. *J. Am. Chem. Soc.*, **1990**, *112*, 8705; (g) Agresti, A.; Acci, M.; Cecconi, F.; Ghilardi, C. A.; Midollini, S. *Inorg. Chem.*, **1985**, *24*, 689; (h) Bencini, A.; Ghilardi, C. A.; Midollini, S.; Orlandini, A.; Russo, U.; Uytterhoeven, M. G.; Zanchini, C. *J. Chem. Soc., Dalton Trans.*, **1995**, 963.

42. Zhao, Q.; Betley, T. A. *Angew. Chem. Int. Ed.*, **2011**, *50*, 709.

43. Andersen, R. A.; Faegri, K.; Green, J. C.; Haaland, A.; Lappert, M. F.; Leung, W.-P.; Rypdal, K., *Inorg. Chem.* **1988,** *27*, 1782.

44. Klose, A.; Solari, E.; Ferguson, R.; Floriani, C.; Chiesi-Villa, A.; Rizzoli, C. *Organometallics* **1993**, *12*, 2414.

45. Litterst, F. J.; Amthauer, G., *Phys Chem Minerals* **1984**, *10*, 250.

46. SMART V 5.05 Software for the CCD Detector System; Bruker Analytical X-ray System, Inc.: Madison, WI, 1998.

47. SAINT. Data Reduction Software. V 6.36A; Bruker Analytical X-ray System, Inc.: Madison, WI, 2002.

48. SADABS. Bruker/Siemens Area Detector Absorption and Other Corrections. V2.03; Bruker Analytical X-ray System, Inc.: Madison, WI, 2002.

49. Sheldrick, G. M., *SHELXTL. V 6.12*; Bruker Analytical X-ray Systems, Inc.: Madison, WI, 2000.

Chapter 3: Site-Isolated Redox Reactivity in a Trinuclear Iron Complex

3.1 Introduction

While the collective function of polynuclear, metalloenzyme cofactors is well-described,[1] the functions of each individual metal ion within the cofactor are difficult to ascertain. Undoubtedly neighboring metal ions influence cofactor reactivity by altering substrate coordination modes and buttressing redox changes and charge distribution within the cofactor.[1a,2] We[3] and others[4] are pursuing a class of coordination complexes that feature polynuclear cores to elucidate how transition metals can cooperatively mediate redox processes and to establish what types of reactivities are possible with multiple redox reservoirs available. Utilizing a simple, hexadentate amine-based platform, we have observed facile construction of polynuclear complexes. Transamination reaction of divalent metal precursors with the amine ligand afford trinuclear metal complexes with a broad range of molecular spin states ($S = 1 \rightarrow 6$) which vary

Scheme 3.1

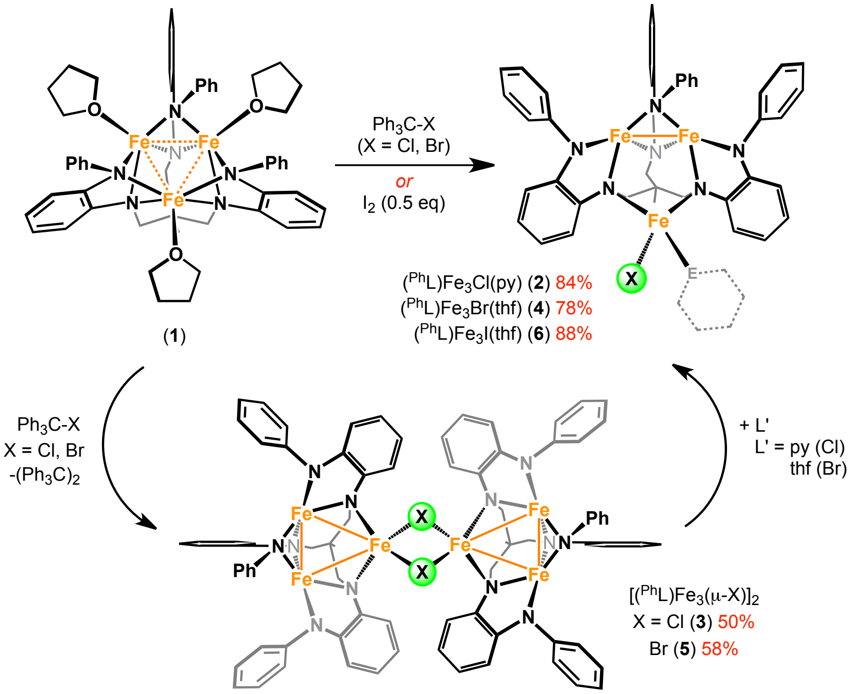

as a function of the ligand architecture.[3a,b,g] In the iron-based complexes, use of the sterically unencumbered proton-capped ligand $(^{H}L)^{6-}$ gave rise to core delocalized redox activity,[3a] whereas use of the silylamide ligand $(^{tbs}L)^{6-}$ gave rise to atom transfer reactivity to the tri-iron core, maintaining an open-shell electronic configuration.[3b] Herein we present redox reactivity of the maximally high-spin (S = 6) triiron complex[3g] $(^{Ph}L)Fe_3(thf)_3$ that gives rise to asymmetric oxidation products where coordination change occurs at an isolated ferrous ion and a distal diiron unit undergoes redox changes.

3.2 Results and Discussion

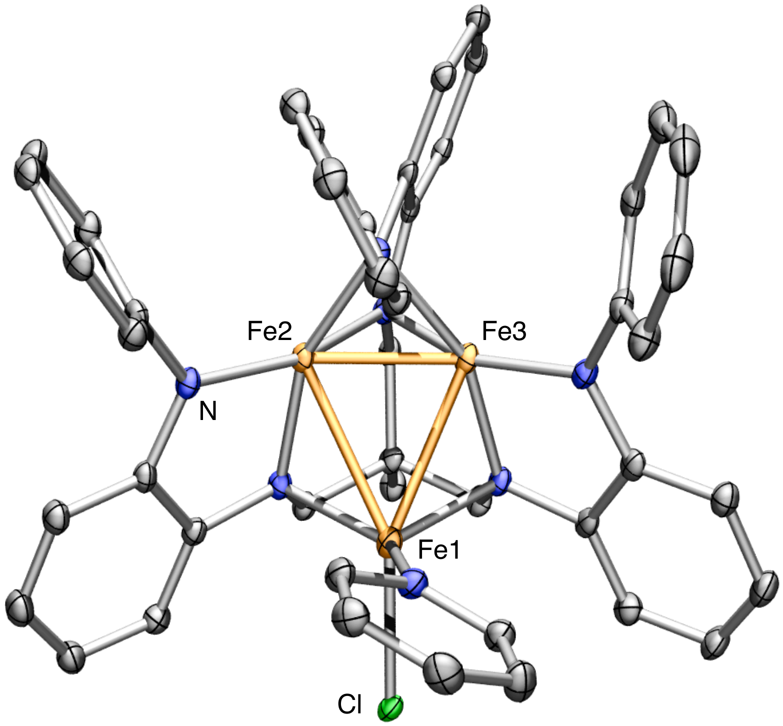

Figure 3.1. Solid-state structure of $(^{Ph}L)Fe_3Cl(py)$ (**2**) with the thermal ellipsoids set at the 50% probability level (solvent molecules and hydrogen atoms omitted for clarity; Fe orange, C black, H white, N blue, Cl green). Bond lengths (Å): Fe1-Fe2, 2.7303(8); Fe1-Fe3, 2.6534(8); Fe2-Fe3, 2.2955(8); Fe1-Cl, 2.3333(11); Fe1-N_{py}, 2.066(3).

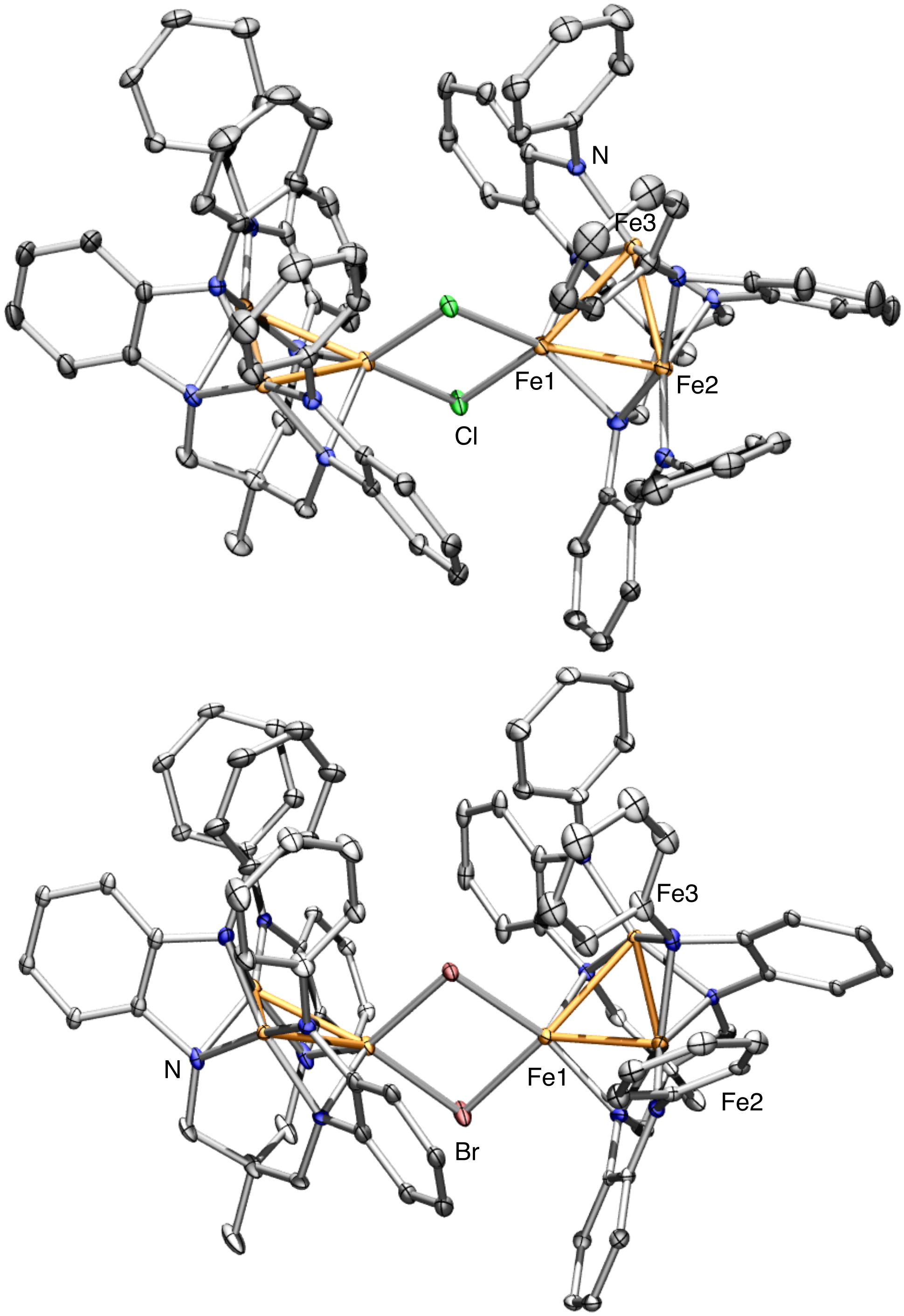

Figure 3.2. Solid-state structure $[(^{Ph}L)Fe_3(\mu\text{-}Cl)]_2$ (**3**), (top) and $[(^{Ph}L)Fe_3(\mu\text{-}Br)]_2$ (**5**), (bottom), with the thermal ellipsoids set at the 50% probability level (solvent molecules and hydrogen atoms omitted for clarity; Fe orange, C black, H white, N blue, Cl green, Br maroon). Bond lengths (Å) for **3**: Fe1-Fe2, 2.5889(5); Fe1-Fe3, 2.5801(5); Fe2-Fe3, 2.3410(5); Fe1-Cl1, 2.3573 (6); Fe1-Cl2, 2.4425(6); for **5**: Fe1-Fe2, 2.5871(7); Fe1-Fe3, 2.5873(7); Fe2-Fe3, 2.3504(7); Fe1-Br1, 2.4670(6); Fe1-Br2, 2.5715(6).

Table 3.1. Selected Core Bond Distances (Å) of **2**-**6**.

Temperature (K)	**2**	**3**	**4**	**5**	**6**
Fe(1)–Fe(2)	2.7303(8)	2.5889(5)	2.7183(10)	2.5871(7)	2.6026(10)
Fe(1)–Fe(3)	2.6534(8)	2.5801(5)	2.7034(10)	2.5873(7)	2.6971(11)
Fe(2)–Fe(3)	2.2955(8)	2.3410(5)	2.3037(10)	2.3504(7)	2.3079(10)
Fe(1)–X	2.3333(11)	2.3573(6)	2.4475(9)	2.4670(6)	2.6695(9)
Fe(1)–L	2.066(3)	2.4425(6)	2.037(3)	2.5715(6)	2.024(4)
Fe(1)–N(2)	2.078(3)	2.081(2)	2.090(4)	2.085(3)	2.081(4)
Fe(1)–N(3)	2.078(4)	2.092(2)	2.097(4)	2.075(3)	2.082(4)
Fe(2)–N(1)	1.924(3)	1.923(2)	1.929(4)	1.926(3)	1.970(4)
Fe(2)–N(3)	1.914(3)	1.9266(19)	1.919(4)	1.937(3)	1.909(4)
Fe(2)–N(4)	1.966(3)	1.978(2)	1.992(4)	1.994(3)	2.073(4)
Fe(2)–N(6)	1.871(3)	1.8552(19)	1.859(4)	1.862(3)	1.869(4)
Fe(3)–N(1)	1.968(4)	1.965(2)	1.954(4)	1.946(3)	1.921(4)
Fe(3)–N(2)	1.900(3)	1.916(2)	1.908(4)	1.916(3)	1.924(4)
Fe(3)–N(4)	2.067(3)	2.059(2)	2.048(4)	2.059(3)	1.977(4)
Fe(3)–N(5)	1.881(4)	1.872(2)	1.889(4)	1.916(3)	1.859(4)

3.2.1 Syntheses and Structures. Chemical oxidation of (^{Ph}L)Fe$_3$(thf)$_3$ (**1**) can be readily affected by treatment with a single equivalent of trityl chloride (Ph$_3$CCl) in tetrahydrofuran, producing a half-equivalent of the quinoid dimer Ph$_3$C(C$_6$H$_5$)CPh$_2$ (identified by ^{1}H NMR, Scheme 3.1).[5] The oxidized trinuclear complex was precipitated from benzene, affording a trinuclear product following treatment with pyridine (^{Ph}L)Fe$_3$Cl(py) (**2**), or the chloride-bridged

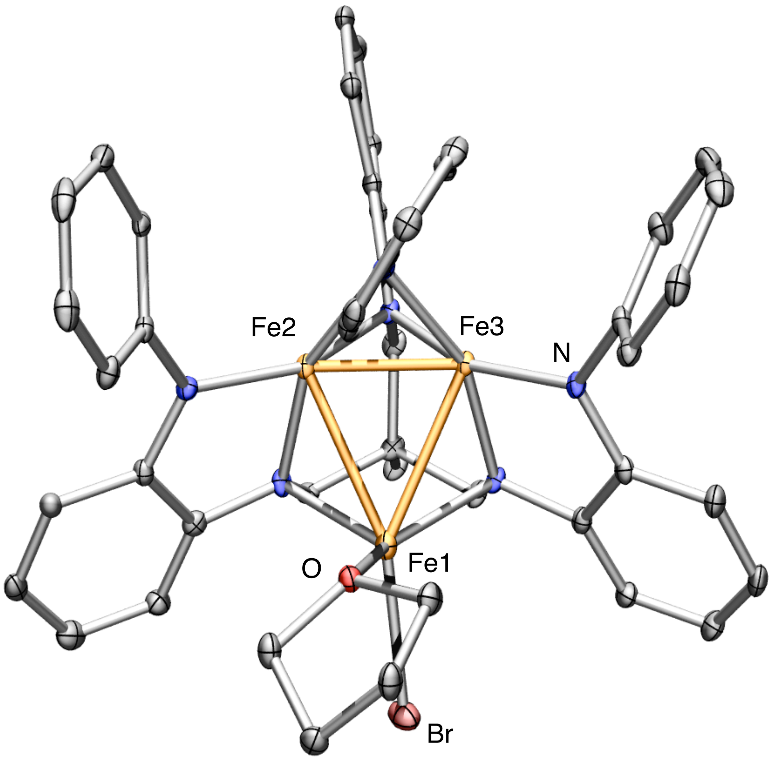

Figure 3.3. Solid-state structure (^{Ph}L)Fe$_3$Br(thf) (**4**) with the thermal ellipsoids set at the 50% probability level (solvent molecules and hydrogen atoms omitted for clarity; Fe orange, C black, H white, N blue, Br maroon). Bond lengths (Å): Fe1-Fe2, 2.7183(10); Fe1-Fe3, 2.7034(10); Fe2-Fe3, 2.3037(10); Fe1-Br, 2.4475(9); Fe1-O, 2.037(3).

product [(^{Ph}L)Fe$_3$(μ-Cl)]$_2$ (**3**). Oxidation of **1** with trityl bromide likewise produced both trinuclear (^{Ph}L)Fe$_3$Br(thf) (**4**) and halide-bridged products [(^{Ph}L)Fe$_3$(μ-Br)]$_2$ (**5**) from tetrahydrofuran or benzene solutions; whereas reaction of **1** with half an equivalent of iodine in tetrahydrofuran exclusively gave the trinuclear product (^{Ph}L)Fe$_3$I(thf) (**6**). Single crystals for X-ray diffraction analysis were obtained by allowing a solution of each compound in benzene to stand at room temperature (**2**, **3**, and **5**), or by cooling (–35 ˚C) a tetrahydrofuran solution (**4** and **6**).

The chemical compositions of the oxidized complexes **2-6** were confirmed by single crystal X-ray diffraction analysis. The solid-state structures for these species are provided in

Figures 3.1-3.4, and bond distances are provided in Table 3.1. For the trinuclear complexes **2**, **4**, and **6**, the molecular structure reveals three salient features: (1) two molecules of tetrahydrofuran are lost from **1**, (2) the hexa-anilide (^{Ph}L) ligand has substantially altered its binding mode, and (3) the halide ligand from chemical oxidation is bound to a single iron ion. The halide-bearing iron ion (Fe1 in Figure 3.1) is nearly trigonal-monopyramidal (neglecting M–M interactions), where two ligand anilides and the pyridine form the trigonal plane and the Cl ion caps the pyramid, positioned *trans* to the diiron portion of the trinuclear core. The remaining two iron ions (Fe2, Fe3) are each bound to four ligand anilide units, forming an intermediate geometry between tetrahedral and square-planar locally at each iron, with a close Fe–Fe contact (Fe2-Fe3 2.2955(8) Å) in the axial site. The two remaining M–M contacts (Fe1-Fe2 2.7303(8) Å, Fe1-Fe3

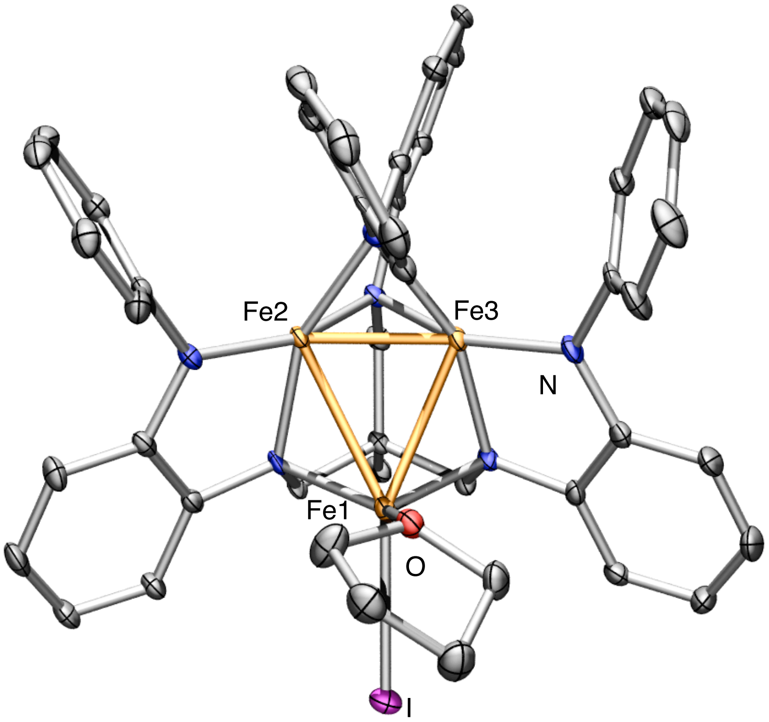

Figure 3.4. Solid-state structure (^{Ph}L)Fe$_3$I(thf) (**6**) with the thermal ellipsoids set at the 50% probability level (solvent molecules and hydrogen atoms omitted for clarity; Fe orange, C black, H white, N blue, I green). Bond lengths (Å): Fe1-Fe2, 2.6026(10); Fe1-Fe3, 2.6971(11); Fe2-Fe3, 2.3079(10); Fe1-I, 2.6695(9); Fe1-O, 2.024(4).

2.6534(8) Å) are substantially elongated compared with average metal ion separation in **1** (2.491 (1) Å).[3g] The trinuclear core asymmetry is maintained in the trinuclear bromide and iodide structures (see Figures 3.3, 3.4), respectively). The bond metrics within the(^{Ph}L) ligand *o*-phenylenediamide units are consistent with the closed-shell dianion state (see Tables 3.2-3.6).[6]

Table 3.2. Selected Ligand Bond Distances (Å) for **2**.

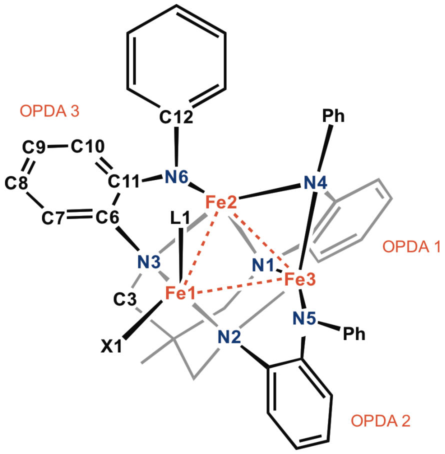

OPDA subunit	**1**	**2**	**3**
C(3)–N(1)	1.460(5)	1.474(5)	1.476(5)
N(1)–C(6)	1.412(5)	1.423(5)	1.434(5)
C(6)–C(7)	1.382(5)	1.385(5)	1.386(6)
C(7)–C(8)	1.388(6)	1.381(6)	1.379(6)
C(8)–C(9)	1.390(6)	1.373(7)	1.391(6)
C(9)–C(10)	1.387(5)	1.378(6)	1.382(6)
C(10)–C(11)	1.385(5)	1.407(6)	1.395(5)
C(6)–C(11)	1.407(6)	1.410(6)	1.413(5)
C(11)–N(4)	1.439(4)	1.387(5)	1.388(5)
N(4)–C(12)	1.427(5)	1.416(6)	1.429(5)

Table 3.3. Selected Ligand Bond Distances (Å) for **3**.

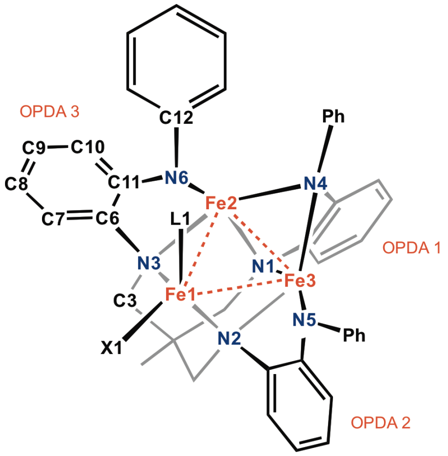

OPDA subunit	**1**	**2**	**3**
C(3)–N(1)	1.465(3)	1.479(3)	1.488(3)
N(1)–C(6)	1.417(3)	1.423(3)	1.431(3)
C(6)–C(7)	1.386(4)	1.389(3)	1.401(3)
C(7)–C(8)	1.389(4)	1.387(4)	1.392(4)
C(8)–C(9)	1.389(5)	1.387(4)	1.398(4)
C(9)–C(10)	1.394(4)	1.395(3)	1.386(4)
C(10)–C(11)	1.386(4)	1.396(3)	1.402(4)
C(6)–C(11)	1.417(3)	1.414(3)	1.407(4)
C(11)–N(4)	1.439(3)	1.387(3)	1.388(3)
N(4)–C(12)	1.429(3)	1.430(3)	1.331(7)

Table 3.4. Selected Ligand Bond Distances (Å) for **4**.

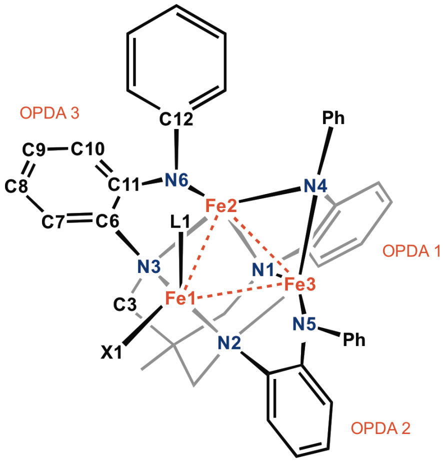

OPDA subunit	**1**	**2**	**3**
C(3)–N(1)	1.468(6)	1.486(6)	1.497(6)
N(1)–C(6)	1.424(6)	1.424(6)	1.431(6)
C(6)–C(7)	1.387(7)	1.391(7)	1.386(7)
C(7)–C(8)	1.393(7)	1.386(7)	1.383(7)
C(8)–C(9)	1.380(7)	1.387(7)	1.374(7)
C(9)–C(10)	1.395(7)	1.390(7)	1.392(7)
C(10)–C(11)	1.384(7)	1.405(6)	1.399(7)
C(6)–C(11)	1.410(6)	1.417(6)	1.409(7)
C(11)–N(4)	1.431(6)	1.373(6)	1.396(6)
N(4)–C(12)	1.441(6)	1.436(6)	1.435(6)

Table 3.5. Selected Ligand Bond Distances (Å) for **5**. Distances are reported for one subunit only, as the others are disordered and bond distances were constrained to 1.39 Å during refinement.

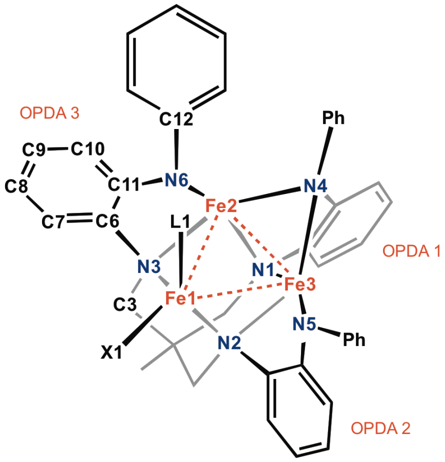

OPDA subunit	**2**
C(3)–N(1)	1.480(4)
N(1)–C(6)	1.426(5)
C(6)–C(7)	1.404(5)
C(7)–C(8)	1.398(6)
C(8)–C(9)	1.382(6)
C(9)–C(10)	1.389(5)
C(10)–C(11)	1.410(5)
C(6)–C(11)	1.412(6)
C(11)–N(4)	1.394(5)
N(4)–C(12)	1.435(4)

Table 3.6. Selected Ligand Bond Distances (Å) for **6**.

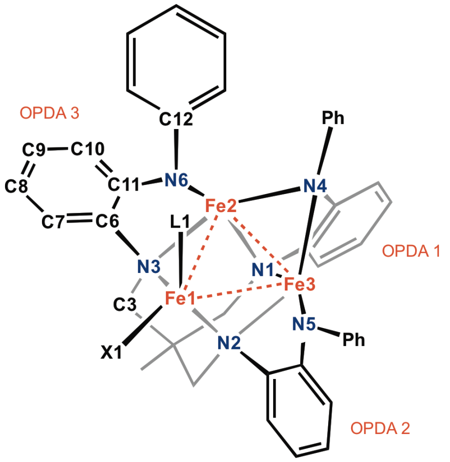

OPDA subunit	**1**	**2**	**3**
C(3)–N(1)	1.452(6)	1.482(6)	1.482(6)
N(1)–C(6)	1.418(6)	1.423(6)	1.417(6)
C(6)–C(7)	1.383(7)	1.410(7)	1.392(7)
C(7)–C(8)	1.389(7)	1.391(7)	1.381(8)
C(8)–C(9)	1.379(8)	1.375(8)	1.398(8)
C(9)–C(10)	1.384(7)	1.388(8)	1.379(8)
C(10)–C(11)	1.394(7)	1.398(7)	1.394(7)
C(6)–C(11)	1.414(7)	1.405(7)	1.410(7)
C(11)–N(4)	1.432(6)	1.394(6)	1.387(7)
N(4)–C(12)	1.426(6)	1.434(6)	1.425(6)

The two hexanuclear products **3** and **5** exhibit the same structural distortions evident in the trinuclear complexes **2**, **4**, and **6**. One iron ion binds the halide ligands, while the (^{Ph}L) ligand distorts to engender nearly square planar binding modes to the two remaining iron ions. The short Fe2-Fe3 contact is maintained in both of the bridged hexanuclear complexes (2.3410(5) Å

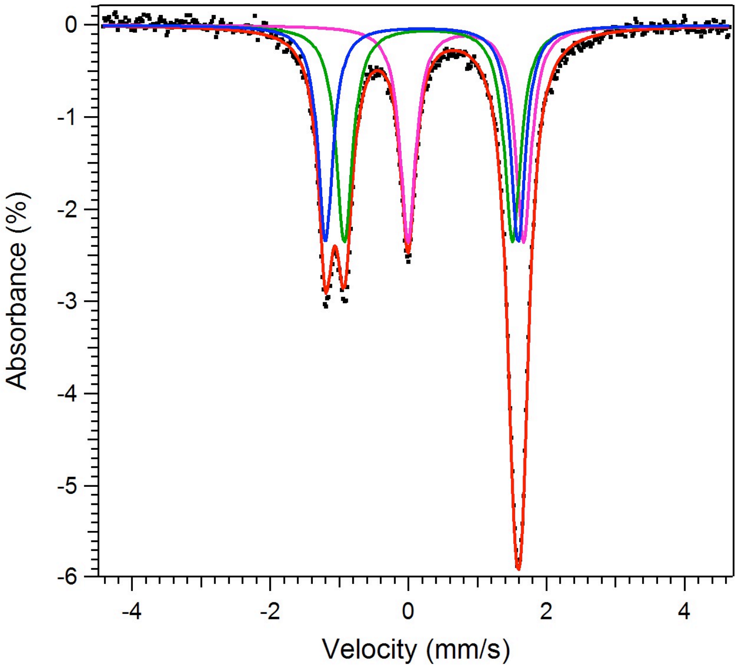

Figure 3.5. Zero-field ^{57}Fe Mössbauer spectrum for **2** obtained at 90 K with spectral fits (δ, |*ΔE$_Q$*| ($^{mm}/_{s}$)) component 1 (magenta): 0.83, *1.67*, 33%; component 2 (green): 0.29, *2.44*, 33%; component 3 (blue): 0.20, 2.79, 33%.

in **3**, 2.3504(7) Å in **5**). While the Fe2-Fe3 ion separation is modestly elongated from the trinuclear species, the average Fe1-Fe2 and Fe1-Fe3 separations are substantially shorter (average (Å): 2.5849(5), **3**; 2.5872(7), **5**) than the distances observed in **2**, **4**, and **6**. The halide bearing iron ion (Fe1 in **3** and **5**, shown in Figure 3.2) is more tetrahedral than the same site in the trinuclear complexes. The dihedral angle between the Br-Fe1-Br and Fe2-Fe1-Fe3 is 67.85° (68.18° in **3**), creating a twist between the two trinuclear subunits.

3.2.2 Mössbauer Spectroscopy. At first glance, chemical oxidation of **1** appears to localize redox changes to the halide-bearing iron site, leaving the remaining two iron sites in a nominally all-ferrous state, suggesting a [Fe$^{II}_2$Fe^{III}] formulation. A representative zero-field ^{57}Fe Mössbauer spectrum obtained at 90 K for complex **2** is presented in Figure 3.5. The spectrum reveals three distinct quadrupole doublets of equal intensity (δ, |*ΔE$_Q$*| ($^{mm}/_{s}$): 0.83, *1.67*, 33%;

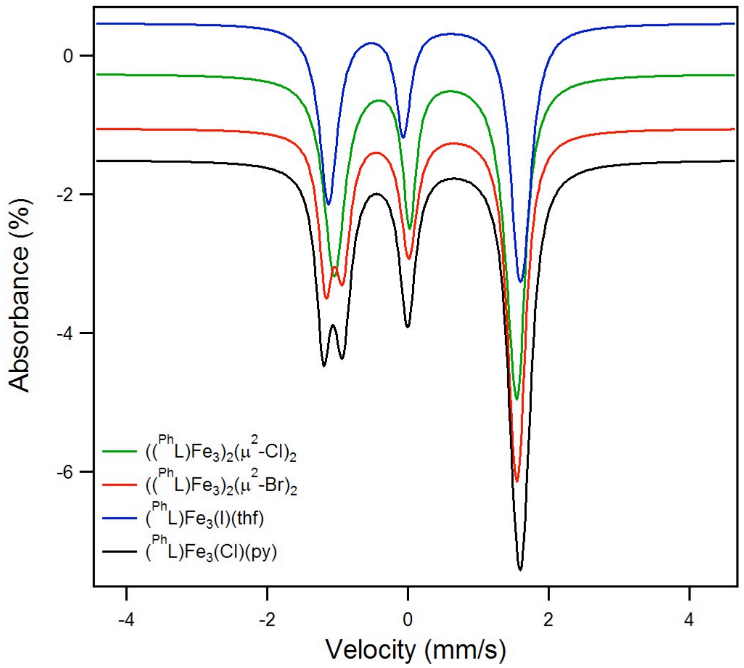

Figure 3.6. Comparison of fits to the zero-field ^{57}Fe Mössbauer spectra for **3-6** obtained at 90 K (δ, $|\Delta E_Q|$ $(^{\mathrm{mm}}/_{\mathrm{s}})$, %). For **3**: 0.79, *1.54*, 33%; 0.22, *2.72*, 33%; 0.26, *2.43*, 33%; for **4**: 0.74, *1.67*, 36%; 0.26, *2.76*, 64%; for **5**: 0.74, *1.49*, 32%; 0.22, *2.76*, 36%; 0.31, *2.46*, 32%; for **6**: 0.81, *1.74*, 36%; 0.22, *2.70*, 64%.

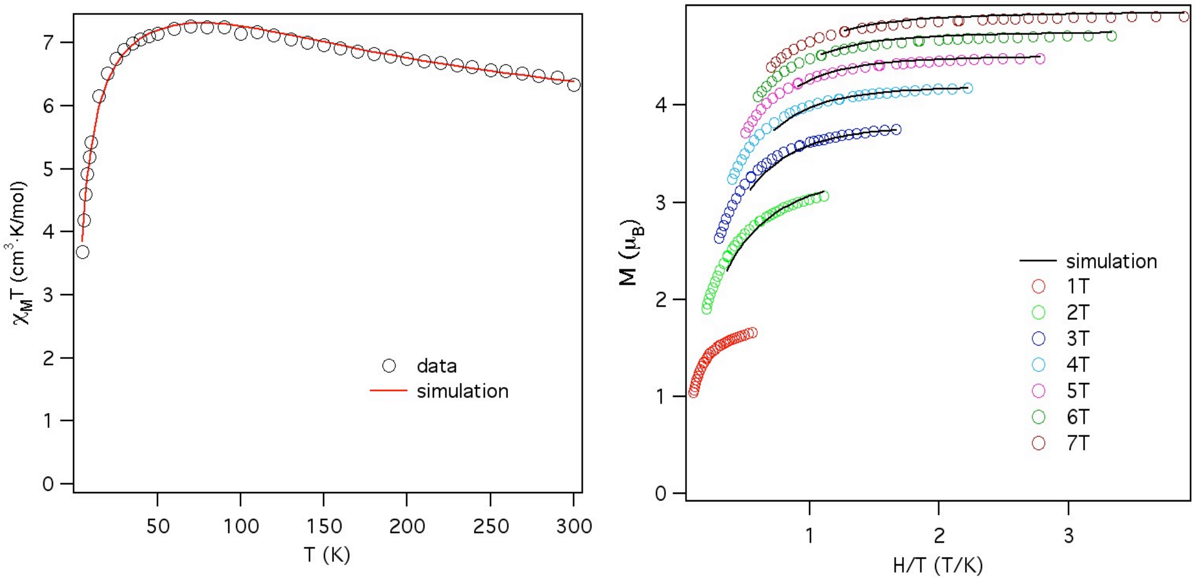

Figure 3.7. Variable-temperature magnetic susceptibility (left) and reduced magnetization (right) data for **2** with simulation ($\boldsymbol{S}_1 = 2$, $\boldsymbol{S}_2 = 3/2$, $J = 16$ cm^{-1}, $D_1 = 36$ cm^{-1}, $D_2 = -47$ cm^{-1}, $g = 2.09$ (susceptibility), $g = 2.02$ (reduced magnetization)).

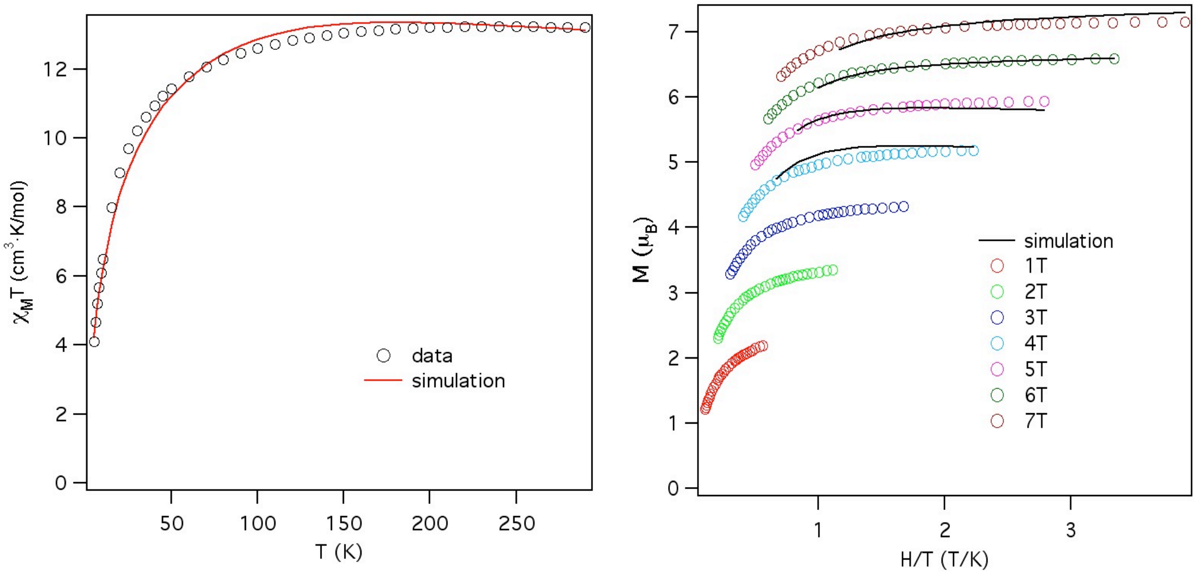

Figure 3.8. Variable-temperature magnetic susceptibility (left) and reduced magnetization (right) data for **3** with simulation ($\boldsymbol{S}_1 = 2$, $\boldsymbol{S}_2 = 3/2$, $J_1 = 15$ cm^{-1}, $J_2 = -1.5$ cm^{-1}, $D_1 = 40$ cm^{-1}, $D_2 = -120$ cm^{-1}, $g = 2.17$ (susceptibility), $g = 1.97$ (reduced magnetization)).

0.29, *2.44*, 33%; 0.20, *2.79*, 33%). The isomer shift of the first component is consistent with a ferrous assignment and is comparable to the isomer shift found in **1** (δ, $|\Delta E_Q|$ ($^{mm}/_{s}$): 0.79, *1.25*).[3g] The two remaining quadrupole doublets are considerably shifted from **1** and feature considerably larger quadrupole splitting parameters. The significantly lowered isomer shift indicates an increase in the formal oxidation state, suggesting oxidation occurs within the diiron unit. The similarity between the isomer shifts for the two ions in the diiron unit indicate the one-electron oxidation is substantially delocalized yielding a mixed-valent diiron unit (i.e., [Fe$_2$]$^{5+}$). Thus, while Fe1 may bear the halide in **2**, the distal di-iron unit (Fe2-Fe3) is the locus of oxidation, giving the formal oxidation assignment as [Fe^{2+}(Fe$_2$)$^{5+}$]. The spectrum for **2** is highly representative of the entire series **3-6** (see Figure 3.6), indicating this oxidation distribution is maintained throughout the series.

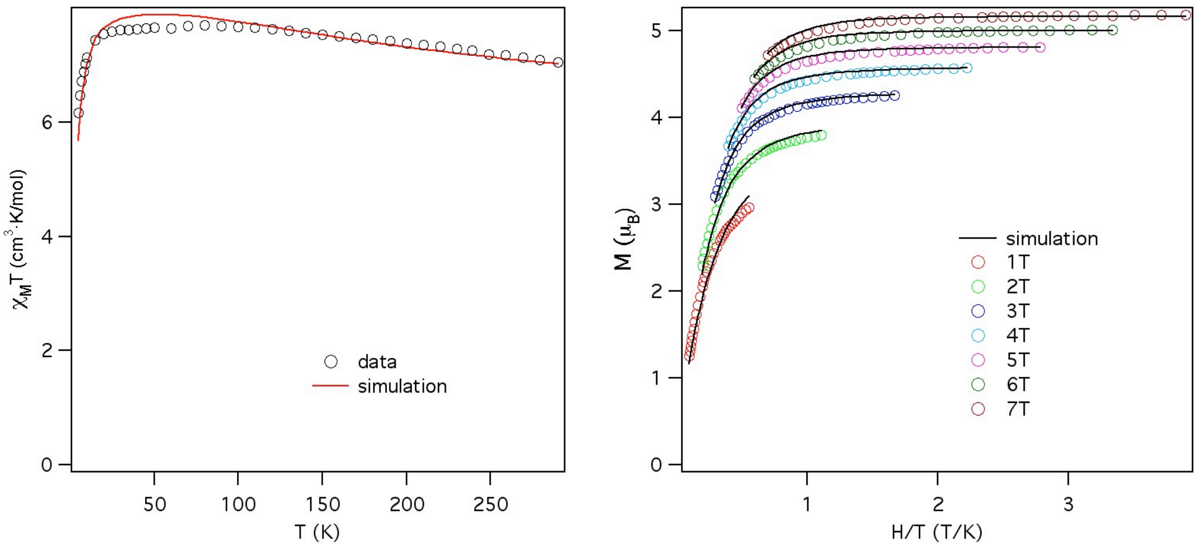

Figure 3.9. Variable-temperature magnetic susceptibility (left) and reduced magnetization (right) data for **4** with simulation ($\boldsymbol{S}_1 = 2$, $\boldsymbol{S}_2 = 3/2$, $J = 12.5$ cm^{-1}, $D_1 = 14$ cm^{-1}, $D_2 = -96$ cm^{-1}, $g = 2.23$ (susceptibility), $g = 2.00$ (reduced magnetization)).

3.2.3 Magnetic Properties. The solution magnetic moments obtained for the soluble trinuclear complexes (e.g., $\mu_{\mathrm{eff}} = 7.94$ μ_B for **2**, 295 K C_6D_6) indicate the oxidized products maintain an open-shell configuration, although reduced from a maximally high-spin state ($S = {}^{13}/_2$), which would exhibit a spin-only moment of 13.96 μ_B. To probe the magnetic behavior of complexes **2-6** further, variable temperature dc susceptibility data were collected in the temperature range of 5-300 K. In the case of **2**, $\chi_M T$ increases from a value of 6.8 cm^3 K mol^{-1} at 300 K to a maximum value of 7.4 cm^3 K mol^{-1} at 70 K (see Figure 3.7). Below 50 K, the data undergo a downturn, likely the result of Zeeman and zero-field splitting. The data for trinuclear bromide **4** and iodide **6** complexes are similar (see Figures 3.9 and 3.11). The data for the hexanuclear, chloride-bridged complex **3** are nearly double that observed for trinuclear **2**. For **3**, $\chi_M T$ exhibits a maximal value of 12.8 cm^3 K mol^{-1} at 300 K, but decreases substantially below temperatures of 120 K (see Figure 3.8). Variable temperature magnetization data were collected for complexes **2-6** in the temperature range of 1.8–10 K at fields of 1 to 7 T. A representative plot

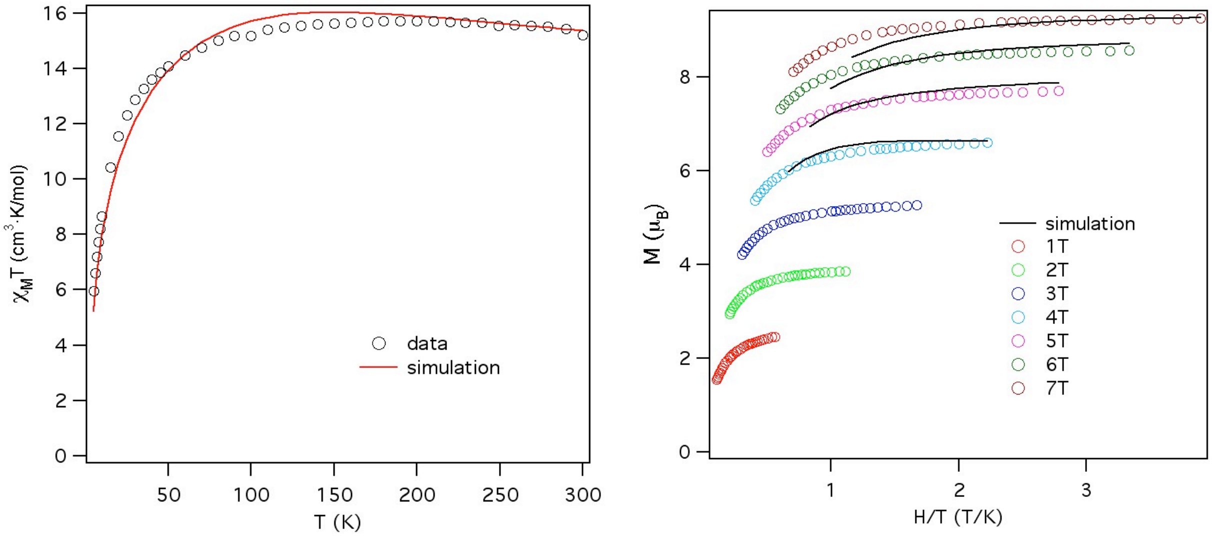

Figure 3.10. Variable-temperature magnetic susceptibility (left) and reduced magnetization (right) data for **5** with simulation ($\boldsymbol{S}_1 = 2$, $\boldsymbol{S}_2 = 3/2$, $J_1 = 20$ cm^{-1}, $J_2 = -1.25$ cm^{-1}, $D_1 = 43$ cm^{-1}, $D_2 = -95$ cm^{-1}, $g = 2.28$ (susceptibility), $g = 2.08$ (reduced magnetization)).

of reduced magnetization for **2** is shown in Figure 3.7, which features a series of non-superimposable isofield curves, with the 7 T curve reaching a maximum value of $M = 4.9$ μ_B at 1.8 K.

Based on the Mössbauer spectra which suggest each of the oxidized trinuclear cores consist of an isolated ferrous site and a mixed-valent dinuclear unit, we modeled the data using the two-spin Hamiltonian shown below (Equation 3.1), where $\boldsymbol{S}_1 = 2$ for the ferrous ion, and $\boldsymbol{S}_2$ represents the mixed-valent diiron unit spin.

$$\hat{H} = -2J(\boldsymbol{S}_1\boldsymbol{S}_2) + \Sigma D_i\boldsymbol{S}_i^2 + g\mu_B\boldsymbol{S}\cdot\boldsymbol{B} \qquad \text{Equation 3.1}$$

The spin state of the diiron $[Fe_2]^{5+}$ unit $\boldsymbol{S}_2$ will fall in the range of ½ for a maximally low-spin state, to $^9/_2$ for a maximally high-spin state.[7] The value of $\boldsymbol{S}_2$ affects data simulations by setting the value for g, as well as modulating the effect D_2 has on the shape of the susceptibility and reduced magnetization curves. Suitable models of the data (where g ≈ 2) were only obtained

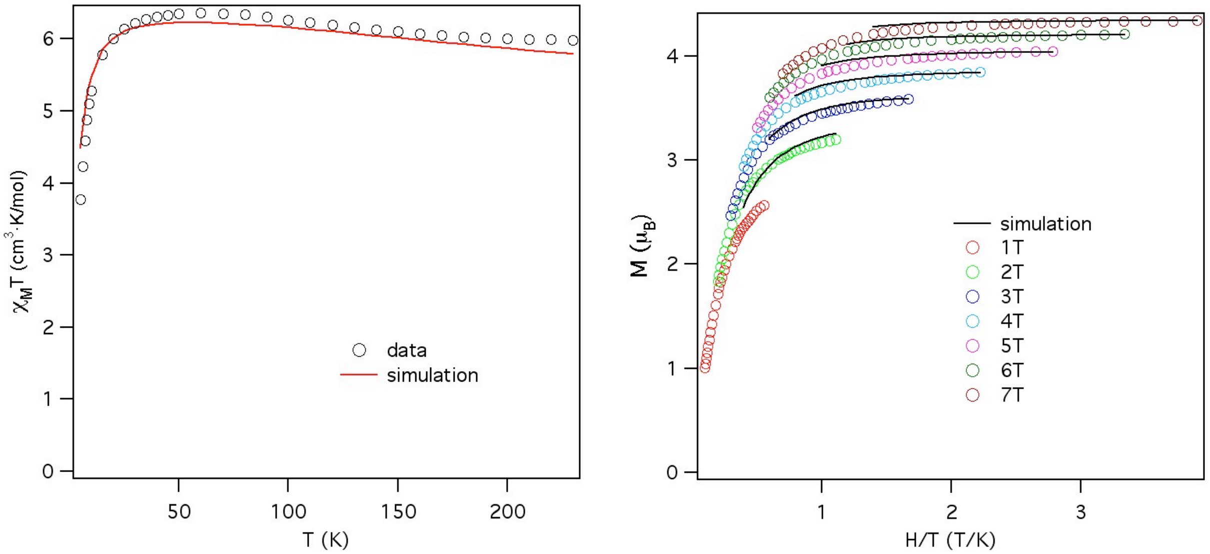

Figure 3.11. Variable-temperature magnetic susceptibility (left) and reduced magnetization (right) data for **6** with simulation ($\boldsymbol{S}_1 = 2$, $\boldsymbol{S}_2 = 3/2$, $J = 15$ cm^{-1}, $D_1 = 14$ cm^{-1}, $D_2 = -110$ cm^{-1}, $g = 2.01$ (susceptibility), $g = 1.79$ (reduced magnetization)).

when $\boldsymbol{S}_2 = {}^3/_2$ was used in equation 1, suggesting a total spin state of $\boldsymbol{S} = {}^7/_2$ for trinuclear complex which is consistent with the room temperature magnetic moments obtained for **2** ($\mu_{\text{spin-only}} = 7.94\ \mu_B$ for $\boldsymbol{S} = {}^7/_2$). The corresponding simulation using the program MAGPACK[8] that best reproduces the susceptibility and reduced magnetization data affords parameters of $J = +16$ cm^{-1}, $D_1 = 36$ cm^{-1}, $D_2 = -47$ cm^{-1}, and $g = 2.09$. Modifying the Hamiltonian spin expression to account for an additional exchange interaction J_2 (between the two trinuclear subunits mediated through the bridging halides in **3**), we modeled the data for **3** using the following expression (Equation 3.2):

$$\hat{H} = -2J_1(\boldsymbol{S}_{1_a}\boldsymbol{S}_{2_a} + \boldsymbol{S}_{1_b}\boldsymbol{S}_{2_b}) - 2J_2(\boldsymbol{S}_{1_a}\boldsymbol{S}_{1_b}) + \Sigma D_i\boldsymbol{S}_i^2 + g\mu_B\boldsymbol{S}\cdot\boldsymbol{B} \qquad \text{Equation 3.2}$$

The simulation that best reproduces the data for **3** affords parameters of $J_1 = +15$ cm^{-1}, $J_2 = -1.5$ cm^{-1}, $D_1 = 40$ cm^{-1}, $D_2 = -120$ cm^{1}, and $g = 2.17$. The weak antiferromagnetic coupling between the trinuclear subunits leads to the $S = 0$ ground state for the hexanuclear, halide-bridged complexes **3** and **5**, contributing to the downturn in the susceptibility data at lower temperatures.

Scheme 3.2

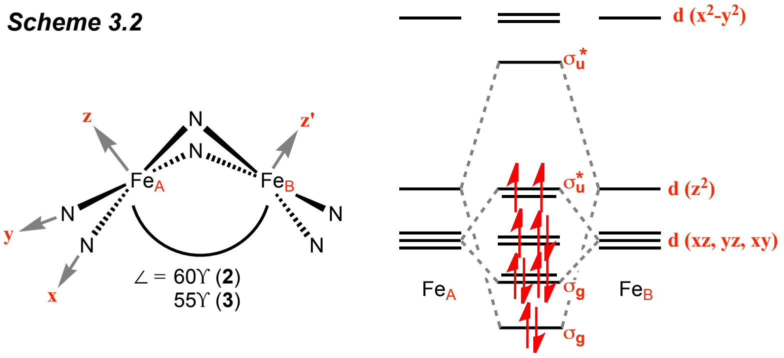

At higher temperatures, the susceptibility data is nearly twice the values observed for trinuclear **2**, consistent with two spin-independent trinuclear subunits in **3**. This assessment is corroborated by the reduced magnetization data for **3** and **5** (see Figures 3.8, 3.10).

3.2.4 Qualitative Electronic Structure. The electronic structure within the trinuclear cores deviates from our previous work, wherein redox was symmetrically distributed within the polynuclear core.[3a,c] In previous examples, bonding metrics within the polynuclear core are affected by direct orbital-orbital interactions between adjacent metal sites. Upon oxidation of the low-spin congener (^{H}L)Fe$_3$(PMe$_3$)$_3$, the contraction observed within the trinuclear core is attributed to depopulation of a nominally antibonding interaction.[3a] In the present case, chemical oxidation of **1** leads to increased metal-metal interaction within the dinuclear site of oxidation, while simultaneously attenuating the interaction with the lone ferrous site. The iron-anilide (Fe-N 2.078(3) Å) and iron-halide bond metrics for Fe1 in **2** are consistent with a high-spin ferrous assignment. The close iron-iron separation in the oxidized diiron unit [Fe$_2$]$^{5+}$ suggests significant M–M orbital overlap. The diiron unit is approximated as two edge-sharing square planar ions giving rise to the direct orbital interactions as illustrated in Scheme 3.2. Population of the eleven valence electrons into this manifold will not fill the three highest lying σ* orbitals, which represent (Fe–N)$_\sigma^*$ and (Fe–Fe)$_\sigma^*$ interactions, the latter arising from the antibonding combination of the Fe d_{z^2}. Consistent with this model, the average Fe–N distance in **2** (1.936(5) Å) are considerably shorter than high-spin **1** (2.176(5) Å) where these orbital interactions are populated.

3.3 Conclusions and Outlook

The above analysis, based on crystallographic, magnetic, and Mössbauer spectral data suggest a new mechanism by which redox is mediated within polynuclear complexes. In the low-spin regime, oxidation is delocalized throughout the trinuclear core. Mössbauer data obtained upon atom-transfer to the high-spin (^{tbs}L)Fe_3(thf) complex suggests the two-electron oxidation incurred upon nitride formation is core-delocalized.[3b] However, the foregoing data describing the chemical oxidation of high-spin (^{Ph}L)$Fe_3(thf)_3$ demonstrate that oxidation leads to a trapped valency within a diiron unit, separate from the apparent site of halide capture, with concomitant rearrangement of the trinucleating ligand. Typically such ligand reorganization presents a large energy barrier, but the maximally high-spin formulation of the all-ferrous precursor creates an inherently labile system. Furthermore, the elucidation of this unusual mode of cooperative redox reactivity demonstrates the potential of polynuclear complexes to provide insight into how redox processes may occur within polynuclear metallocofactors in nature.

3.4 Experimental Section

Materials and Methods. All manipulations involving metal complexes were carried out using standard Schlenk line or glove-box techniques under a dinitrogen atmosphere. All glassware was oven-dried for a minimum of 4 h and cooled in an evacuated antechamber prior to use in the dry box. Benzene, toluene, diethyl ether, hexanes and tetrahydrofuran (THF) were dried and deoxygenated on a Glass Contour System (SG Water USA, Nashua, NH) and stored over 4 Å molecular sieves (Strem) prior to use. Benzene-d_6 and THF-d_8 were purchased from Cambridge Isotope Labs and were degassed and stored over 4 Å molecular sieves prior to use. Non-halogenated solvents were typically tested with a standard purple solution of sodium benzophenone ketyl in THF in order to confirm effective oxygen and moisture removal. MeC($CH_2NHC_6H_4$-*o*-NHPh)$_3$ (^{Ph}L) and (^{Ph}L)Fe_3(THF)$_3$ (**1**) were prepared following published methods.[3g] Anhydrous pyridine was purchased from Aldrich and stored over 4 Å molecular sieves prior to use. Trityl chloride was recrystallized from diethyl ether. All other reagents were purchased from commercial vendors and used without further purification unless explicitly stated.

Physical Measurements. All of the measurements for the metal complexes were made under anaerobic conditions. Elemental analyses were performed by Complete Analysis Laboratories, Inc., Parsippany, New Jersey or Robertson Microlit Laboratories, Madison, New Jersey. ^1H and ^{13}C NMR spectra were recorded on a Varian Unity/Inova 500B or Varian Mercury 400B NMR spectrometer with chemical shifts (δ ppm) referenced to residual NMR solvent. UV/Visible spectra were recorded on a Varian Cary 50 UV/Visible spectrometer using quartz cuvettes. NIR spectra were recorded on a PerkinElmer Lambda 750 high-performance UV-vis spectrometer.

Magnetic measurements were recorded using a Quantum Design MPMS-5S, MPMS-XL or MPMS SQUID VSM magnetometer. Samples were suspended in the magnetometer in folded plastic bags or suspended in eicosane wax contained in Lilly #4 gel capsules, inserted into plastic straws. All manipulations were performed under an atmosphere of dinitrogen. Dc magnetic susceptibility data were collected in the temperature range 2-300 K under fields of 0.1, 0.5, 1 and 2 T. Magnetization data were acquired at 1.8-10 K under fields of 1, 2, 3, 4, 5, 6, and 7 T. Susceptibility data were corrected for the diamagnetic contribution of a blank sample consisting of the bag or wax, capsule and straw at the correct field and temperature. The magnetic susceptibilities were adjusted for diamagnetic contributions using the constitutive corrections from Pascal's constants. The molar magnetic susceptibility (χ_m) was calculated by converting the magnetization (M) obtained from the magnetometer to a molar susceptibility using the multiplication factor [molecular weight (MW)]/[sample weight (m) × field strength (H)]. All samples were measured at least twice. While the shapes of the curves remained constant, the measured values varied by ~10% between samples, likely due some variation in purity. All samples were checked for ferromagnetic impurities by collecting a field dependence curve at 100 K and samples were rejected if any deviation from linearity was observed.

Iron-57 Mössbauer spectra were measured on a constant acceleration spectrometer (SEE Co, Minneapolis, MN) with a Janis SVT-100 cryostat. Isomer shifts are quoted relative to α-Fe foil (< 25 μm thick) at room temperature. Samples were prepared using approximately 30 mg of sample suspended in paratone-N oil. Temperatures were controlled using a LakeShore 321 Autotuning temperature controller. Data were collected at 95 K, with temperature swings no greater than ±10 K, and generally within ±2 K. Data were analyzed using an in-house package written by E. R. King in Igor Pro (Wavemetrics). While it is not possible to definitively and precisely determine the isomer shift and quadrupole splittings in the presence of nearly identical overlapping peaks, the data for each compound were modeled based on the arbitrary assumption that the doublet with greater isomer shift has smaller quadrupole splitting. This yields a simulation in which the isomer shifts, rather than quadrupole splittings, are most nearly equal, a choice which seems justified in light of the fact that in many of the spectra observed, the lowest velocity peaks appear coalesced into a single site. We have previously observed situations in which nearly indistinguishable Fe sites show identical isomer shift and different quadrupole splittings, and this is likely another such case.

Preparation of (^{Ph}L)Fe$_3$Cl(py) (2). A thawing solution of 1% (w/w) pyridine in benzene (1.1 g, 140 μmol, 1.4 equiv) was added to solid **3** (100 mg, 100 μmol, 1 equiv) and stirred for 2h. The resulting solution was filtered to remove a small amount of pale insoluble material (likely a polymerized byproduct) and solvent removed under vacuum. The resulting black powder was collected on a frit, washed with diethyl ether, and dried under vacuum. Yield: 90 mg (84%). X-ray quality crystals were grown from a concentrated filtered solution in benzene at room temperature. ^{1}H NMR (C_6D_6, 500 MHz, δ, ppm): 160, 52, 31, 30, 26, 19, 11, 9, 4.5, -1, -3.5, -27, -77, -89, -92, --153. Anal. Calcd for $C_{46}H_{41}Fe_3N_7Cl$: C 61.74, H 4.62, N 10.96. Found: C 62.06, H 4.58, N 10.82.

Preparation of [(^{Ph}L)Fe$_3$Cl]$_2$ (3). (^{Ph}L)Fe$_3$(THF)$_3$ (300 mg, 301 μmol) was dissolved in THF (100 mL) and frozen. Trityl chloride (88.5 mg, 1.05 equiv) was added in 10 mL THF to the thawing solution and the resulting black solution was immediately placed under vacuum, with stirring, to remove solvent. The dried product was dissolved in benzene and filtered rapidly to remove a pale, insoluble byproduct. The product is only briefly soluble in benzene, apparently because the initial product is benzene-soluble (^{Ph}L)Fe$_3$Cl(THF); as the THF dissociates the insoluble dimer complex **3** comes out of solution. The benzene was removed under vacuum, and more benzene added. Precipitated product was collected on a frit and washed with copious benzene and ether to remove Gomberg's dimer. The washes were dried and the process repeated to collect further batches of product. Yield from first two collections is ~125 mg (50%). NMR is not reported for the dimer, as only the monomeric form is soluble. X-ray quality crystals were grown from a concentrated, filtered benzene solution of the initial soluble product at RT. Anal. Calcd for $C_{41}H_{36}Fe_3N_6Cl$: C 60.37, H 4.45, N 10.30. Found: C 60.29, H 4.34, N 10.21.

Preparation of (^{Ph}L)Fe$_3$Br(THF) (4). Solid **4** (100 mg, 58 μmol, 1 equiv) was dissolved in chilled THF (10 ml) and filtered to remove any insoluble material. The resulting solution was condensed to saturation (~3 ml) and diethyl ether (~7 ml) was added. The solution was stored at –35 °C to promote crystallization. The product was collected on a frit and washed with diethyl ether, then dried under vacuum. Yield: 85 mg (78%). X-ray quality crystals were grown from a concentrated solution in THF at –35 °C. ^{1}H NMR (C_6D_6, 500 MHz, δ, ppm): 104, 58, 43, 40, 32, 30, 20, 17, 13, 11, 9.5, 2, 0, -7, -28, -40, -72, -88, -95, -113, -149, -246. Anal. Calcd for $C_{45}H_{44}Fe_3N_6OBr$: C 57.97, H 4.76, N 9.01. Found: C 57.82, H 4.94, N 8.87.

Preparation of [(^{Ph}L)Fe$_3$Br]$_2$ (5). (^{Ph}L)Fe$_3$(THF)$_3$ (300 mg, 301 μmol) was dissolved in THF (100 mL) and frozen. Trityl bromide (97 mg, 1 equiv) was added in 10 mL THF to the thawing solution and the resulting black solution was immediately placed under vacuum, with stirring, to remove solvent. The dried product was dissolved in benzene and filtered rapidly to remove a pale, insoluble byproduct. The product is only briefly soluble in benzene, apparently because the initial product is benzene-soluble (^{Ph}L)Fe$_3$Br(THF); as the THF dissociates the insoluble dimer complex **5** comes out of solution. The benzene was removed under vacuum, and more benzene added. Precipitated product was collected on a frit and washed with copious benzene and ether to remove Gomberg's dimer. The washes were dried and the process repeated to collect further batches of product. Yield from first two collections is ~150 mg (58%). X-ray quality crystals were grown from a concentrated, filtered benzene solution of the initial soluble product at RT. NMR is not reported for the dimeric complex as only the monomeric form is soluble. Anal. Calcd for $C_{41}H_{36}Fe_3N_6Br$: C 57.25, H 4.22, N 9.77. Found: C 57.14, H 4.15, N 9.72.

Preparation of (^{Ph}L)Fe$_3$I(THF) (6). (^{Ph}L)Fe$_3$(THF)$_3$ (90 mg, 90.3 μmol) was dissolved in THF (25 mL) and frozen. Iodine (11.4 mg, 1 equiv) was added in 5 mL THF to the thawing solution and the resulting black solution was immediately placed under vacuum, with stirring, until the solution had condensed to ~2 ml. The resulting solution was filtered to remove a small amount of pale insoluble material (likely a polymerized byproduct) and additional THF (~2 ml) was added to fully dissolve the product. The solution was condensed to 2 ml again and stored at –35 °C for 4 h. The solution was decanted and the crystalline black product washed twice with cold THF and dried under vacuum. Yield: 50 mg (88%). X-ray quality crystals were grown from a concentrated filtered solution in benzene at room temperature. ^{1}H NMR (C_6D_6, 500 MHz, δ, ppm): 104, 35, 32, 28, 21, 11.6, 10.1, 8.9, -31, -75, -85, -89, -166. Anal. Calcd for $C_{45}H_{44}Fe_3N_6IO$: C 55.19, H 4.53, N 8.58. Found: C 54.89, H 4.46, N 8.54.

X-ray Structure Determinations. A single crystal suitable for X-ray analysis was mounted and centered on the tip of a cryoloop attached to a goniometer head. Cell parameters were determined using the program SMART.[9] Data reduction and integration were performed with the software package SAINT,[10] while absorption corrections were applied using the program SADABS.[11] Space groups were assigned unambiguously by analysis of symmetry, and systematic absences were determined by XPREP.[12] The positions of the heavy atoms were found via direct methods using the program SHELXTL.[13] Subsequent cycles of least-squares refinement followed by difference Fourier syntheses revealed the positions of the remaining non-hydrogen atoms. Hydrogen atoms were added in idealized positions. Non-hydrogen atoms were refined with anisotropic displacement parameters. In disordered structures, phenyl rings were constrained to idealized geometries and anisotropic displacement parameters were restrained as necessary. Crystallographic data are given in Table 3.7.

Modeling of Magnetic Data. The susceptibility and reduced magnetization data were modeled using the package MAGPACK.[8] Simulations were run by canvassing a range of parameter values rather than using a fitting algorithm, due to the computational intensity of the calculations. The spin state values reported are the only ones that produced plausible fits, but the exchange, anisotropy and g parameters reported should not be taken as definitive, as wide ranges of values gave fits of similar quality. (Anisotropy parameters are not in general reliably determined by fitting magnetic data.) Based on the data from Mössbauer spectroscopy, each trinuclear unit was modeled as a high-spin ferrous unit and a single half-integer spin unit for the Fe_2^{5+} pair, which was determined to be $S = 3/2$ based on the simulations. Satisfactory fits were only obtained using distinct, opposite-sign anisotropy parameters (D) for the two spins within each trinuclear unit, with ferromagnetic coupling between them. For the hexanuclear molecules, satisfactory fits required a small antiferromagnetic coupling through the chloride bridges. Where possible, parameter values were chosen to simultaneously optimize the fit to the reduced magnetization and susceptibility data, but no attempt was made to optimize the combined fit in a rigorously quantitative way.

Table 3.7. X-ray Crystallographic Data for **2-6**.

Chemical formula	$C_{46}H_{41}Fe_3N_7Cl\cdot(C_6H_6)$	$[C_{41}H_{36}Fe_3Cl]_2\cdot3.5(C_6H_6)$	$C_{45}H_{44}Fe_3N_6OBr\cdot3(C_4H_8O)$	$[C_{41}H_{36}Fe_3Br]_2\cdot3.5(C_6H_6)$	$C_{45}H_{44}Fe_3N_6OI\cdot1.5(C_6H_6)$
FW	972.97	1904.89	1148.63	1993.81	1096.47
Space group	$P\overline{1}$	*C2/c*	*P2(1)/c*	*C2/c*	$P\overline{1}$
a (Å)	10.6400(14)	20.5157(19)	11.6808(8)	20.5157(19)	12.984(3)
b (Å)	13.8195(18)	16.5388(15)	35.637(2)	16.5388(15)	13.210(3)
c (Å)	17.468(2)	26.062(2)	12.7385(9)	26.062(2)	14.734(3)
α (deg)	99.426(2)	90	90	90	86.701(3)
β (deg)	103.926(2)	99.657(2)	103.8260(10)	99.657(2)	80.278(3)
γ (deg)	111.921(2)	90	90	90	77.288(3)
V (Å^3)	2219.1(5)	8717.7(14)	5149.0(6)	8717.7(14)	2429.3(8)
Z	2	4	4	4	2
d_{calcd} (g·cm^{-3})	1.456	1.451	1.482	1.519	1.499
μ (mm^{-1})	1.074	1.091	1.664	1.946	1.565
T (K)	100(2)	100(2)	100(2)	100(2)	100(2)
R1[a] (wR2[b])	0.0538 (0.1419)	0.0367 (0.1327)	0.0553 (0.1301)	0.0372 (0.0920)	0.0479 (0.1453)

[a] $R1 = [\sum w(F_o - F_c)^2/\sum wF_o^2]^{1/2}$.

[b] $wR2 = [\sum [w(F_o^2 - F_c^2)^2]/\sum w(F_o^2)^2]^{1/2}$, $w = 1/[\sigma^2(F_o^2) + (aP)^2 + bP]$, where $P = [\max(F_o^2,0) + 2(F_c^2)]/3$.

References Cited

1. Nitrogenase: (a) Burgess, B. K.; Lowe, D. J. *Chem. Rev.* **1996**, *96*, 2983-3012. (b) Dos Santos, P. C; Igarashi, R. Y.; Lee, H.-I.; Hoffman, B. M.; Seefeldt, L. C.; Dean, D. R. *Acc. Chem. Res.* **2005**, *38*, 208-214. (c) Hoffman, B. M; Dean, D. R.; Seefeldt, L. C. *Acc. Chem. Res.* **2009**, *42*, 609-619. Photosystem II: (d) Nugent, J., Ed. *Biochim. Biophys. Acta* **2001**, *1503*, 1. (e) Ferreira, K. N.; Iverson, T. M.; Maghlaoui, K.; Barber, J.; Iwata, S. *Science* **2004**, *303*, 1831. (f) Iwata, S.; Barber, J. *Curr. Opin. Struct. Biol.* **2004**, *14*, 447. N_2O reductase: (g) Brown, K.; Djinovic-Carugo, K.; Haltia, T.; Cabrito, I.; Saraste, M.; Moura, J. J. G.; Moura, I.; Tegoni, M.; Cambillau, C. *J. Biol. Chem.* **2000**, *275*, 41133. (h) Brown, K.; Tegoni, M.; Prudêncio, M.; Pereira, A. S.; Besson, S.; Moura, J. J.; Moura, I.; Cambillau, C. *Nat. Struct. Biol.* **2000**, *7*, 191. (i) Chen, P.; George, S. D.; Cabrito, I.; Antholine, W. E.; Moura, J. G.; Moura, I.; Hedman, B.; Hodgson, K. O.; Solomon, E. I. *J. Am. Chem. Soc.* **2002**, *124*, 744.

2. (a) Fontecilla-Camps, J. C. *J. Biol. Inorg. Chem.* **1996**, *96*, 3031. (b) Siegbahn, P. E. M. *Inorg. Chem.* **2000**, *39*, 2923. (c) Huniar, U.; Ahlrichs, R.; Coucouvanis, D. *J. Am. Chem. Soc.* **2004**, *126*, 2588.

3. (a) Zhao, Q.; Betley, T. A. *Angew. Chem. Int. Ed.*, **2011**, *50*, 709-712. (b) Powers, T. M.; Fout, A. R.; Zheng, S.-L.; Betley, T. A. *J. Am. Chem. Soc.* **2011**, *133*, 3336. (c) Zhao, Q.; Harris, T. D.; Betley, T. A. *J. Am. Chem. Soc.* **2011**, *133*, 8293. (d) Harris, T. D.; Zhao, Q.; Hernández Sánchez, R.; Betley, T. A. *Chem. Commun.* **2011**, *47*, 6344. (e) Harris, T. D.; Betley, T. A. *J. Am. Chem. Soc.* **2011**, *133*, 13852. (f) Fout, A. R.; Zhao, Q.; Xiao, D. J.; Betley, T. A. *J. Am. Chem. Soc.* **2011**, *133*, 16750. (g) Eames, E. V.; Harris, T. D.; Betley, T. A. *Chem. Sci.* **2012**, *3*, 407.

4. (a) Adams, R. D. *J. Organometallic Chem.* **2000**, *600*, 1-6. (b) Suzuki, H. *Eur. J. Inorg. Chem.* **2002**, 1009-1023. (c) Dyson, P. J. *Coord. Chem. Rev.* **2004**, *248*, 2443-2458. (d) Pap, J. S.; DeBeer George, S.; Berry, J. F. *Angew. Chem. Int. Ed.* **2008**, *47*, 10102-10105.

5. Gomberg, M. *J. Am. Chem. Soc.* **1900**, *22*, 757.

6. (a) Balch, A. L.; Holm, R. H. *J. Am. Chem. Soc.* **1966**, *88*, 5201; (b) Warren, L. F. *Inorg. Chem.* **1977**, *16*, 2814; (c) Chaudhuri, P.; Verani, C. N.; Bill, E.; Bothe, E.; Weyhermüller, T.; Wieghardt, K. *J. Am. Chem. Soc.* **2001**, *123*, 2213; (d) Anillo, A; . Diaz, M. R.; Garcia-Granda, S.; Obeso-Rosete, R.; Galindo, A.; Ienco, A.; Mealli, C. *Organometallics* **2004**, *23*, 471; (d) Bill, E.; Bothe, E.; Chaudhuri, P.; Chlopek, K.; Herebian, K.; Kokatam, S.; Ray, K.; Weyhermüller, T.; Neese, F.; Wieghardt, K. *Chem. Eur. J.* **2005**, *11*, 204; (e) Chlopek, K.; Bill, E.; Weyhermüller, T.; Wieghardt, K. *Inorg. Chem.* **2005**, *44*, 7087.

7. (a) Drüeke, S.; Chaudhuri, P.; Pohl, K.; Wieghardt, K; Ding, X.-Q.; Bill, E.; Sawaryn, A.; Trautwein, A. X.; Winkler, H.; Gurman, S. J. *Chem. Commun.* **1989**, 59. (b) Ding, X.-Q.; Bominaar, E. L.; Bill, E.; Winkler, H.; Trautwein, A. X.; Drüeke, S.; Chaudhuri, P.; Wieghardt, K. *J. Chem. Phys.* **1990**, *92*, 178. (c) Dutta, S. K.; Ensling, J.; Werner, R.; Flörke,

U.; Haase, W.; Gütlich, P.; Nag, K. *Angew. Chem., Int. Ed.* **1997**, *36*, 152. (d) LeCloux, D. D.; Davydov, R.; Lippard, S. J. *J. Am. Chem. Soc.* **1998**, *120*, 6810. (e) Lee, D.; Krebs, C.; Huynh, B. H.; Hendrich, M.; Lippard, S. J. *J. Am. Chem. Soc.* **2000**, *122*, 5000. (f) Hazra, S.; Sasmal, S.; Fleck, M.; Grandjean, F.; Sougrati, M. T.; Ghosh, M.; Harris, T. D.; Bonville, P.; Long, G. J.; Mohanta, S. *J. Chem. Phys.* **2011**, *134*, 174507.

8. Borrás-Almenar, J. J.; Clemente-Juan, J. M.; Coronado, E.; Tsukerblat, B. S. *J. Comput. Chem.* **2001**, *22*, 985.
9. SMART V 5.05 Software for the CCD Detector System; Bruker Analytical X-ray System, Inc.: Madison, WI, 1998.
10. SAINT. Data Reduction Software. V 6.36A; Bruker Analytical X-ray System, Inc.: Madison, WI, 2002.
11. SADABS. Bruker/Siemens Area Detector Absorption and Other Corrections. V2.03; Bruker Analytical X-ray System, Inc.: Madison, WI, 2002.
12. Sheldrick, G. M., *SHELXTL. V 6.12*; Bruker Analytical X-ray Systems, Inc.: Madison, WI, 2000.

Chapter 4: Metal Ion Lability in Polynuclear Complexes Featuring Strong M–M Interactions

4.1 Introduction

Polynuclear, heterometallic clusters are prevalent in biology.[1-3] Two prototypical enzymes that feature heteropolynuclear metallocofactors critical for function are the water oxidizing center in photosystem II[2] and the nitrogen fixing cofactors in nitrogenase.[1] In water oxidation, the presence of Ca within the Mn_4O_4Ca cofactor is critical for oxygen evolution, though the mechanistic role Ca plays is still a topic of debate.[4] The composition of the nitrogen-reducing cofactor has been observed to contain Fe alone[5] in a fused cubane structure with an iron-sulfur Fe_8S_9 core or with the substitution of a single Fe for Mo[1] or V[6] ion in the FeMo- and FeV-cofactors, respectively. The cofactor composition has been reported to have significant ramifications on the enzymatic chemoselectivity and catalytic efficacy.[7] Preparation of synthetic heteropolynuclear structures has been reported using non-selective, self-assembly processes,[8] and by addition of a second metal precursor to a stable metal unit, such as chelated metal units, metal-metal multiply bonded units, or incomplete cubane clusters.[9] Polynucleating ligands with different elemental binding affinities have been employed primarily in construction of heterobimetallics.[10] The selective exchange of transition metal ions from a polynuclear cluster could be a potential method for the preparation of heteropolynuclear cores in a systematic fashion, allowing for rigorous study of the electronic property perturbations. Herein we present the systematic substitution of cobalt ions for iron within a preformed polynuclear complex to afford heteropolynuclear complexes.

We have demonstrated the divergent oxidation pathways low-spin and high-spin iron-based clusters exhibit mediating redox processes. In the low-spin regime, core-delocalized redox behavior was observed where intra-core bonding is enhanced.[11] In contrast, the chemical oxidation of high-spin $(^{Ph}L)Fe_3(thf)_3$ leads to a trapped valency within a diiron unit, separate from the apparent site of halide capture.[12] Typically such ligand reorganization presents a large energy barrier, but the maximally high-spin formulation of the all-ferrous precursor[13] creates an inherently labile system. While we referenced the high-spin nature of the cluster to describe the facile ligand coordination mode changes, the notion of lability might be extended to include the facile exchange of metal ions out of the polynuclear core.

Scheme 4.1

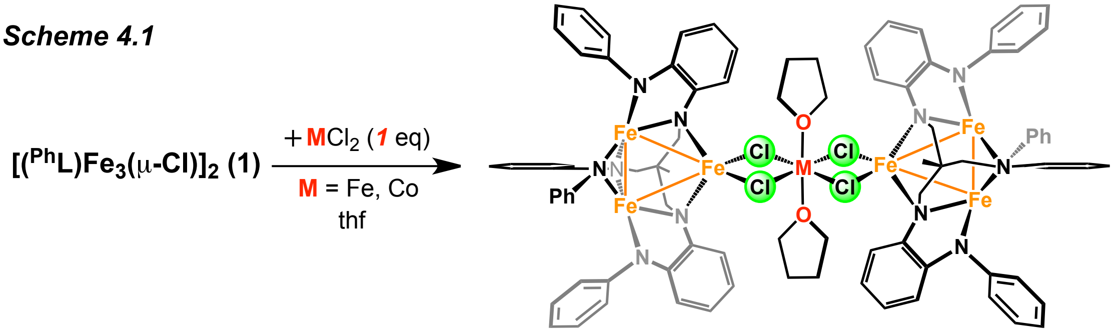

$(^{Ph}L)_2Fe_7Cl_4(thf)_2$ (**2**) 52%
$(^{Ph}L)_2Fe_6CoCl_4(thf)_2$ (**3**) 51%

4.2 Results and Discussion

In an effort to construct higher nuclearity clusters using the "$(^{Ph}L)Fe_3Cl$" synthon, the reactivity of $[(^{Ph}L)Fe_3(\mu\text{-}Cl)]_2$ (**1**)[12] was canvassed with metal-halide salts. Reaction of **1** with $FeCl_2$ or $CoCl_2$ in tetrahydrofuran afforded new complexes that could be crystallized from benzene yielding $(^{Ph}L)Fe_7(\mu\text{-}Cl)_4(thf)_2$ (**2**) and $(^{Ph}L)Fe_6Co(\mu\text{-}Cl)_4(thf)_2$ (**3**), respectively. The solid-state molecular structures for **2** and **3**, both featuring two trinuclear cores bridged by a

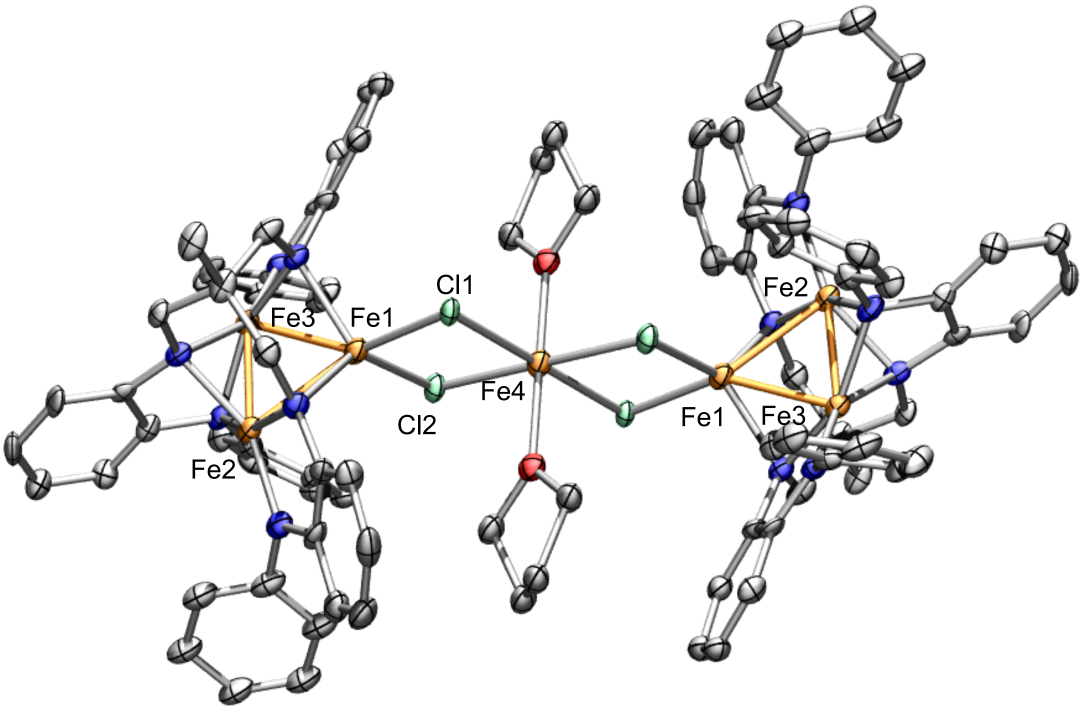

Figure 4.1. Solid-state structures for $(^{Ph}L)_2Fe_7(\mu\text{-}Cl)_4(thf)_2$ (**2**) with the thermal ellipsoids set at the 50% probability level (hydrogen atoms, and solvent molecules omitted for clarity; Fe orange, C gray, N blue, O red, Cl green). Bond lengths (Å): Fe1-Fe2, 2.5103(14); Fe1-Fe3, 2.6439(14); Fe2-Fe3, 2.3177(13); Fe1-Cl1, 2.3246(19); Fe1-Cl2, 2.403(2); Fe4-O1, 2.070(4); Fe4-Cl1, 2.5200(18); Fe4-Cl2, 2.5630(14).

single metal ion via four bridging halides (see Scheme 4.1 and Figure 4.1 for a representative molecular structure). Zero-field, ^{57}Fe Mössbauer analysis revealed four primary features: two quadrupole doublets for $[Fe_2]^{5+}$ (54% of the total Fe), the ferrous ion in the trinuclear subunit (Fe_A, 29%), and the bridge position ($FeCl_4(thf)_2$ (Fe_B); 17%), in nearly the expected ratio of 4:2:1 (see Figure 4.2, top). For complex **3**, three quadrupole doublets are present with the following metrical parameters (δ, $|\Delta|$ ($^{mm}/_{s}$)): 0.21, *2.69* (38.9%); 0.73, *1.39* (38.9%); and 1.16, *2.35* (22%), which coincide with spectral features for the $[Fe_2]^{5+}$, Fe_A, and Fe_B sites, respectively, in **2** (see Figure 4.2, bottom). If the Co ion occupied the bridge position $MCl_4(thf)_2$, we would anticipate the spectral features for the trinuclear subunits to be unchanged and no spectral features for the Fe_B site. However, the data are consistent with two iron ions in the trinuclear cores and an iron

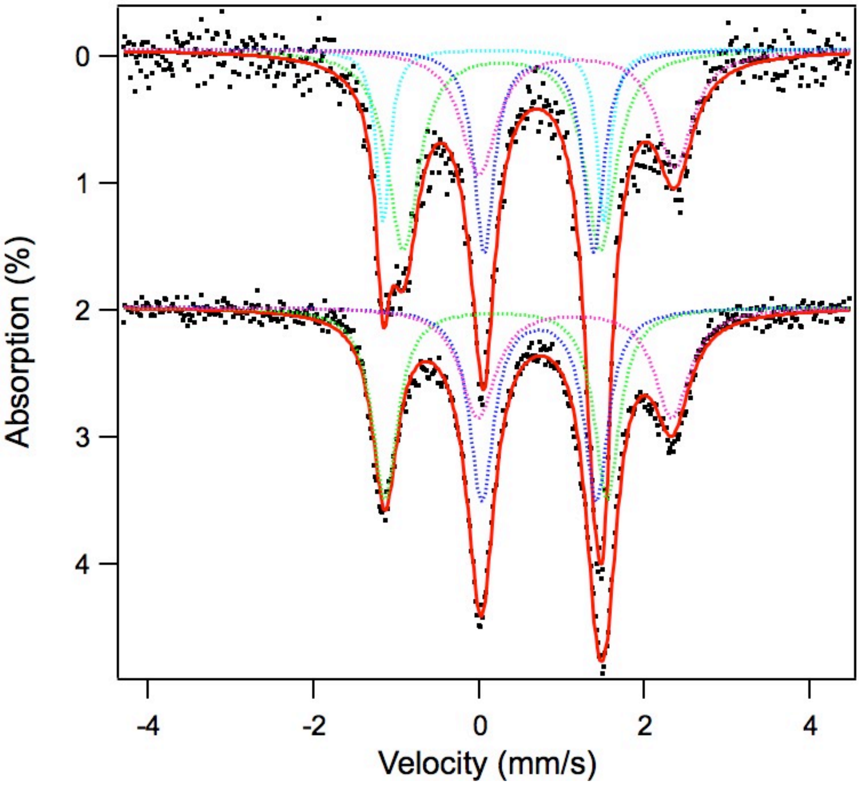

Figure 4.2. Zero-field ^{57}Fe Mössbauer spectrum obtained at 90 K for (top) (^{Ph}L)$_2$Fe$_7$(μ-Cl)$_4$(thf)$_2$ (**2**) and (bottom) (^{Ph}L)$_2$Fe$_6$Co(μ-Cl)$_4$(thf)$_2$ (**3**) with spectral fits (δ, $|\Delta E_Q|$ ($^{mm}/_{s}$)). For **2** (blue): 0.72, *1.32*, 29%; (green): 0.28, *2.38*, 29%; (cyan): 0.17, *2.67*, 25%; (magenta): 1.18, *2.37*, 17%. For **3** (blue): 0.73, *1.39*, 39%; (green): 0.21, *2.69*, 39%; (magenta): 1.16, *2.35*, 22%.

residing in the MCl$_4$(thf)$_2$ site, suggesting Co ion migration into the trinuclear subunits has occurred. This metal ion substitution is striking in that a minimum of four Fe–N bonds must be broken concomitant with four Co–N bonds created.

To explore this substitution reaction further, complex **1** was reacted with two or five equivalents of CoCl$_2$ in tetrahydrofuran for three hours at room temperature. Following removal of the volatiles *in vacuo*, acetonitrile was added to the solid. The material briefly dissolved and rapidly precipitated a fraction of the material as crystals. The crystallized material was collected on a fritted glass funnel and washed with acetonitrile. The product was recrystallized from a mixture of tetrahydrofuran and acetonitrile at room temperature. The reaction products obtained

Scheme 4.2

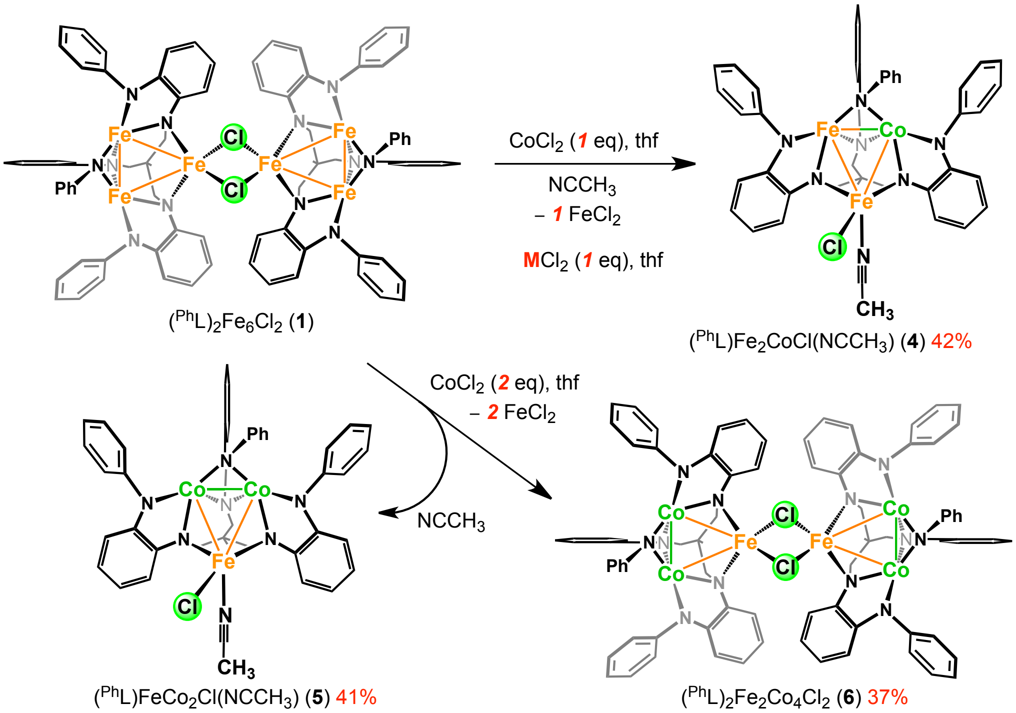

from these two reactions are consistent with the compositions of $(^{Ph}L)Fe_2CoCl(NCCH_3)$ (**4**) from the reaction of **1** with two equivalents of $CoCl_2$, and $(^{Ph}L)Co_2FeCl(NCCH_3)$ (**5**) from the reaction of **1** with five equivalents of $CoCl_2$ (see Scheme 4.2). Excess equivalents of Co ion are used in the latter case to ensure full substitution during the time scale of the reaction, while in the former no excess is used to prevent over-substitution to form **5**. Without the addition of extra acetonitrile during crystallization from benzene, the halide-bridged species was obtained $[(^{Ph}L)Co_2Fe(\mu\text{-}Cl)]_2$ (**6**) from the reaction with excess $CoCl_2$ (Figure 4.3b). Although the species feature paramagnetically shifted ^1H NMR, the spectra are diagnostic and distinguishable (see Figure 4.4). The spectra for the acetonitrile adducts **4** and **5** are distinct from each other, as well as $(^{Ph}L)Fe_3Cl(NCCH_3)$ (**7**), prepared by addition of acetonitrile to **1**, suggesting that **4** and **5** are distinct molecular species with integer Fe:Co ratios, rather than a mixture of substitution products. The evolution of $FeCl_2$ as an acetonitrile solvate was observed by analysis of the reaction supernatant

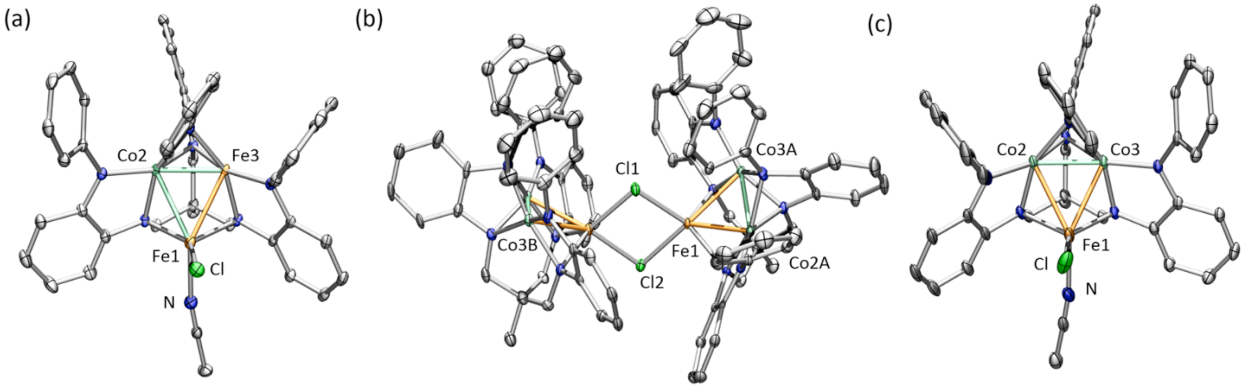

Figure 4.3. Solid-state structures for (a) $(^{Ph}L)Fe_2CoCl(NCCH_3)$ (**4**), (b) $[(^{Ph}L)FeCo_2(\mu\text{-}Cl)]_2$ (**6**), and (c) $(^{Ph}L)FeCo_2Cl(NCCH_3)$ (**5**) with the thermal ellipsoids set at the 50% probability level (hydrogen atoms, and solvent molecules omitted for clarity; Fe orange, Co aquamarine, C gray, N blue, O red, Cl green). Bond lengths (Å) for **4**: Fe1-M2, 2.5391(7); Fe1-M3, 2.5493(8); M2-M3, 2.2934(8); Fe1-Cl, 2.3393(9); Fe1-N_{ACN}, 2.134(3); for **6**: Fe1A-Co2A, 2.5120(14); Fe1A-Co3A, 2.5319(14); Co2A-Co3A, 2.2860(13); Fe1A-Cl1, 2.349(2), Fe1A-Cl2, 2.441(2); Fe1-Fe1, 3.4474(14); Fe1B-Co2B, 2.5009(14); Fe1B-Co3B, 2.5334(14); Co2B-Co3B, 2.2862(14); Fe1B-Cl1, 2.349(2), Fe1B-Cl2, 2.428(2); Fe1-Fe1, 3.4474(14); for **5**: Fe1-Co2, 2.5253(6); Fe1-Co3, 2.5348(6); Co2-Co3, 2.2971(5); Fe1-Cl, 2.2348(9); Fe1-N_{ACN}, 2.129(3).

by ^{57}Fe Mössbauer spectroscopy (δ, $|\Delta E_Q|$ ($^{mm}/_{s}$): 1.24, *2.16*), which matches the metrical parameters for $FeCl_2(NCCH_3)_2$ prepared independently.[14]

The molecular structures of the reaction products **4**-**6** were obtained by single crystal X-ray diffraction analysis (see Figure 4.3). For the acetonitrile-bound, trinuclear complexes **4** and **5**, the molecular structures are analogous to the previously described oxidized trinuclear complex $(^{Ph}L)Fe_3Cl(py)$,[12] maintaining the overall (^{Ph}L) coordination mode. The molecular structures feature two metal ions in an intermediate geometry between square planar and tetrahedral (Co2 and Fe3 in Figure 4.3a), and one metal ion in a trigonal, monopyramidal geometry (neglecting M–M interactions) bound by two ligand amide donors, a Cl ion, and the acetonitrile ligand (Fe1 in Figure 4.3a). As Fe and Co are indistinguishable by X-ray diffraction, the data for complex **4** were refined with an equal population of Co and Fe in the M2 and M3 positions, whereas the

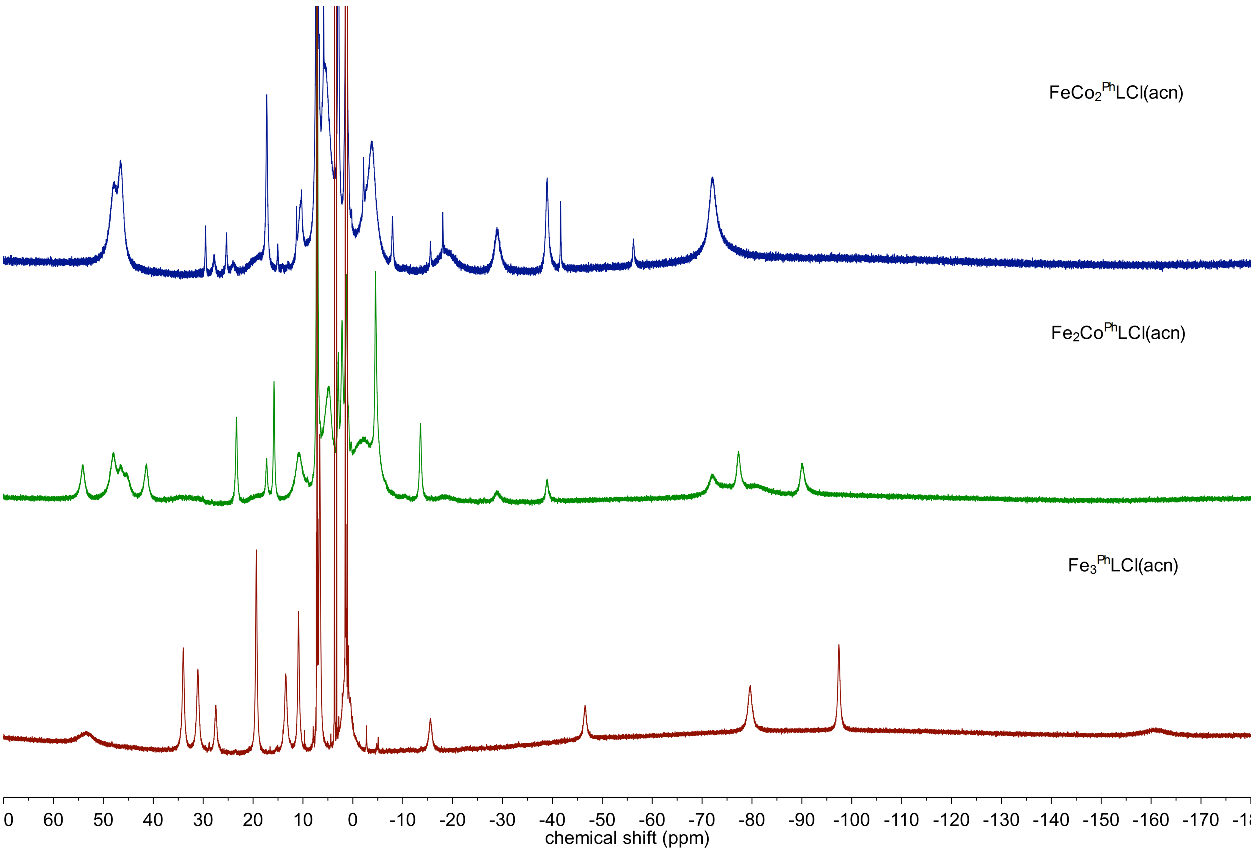

Figure 4.4. ^{1}H NMR data for (^{Ph}L)Fe$_2$CoCl(NCCH$_3$) (**4**) (green), (^{Ph}L)Co$_2$FeCl(NCCH$_3$) (**5**) (blue), and (^{Ph}L)Fe$_3$Cl(NCCH$_3$) (red).

data for **5** was refined with Co exclusively in the dinuclear unit. The four-coordinate ions (Co2, Fe3) are each bound to four ligand anilide units and feature a close M–M contact (2.2934(8) Å in **4**, 2.2971(5) Å in **5**) in the axial site. The two remaining M–M contacts between the dinuclear unit and the trigonal pyramidal site are shorter compared to the M–M separation observed in (^{Ph}L)Fe$_3$Cl(py) (data compiled in Table 4.1), though the solvent ligands are bound in different positions.[12] In (^{Ph}L)Fe$_3$Cl(py), the pyridine ligand completes the trigonal plane of Fe1, whereas this position is occupied by Cl in **4** and **5** which may contribute to some of the trinuclear core distortion observed. The chloride-bridged complex **6** maintains the connectivity present in its all-iron precursor **1**, providing the best comparison to illustrate the intra-core distortions resulting

Table 4.1. Selected bond distances.

	M1	M1–M2	M2	M1–M3	M3	M2–M3
1	Fe	2.5889(5)	Fe	2.5801(5)	Fe	2.3410(5)
6	$\mathrm{Fe_A}$	2.512(1)	$\mathrm{Co_A}$	2.532(1)	$\mathrm{Co_A}$	2.286(1)
	$\mathrm{Fe_B}$	2.501(1)	$\mathrm{Co_B}$	2.533(1)	$\mathrm{Co_B}$	2.286(1)
$\mathrm{Fe_3Cl}$[a]	Fe	2.7303(8)	Fe	2.6534(8)	Fe	2.2955(8)
4	Fe	2.5391(7)	M1	2.5493(8)	M2	2.2934(8)
5	Fe	2.5253(6)	Co	2.5348(6)	Co	2.2971(5)

(a) $(^{Ph}L)Fe_3Cl(py)$[12]

from substitution of iron by cobalt. All three M–M interactions are contracted for the mixed-metal cluster **6** as compared to the metrics found in the all-iron complex **1** (see Table 4.1). As with the tri-iron congeners, the bond metrics within the (^{Ph}L) ligand *o*-phenylenediamide units

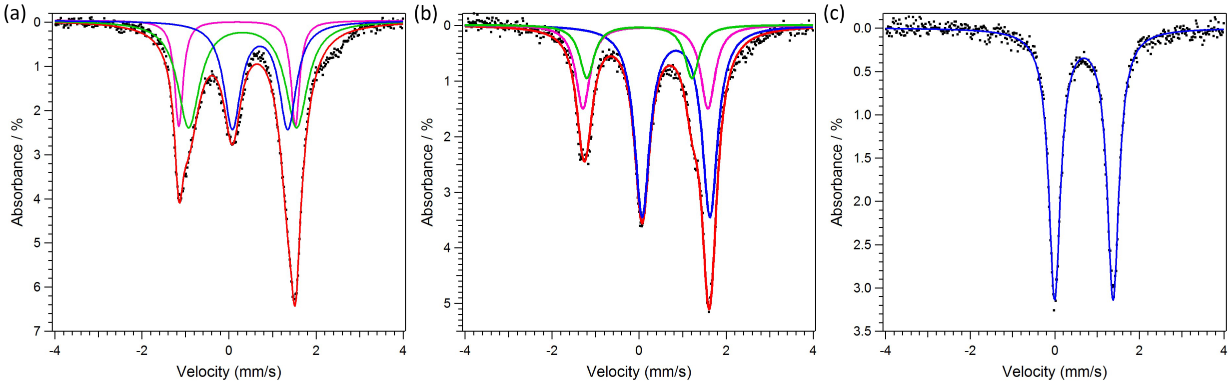

Figure 4.5. Zero-field ^{57}Fe Mössbauer spectrum obtained at 90 K and spectral fits (δ, $|\Delta E_Q|$ ($^{mm}/_{s}$)) for (a) $(^{Ph}L)Fe_3Cl(NCCH_3)$ (**7**), (component 1 (blue): 0.71, *1.27*, 33%; component 2 (green): 0.31, *2.48*, 33%; component 3 (magenta): 0.19, *2.68*, 33%); (b) $(^{Ph}L)Fe_2CoCl(NCCH_3)$ (**4**), (component 1 (blue): 0.83, *1.41*, 56.7%; component 2 (green): –0.01, *2.36*, 22.1%; component 3 (magenta): 0.21, *2.92*, 21.1%); (c) $(^{Ph}L)Fe_2CoCl(NCCH_3)$ (**6**) (0.69, *1.38*).

are consistent with the closed-shell dianion state (see Table 4.2-4.6), indicating ligand-redox participation is not involved.[15]

Table 4.2. Selected Ligand Bond Distances (Å) for **2**.

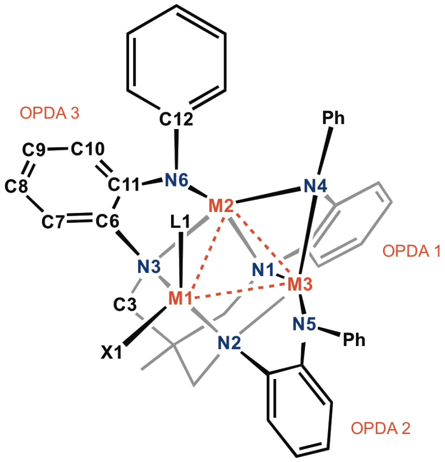

OPDA subunit	**1**	**2**	**3**
C(3)–N(1)	1.463(8)	1.464(8)	1.482(8)
N(1)–C(6)	1.415(8)	1.411(8)	1.430(8)
C(6)–C(7)	1.384(9)	1.373(9)	1.395(10)
C(7)–C(8)	1.397(10)	1.398(9)	1.410(10)
C(8)–C(9)	1.357(9)	1.368(10)	1.386(11)
C(9)–C(10)	1.408(9)	1.391(9)	1.395(11)
C(10)–C(11)	1.377(9)	1.398(9)	1.404(10)
C(6)–C(11)	1.407(9)	1.406(9)	1.403(10)
C(11)–N(4)	1.441(8)	1.380(8)	1.376(9)
N(4)–C(12)	1.419(8)	1.416(8)	1.446(10)

Table 4.3. Selected Ligand Bond Distances (Å) for **3**.

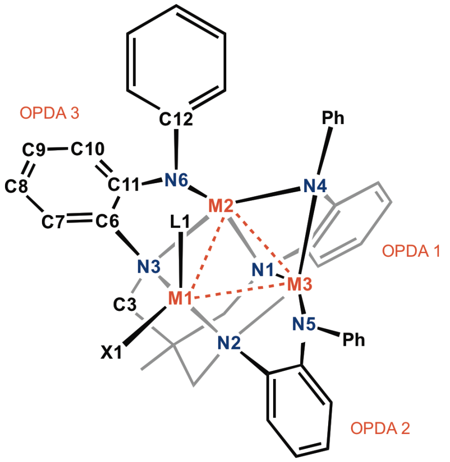

OPDA subunit	**1**	**2**	**3**
C(3)–N(1)	1.484(9)	1.477(9)	1.463(9)
N(1)–C(6)	1.425(9)	1.402(9)	1.399(9)
C(6)–C(7)	1.381(10)	1.382(10)	1.396(11)
C(7)–C(8)	1.391(11)	1.393(10)	1.388(11)
C(8)–C(9)	1.387(11)	1.379(11)	1.416(12)
C(9)–C(10)	1.385(10)	1.376(10)	1.387(12)
C(10)–C(11)	1.383(10)	1.396(10)	1.423(11)
C(6)–C(11)	1.437(10)	1.425(11)	1.386(11)
C(11)–N(4)	1.444(9)	1.370(9)	1.404(10)
N(4)–C(12)	1.442(9)	1.423(9)	1.428(11)

Table 4.4. Selected Ligand Bond Distances (Å) for **4**.

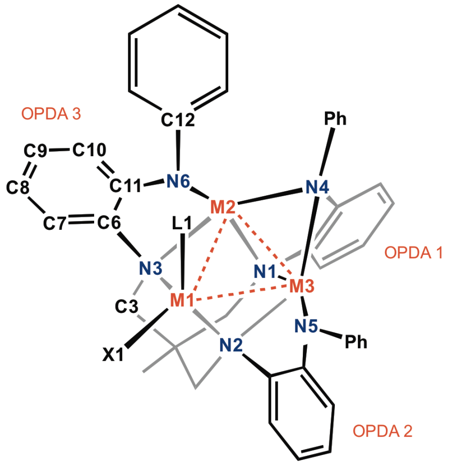

OPDA subunit	**1**	**2**	**3**
C(3)–N(1)	1.460(3)	1.492(3)	1.478(3)
N(1)–C(6)	1.423(4)	1.433(4)	1.415(4)
C(6)–C(7)	1.378(4)	1.385(4)	1.395(4)
C(7)–C(8)	1.398(4)	1.389(4)	1.382(4)
C(8)–C(9)	1.386(4)	1.395(4)	1.390(4)
C(9)–C(10)	1.391(4)	1.379(4)	1.388(4)
C(10)–C(11)	1.387(4)	1.408(4)	1.400(4)
C(6)–C(11)	1.414(4)	1.416(4)	1.412(4)
C(11)–N(4)	1.430(4)	1.385(4)	1.394(4)
N(4)–C(12)	1.436(3)	1.416(3)	1.433(4)

Table 4.5. Selected Ligand Bond Distances (Å) for **5**.

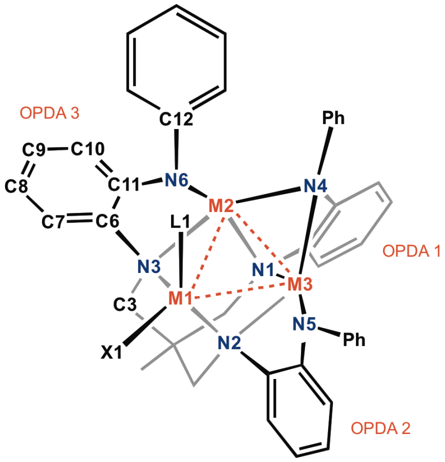

OPDA subunit	**1**	**2**	**3**
C(3)–N(1)	1.461(3)	1.490(3)	1.473(4)
N(1)–C(6)	1.422(3)	1.429(3)	1.418(3)
C(6)–C(7)	1.384(4)	1.382(4)	1.398(4)
C(7)–C(8)	1.387(4)	1.388(4)	1.385(4)
C(8)–C(9)	1.385(4)	1.393(4)	1.380(6)
C(9)–C(10)	1.400(4)	1.375(4)	1.396(5)
C(10)–C(11)	1.385(4)	1.408(4)	1.406(4)
C(6)–C(11)	1.408(4)	1.420(4)	1.406(5)
C(11)–N(4)	1.431(3)	1.384(4)	1.390(4)
N(4)–C(12)	1.434(3)	1.420(3)	1.433(4)

Table 4.6. Selected Ligand Bond Distances (Å) for **7**.

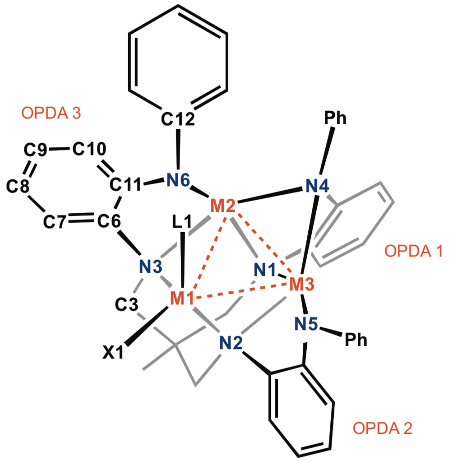

OPDA subunit	**1**	**2**	**3**
C(3)–N(1)	1.455(10)	1.468(10)	1.488(9)
N(1)–C(6)	1.422(10)	1.426(9)	1.425(9)
C(6)–C(7)	1.388(11)	1.396(10)	1.383(11)
C(7)–C(8)	1.411(12)	1.411(11)	1.398(11)
C(8)–C(9)	1.351(14)	1.387(13)	1.389(12)
C(9)–C(10)	1.403(12)	1.382(12)	1.379(11)
C(10)–C(11)	1.392(12)	1.416(10)	1.407(10)
C(6)–C(11)	1.396(12)	1.386(11)	1.400(10)
C(11)–N(4)	1.435(10)	1.387(9)	1.402(9)
N(4)–C(12)	1.410(10)	1.429(11)	1.426(9)

The zero-field, ^{57}Fe Mössbauer spectra for complexes **4**, **6**, and **7** obtained at 90 K are shown in Figures 4.5. Like **1** and the pyridine bound congener ($^{\text{Ph}}$L)Fe$_3$Cl(py), the spectrum of **7** (Figure 4.5a) features three distinct quadrupole doublets (δ, $|\Delta E_Q|$ ($^{\text{mm}}/_{\text{s}}$): component 1: 0.71, *1.27*, 33.3%; component 2: 0.31, *2.48*, 33.3%; component 3: 0.19, *2.68*, 33.3%). The two low-velocity doublets correspond to the iron ions within the oxidized dinuclear core $[Fe_2]^{5+}$, while the high velocity doublet describes the divalent pyramidal site. The spectrum for **4** (Figure 4.5b) shows little perturbation in the metrical parameters (δ, $|\Delta E_Q|$ ($^{mm}/_s$): component 1: 0.83, *1.41*, 56.7%; component 2: – 0.01, *2.36*, 22.1%; component 3: 0.21, *2.92*, 21.1%), except the ratio of high-velocity to low-velocity doublets has changed from almost 1:2 in 7 to 1.3:1 in **4**, signifying the Co substitution is occurring to a greater extent within the oxidized dinuclear unit ($[M_2]^{5+}$) than the divalent site. The spectrum for **6** (Figure 4.5c) shows complete substitution of both metal ions within the oxidized dinuclear subunit with only a single quadrupole doublet observed with metrical parameters consistent with the divalent site (δ, $|\Delta E_Q|$ ($^{mm}/_s$): 0.69, *1.38*). The

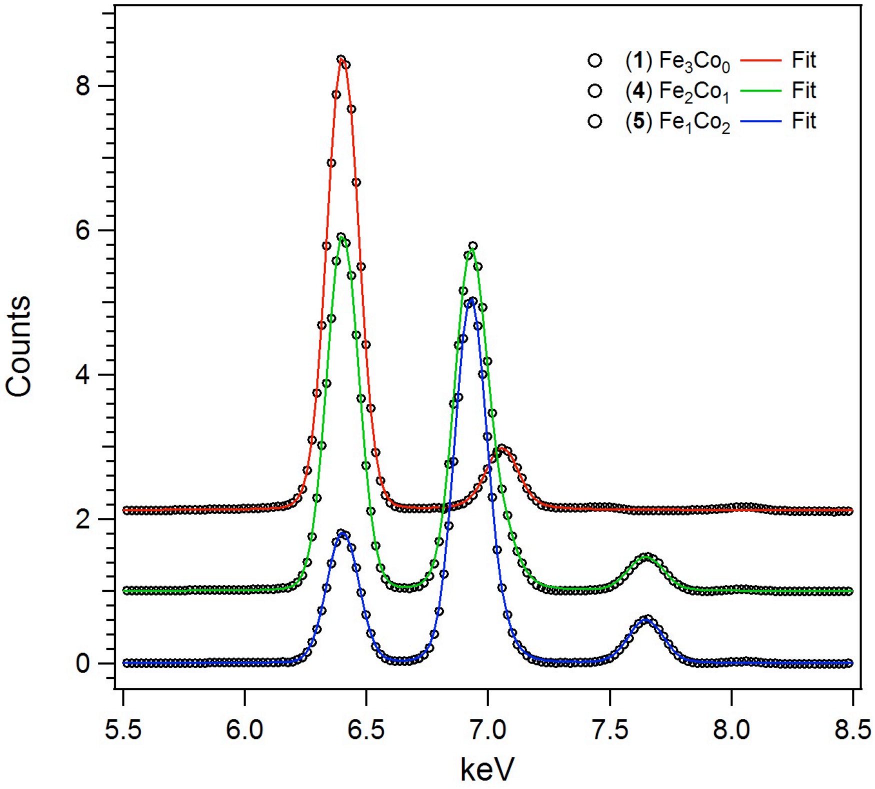

Figure 4.6. X-ray fluorescence spectra (data black circles, fits represented as lines): of **1** (red); **4** (green); **5** (blue).

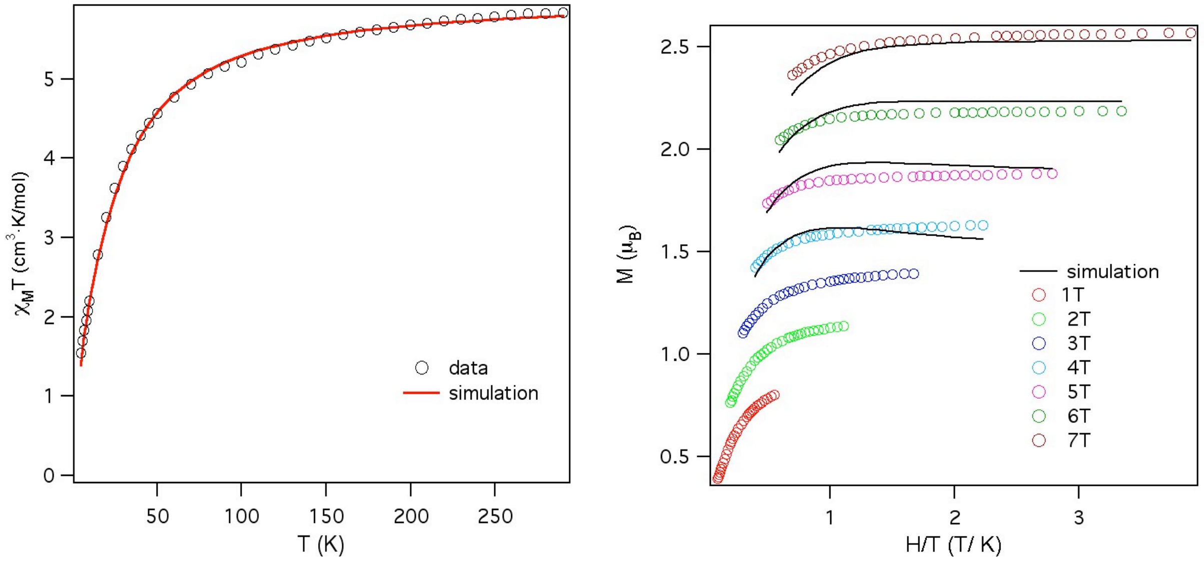

Figure 4.7. Variable-temperature magnetic susceptibility and reduced magnetization data for **4** with best simulation overall ($\boldsymbol{S}_1 = 2$, $\boldsymbol{S}_2 = 1$, $J = -4.25$ cm^{-1}, $D_1 = 5.25$ cm^{-1}, $D_2 = -20$ cm^{-1}, $g = 2.46$).

composition suggested by the Mössbauer analysis was corroborated by X-ray fluorescence analysis. The superposition of Fe and Co Kα and Kβ emission lines for complexes **3**, **4**, and **6** suggest Fe:Co ratios of 6:1, 2:1, and 1:2 (see Figure 4.6).

As previously reported, magnetic data acquired for the all-iron oxidation products revealed the oxidized diiron unit $[Fe_2]^{5+}$ is comprised of a strongly coupled $S = {}^3/_2$ unit that is weakly ferromagnetically coupled to the high spin ($S = 2$) ferrous site, giving an overall $S = {}^7/_2$ ground state for the trinuclear unit. The close M–M separation within the oxidized dimetal unit

Scheme 4.3

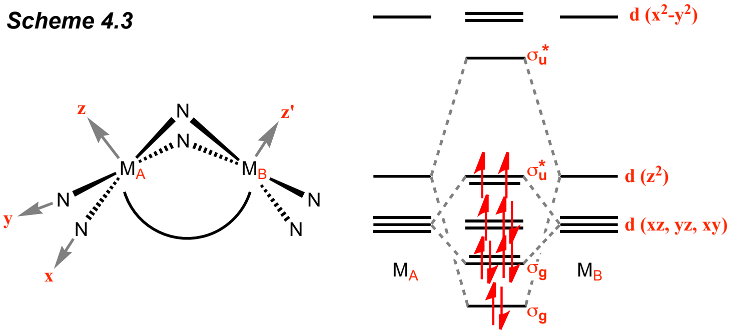

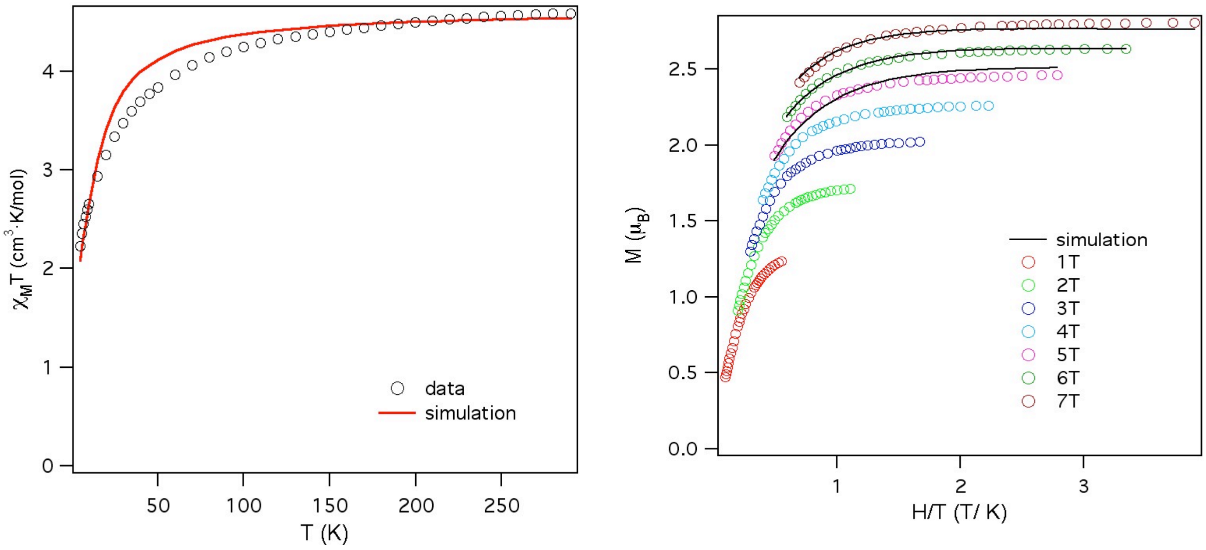

Figure 4.8. Variable-temperature magnetic susceptibility and reduced magnetization data for **5** with simulation parameters chosen to optimize reduced magnetization fit ($\boldsymbol{S}_1$ = 2, $\boldsymbol{S}_2$ =1/2, J = -4.0 cm^{-1}, D_1 = 4.25 cm^{-1}, g = 2.34).

$[M_2]^{5+}$ suggests significant M–M orbital overlap, dictated by the orbital overlap permitted for two edge-sharing square planar ions (Scheme 4.3).[12] For two Fe ions comprising the $[M_2]^{5+}$ unit, population of the eleven valence electrons into this manifold in a quartet configuration avoided population of $(M–N)_\sigma$* and $(M–M)_\sigma$* orbitals, providing a stabilizing interaction within the oxidized dinuclear unit. With complexes **3–6**, substitution of Co for Fe within the oxidized dinuclear unit does not structurally perturb the trinuclear core (*vide supra*) so as to suggest reconfiguration of these orbital interactions. Thus, for complex **4** which features a $[FeCo]^{5+}$ dinuclear subunit, we would anticipate a triplet formulation for $[M_2]^{5+}$, as the number of valence electrons in the orbital manifold has increased to 12. For complex **5** and **6**, we would anticipate a doublet configuration for the 13 electron $[Co_2]^{5+}$ subunit.

To probe the magnetic behavior of complexes **4-5** further, variable temperature dc susceptibility data were collected in the temperature range of 5-300 K (data are shown for complexes **4** and **5** in Figures 4.7 and 4.8). In the case of **4**, $\chi_M T$ decreases from a value of 5.78 cm^3 K mol^{-1} at 300 K to a minimum value of 1.55 cm^3 K mol^{-1} at 5 K (see Figure 4.7). Below 50 K, the data undergo a downturn, likely the result of Zeeman and zero-field splitting. In the case of **5**, $\chi_M T$ decreases from a value of 4.53 cm^3 K mol^{-1} at 300 K to a minimum value of 2.23 cm^3 K mol^{-1} at 5 K (see Figure 4.8). Variable temperature magnetization data were collected for complexes **4** and **5** in the temperature range of 1.8–10 K at fields of 1 to 7 T. Data are shown in Figures 4.7 and 4.8, which feature a series of non-superimposable isofield curves, with the 7 T curve reaching a maximum value of $M = 5.4$ μ_B at 1.8 K.

Given preservation of the ferrous unit in the divalent site of the trinuclear core following Co substitution, as suggested by the Mössbauer spectra, we modeled the data using the two-spin Hamiltonian shown below, where $\boldsymbol{S}_1 = 2$ for the ferrous ion, and $\boldsymbol{S}_2$ represents the mixed-valent dinuclear unit spin.

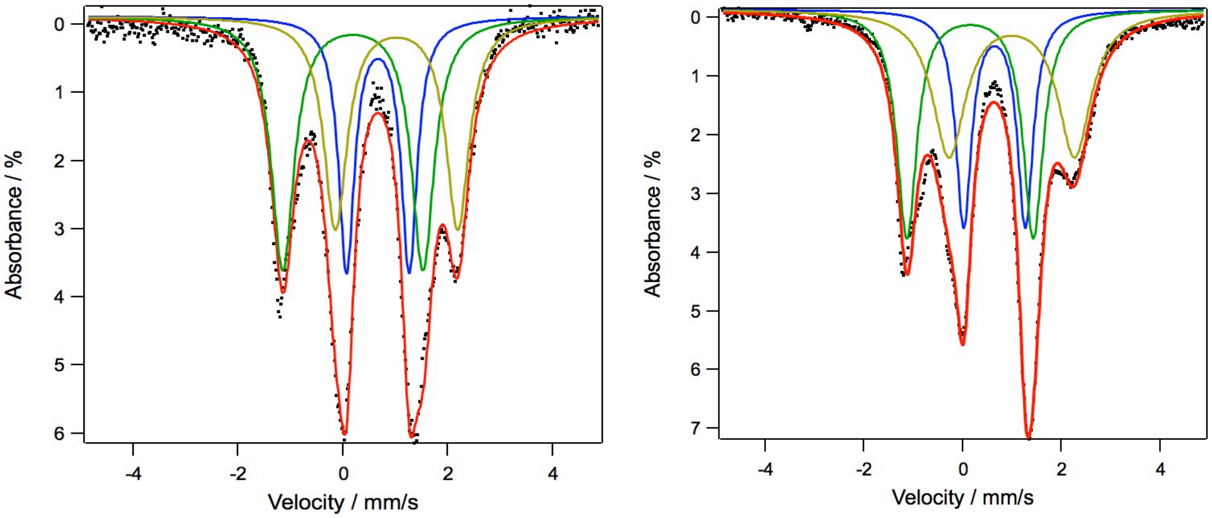

Figure 4.9. Zero-field ^{57}Fe Mössbauer spectrum of **2** prepared with ^{57}Fe-enriched FeCl$_2$(thf)$_2$, stirring for (left) 30 min and (right) 15 h. Left: (component 1 (blue): 0.67, *1.20*, 35%; component 2 (green): 0.19, *2.67*, 35%; component 3 (gold): 1.02, *2.33*, 30%). Right: (component 1 (blue): 0.64, *1.25*, 37%; component 2 (green): 0.15, *2.56*, 39%; component 3 (gold): 0.99, *2.54*, 25%).

$$\hat{H} = -2J(\boldsymbol{S}_1\boldsymbol{S}_2) + \Sigma D_i\boldsymbol{S}_i^2 + g\mu_B\boldsymbol{S}\cdot\boldsymbol{B} \qquad \text{Equation 4.1}$$

Following the orbital analysis presented above, the spin state of the oxidized dinuclear $[M_2]^{5+}$ unit $\boldsymbol{S}_2$ was modeled as a triplet for the $[FeCo]^{5+}$ unit in **4** and a doublet for the $[Co_2]^{5+}$ unit in **5**. The corresponding simulation using the program MAGPACK[16] that best reproduces the susceptibility and reduced magnetization data affords parameters of $J = -4.25$ cm^{-1}, $D_1 = 5.25$ cm^{-1}, $D_2 = -20$ cm^{-1}, and $g = 2.46$ for complex **4**; and $J = -6.25$ cm^{-1}, $D_1 = 2.5$ cm^{-1}, and $g = 2.35$ for complex **5.** Unlike the all-iron oxidized clusters, substitution of Co into the oxidized dinuclear unit leads to a weak antiferromagnetic coupling between the divalent ferrous site and the oxidized dinuclear unit.

With analysis for the thermodynamic product confirmed by a variety of spectroscopic techniques, we sought to probe how the metal substitution occurs kinetically. While many routes may be possible for the $CoCl_2$ salt to engage the $(^{Ph}L)Fe_3Cl(thf)$ core, we propose two such possibilities: (1) Formation of an extended core (similar to heptanuclear products **2** and **3**), followed by metathesis of the divalent ferrous ion for cobalt, then rearrangement of the core to position the Co ion within the oxidized dinuclear site. An alternative pathway could involve $CoCl_2$ association to the exposed axial face of either of the distorted square planar Fe ions within the oxidized dinuclear core and direct metathesis into that position. To probe these two possibilities complex **1** was reacted with ^{57}Fe-labeled $FeCl_2(thf)_2$ to produce heptanuclear **2** in tetrahydrofuran at room temperature. The reaction was evaporated to dryness and the ^{57}Fe Mossbauer spectra recorded after stirring times of 0.5, 2.5, and 15 h (see Figure 4.9). After 30 minutes reaction time, both the divalent site and oxidized dinuclear unit are equally enriched with ^{57}Fe, with that ratio remaining fairly constant even at 15 h. Thus for degenerative exchange of iron ions within **2**, each site is accessible, but accumulation in the oxidized $[Fe_2]^{5+}$ is not observed.

4.3 Conclusion

The foregoing analysis, based on crystallographic, magnetic, and Mössbauer spectral data, suggests metal ion metathesis from within polynuclear complexes is possible while maintaining the overall morphology of the cluster. Typically such ligand reorganization presents a large energy barrier, but the maximally high-spin formulation of the all-ferrous precursor creates an inherently labile system. Moreover, the $S = {}^3/_2$ $[Fe2]^{3+}$ unit in **1**, despite its apparently strong Fe-Fe interaction and lower spin, is also substitutionally labile. Furthermore, the elucidation of this unusual mode of cooperative redox reactivity demonstrates the potential of polynuclear model complexes to provide insight into the characteristic properties and assembly of clusters such as the polynuclear metallocofactors in nature.

4.4 Experimental Section

Materials and Methods. All manipulations involving metal complexes were carried out using standard Schlenk line or glove-box techniques under a dinitrogen atmosphere. All glassware was oven-dried for a minimum of 4 h and cooled in an evacuated antechamber prior to use in the dry box. Benzene, diethyl ether, acetonitrile (acn) and tetrahydrofuran (thf) were dried and deoxygenated on a Glass Contour System (SG Water USA, Nashua, NH) and stored over 4 Å molecular sieves (Strem) prior to use. Benzene-d_6, acn-d_3 and thf-d_8 were purchased from Cambridge Isotope Labs and were degassed and stored over 4 Å molecular sieves prior to use.

Solvents were typically tested with a standard purple solution of sodium benzophenone ketyl in thf in order to confirm effective oxygen and moisture removal. ^{57}Fe powder was purchased from Cambridge Isotope Labs and converted to ^{57}Fe-enriched $FeCl_2$ by conproportionation with $FeCl_3$. All other reagents were purchased from commercial vendors and used without further purification unless explicitly stated.

Physical Measurements. All of the measurements for the metal complexes except XRF analysis were made under anaerobic conditions. Elemental analyses were performed by Complete Analysis Laboratories, Inc., Parsippany, New Jersey. ^{1}H NMR spectra were recorded on a Varian Unity/Inova 500B NMR spectrometer with chemical shifts (δ ppm) referenced to residual NMR solvent. UV/Visible spectra were recorded on a Varian Cary 50 UV/Visible spectrometer using quartz cuvettes. NIR spectra were recorded on a PerkinElmer Lambda 750 high-performance UV-vis spectrometer.

XRF analyses were recorded on a Bruker Tracer III-SD XRF analyzer with the yellow filter (composition 12 mil Al and 1 mil Ti, passes 12-40 keV) and data were collected on each sample for at least 2 min. Samples for the calibration curve were prepared by grinding together cobalt(II)chloride hexahydrate and ferrous chloride tetrahydrate. The spectra of pure Fe and Co were each fit to two Voigt lineshapes. The calibration samples were then fit to four Voigt lineshapes, with the areas of each peak varying freely but all other parameters held to the reference values. Fits are substantially poorer if the Kα:Kβ peak area ratios are fixed, though the overall results are unchanged. Quantification was performed using only the Kα peak areas, but there is no difference in result if the Kα and Kβ areas are summed. Fe:Co ratios in samples were determined by fitting as for the calibration curve and calculating the Fe:Co ratio from the peak area ratios using the linear fit to the calibration curve.

Magnetic measurements were recorded using a Quantum Design MPMS-XL magnetometer. Powdered samples were placed in Lilly #4 gel capsules and thoroughly saturated with melted eicosane wax to prevent particle torquing in the magnetic field. Samples were suspended in the magnetometer in plastic straws. Samples were prepared under dinitrogen atmosphere. Dc magnetic susceptibility data were collected in the temperature range 5-300 K under fields of 0.1, 0.5, 1 and 2 T. Magnetization data were acquired at 1.8-10 K under fields of 1, 2, 3, 4, 5, 6, and 7 T. Susceptibility data were corrected for the diamagnetic contribution of a blank sample consisting of the wax, capsule and straw at the correct field and temperature. The magnetic susceptibilities were adjusted for diamagnetic contributions using the constitutive corrections from Pascal's constants. The molar magnetic susceptibility (χ_m) was calculated by converting the magnetization (M) obtained from the magnetometer to a molar susceptibility using the multiplication factor [molecular weight (MW)]/[sample weight (m) × field strength (H)]. All samples were checked for ferromagnetic impurities by collecting a field dependence curve at 100 K and samples were rejected if any deviation from linearity was observed.

Iron-57 Mössbauer spectra were measured on a constant acceleration spectrometer (SEE Co, Minneapolis, MN) with a Janis SVT-100 cryostat. Isomer shifts are quoted relative to α-Fe foil (< 25 μm thick) at room temperature. Samples were prepared using approximately 30 mg of sample suspended in paratone-N oil. Temperatures were controlled using a LakeShore 321 Autotuning temperature controller. Temperature swings were no greater than ±10 K, and were generally within ±2 K. Data were analyzed using an in-house package written by E. R. King and modified by E. V. Eames in Igor Pro (Wavemetrics).

Preparation of [(^{Ph}L)Fe_3Cl]$_2$$FeCl_2(thf)_2$ (2). A chilled (–35 °C) solution of **1** (100 mg, 61.3 μmol, 1 equiv) in thf (15 ml) was added to solid $FeCl_2$ (8 mg, 63.5 μmol, 1.04 equiv) and stirred for 3 h. The solvent was removed under vacuum. Benzene (5 ml) was added with three drops of thf and the solution was filtered and stored at room temperature. The resulting precipitate was washed with ether and dried under vacuum. Yield: 60 mg (52%). X-ray quality crystals were grown from a concentrated filtered solution in benzene at room temperature. Anal. Calcd for $C_{90}H_{88}Fe_7N_{12}Cl_4O_2$: C 56.82, H 4.66, N 8.83. Found: C 56.57, H 4.61, N 8.71.

Preparation of (^{Ph}L)$_2$$Fe_6CoCl_4(thf)_2$ (3). A chilled (–35 °C) solution of **1** (60 mg, 37 μmol, 1 equiv) in thf (15 ml) was added to solid $CoCl_2$ (4.8 mg, 37 μmol, 1 equiv) and stirred for 3 h. The solvent was removed under vacuum. Benzene (5 ml) was added with three drops of thf and the solution was filtered and stored at room temperature. The resulting precipitate was washed with benzene and dried under vacuum. Yield: 35 mg (51%). X-ray quality crystals were grown from a concentrated filtered solution in benzene at room temperature. Anal. Calcd for $C_{90}H_{88}Fe_6CoN_{12}Cl_4O_2$: C 56.73, H 4.65, N 8.82. Found: C 56.69, H 4.58, N 8.75.

Preparation of (^{Ph}L)Fe_2CoCl(acn) (4). A thawing solution of **1** (130 mg, 80 μmol, 1 equiv) in thf (20 ml) was added to solid $CoCl_2$ (21.2 mg, 164 μmol, 2.06 equiv) and stirred for 3 h. The solvent was removed under vacuum. Acetonitrile (2 ml) was added, briefly dissolving the solid and rapidly crystallizing out the product. The crystals were washed with acetonitrile (3 ml), then dissolved in benzene and filtered to remove any insoluble material. The benzene was removed under vacuum, and 4 drops of thf were added, followed by acetonitrile (2 ml). The product, which is insoluble in acetonitrile, was collected on a frit and washed with more acetonitrile, then dried under vacuum. Recrystallized yield: 58 mg (42%). X-ray quality crystals were grown from a concentrated filtered solution in acetonitrile at room temperature. ^{1}H NMR (C_6D_6 with 3 drops $NCCH_3$-*d*$_3$, 500 MHz, δ, ppm): 54, 48, 46, 45, 41, 23, 17, 16, 11, 5, 2, -2, -5, -14, -29, -39, -72, -77, -90. Anal. Calcd for $C_{43}H_{39}Fe_2CoN_7Cl$: C 60.06, H 4.57, N 11.40. Found: C 59.96, H 4.59, N 11.42.

Preparation of (^{Ph}L)FeCo$_2$Cl(acn) (5). A thawing solution of **1** (140 mg, 86 μmol, 1 equiv) in thf (20 ml) was added to solid $CoCl_2$ (57.1 mg, 443 μmol, 5.1 equiv) and stirred for 3 h. The solvent was removed under vacuum. Acetonitrile (2 ml) was added, briefly dissolving the solid and rapidly crystallizing out the product. The crystals were washed with acetonitrile (3 ml), then dissolved in benzene and filtered to remove any insoluble material. The benzene was removed under vacuum, and 4 drops of thf were added, followed by acetonitrile (2 ml). The product, which is insoluble in acetonitrile, was collected on a frit and washed with more acetonitrile, then dried under vacuum. Recrystallized yield: 60.3 mg (41%). X-ray quality crystals were grown from a concentrated filtered solution in acetonitrile at room temperature. ^{1}H NMR (C_6D_6 with 3 drops $NCCH_3$-*d*$_3$, 500 MHz, δ, ppm): 48, 46, 30, 28, 26, 24, 17, 15, 11, 10, 5.5, -2, -4, -8, -16, -19, -29, -39, -42, -56, -72. Anal. Calcd for $C_{43}H_{39}FeCo_2N_7Cl$: C 59.85, H 4.55, N 11.36. Found: C 59.75, H 4.66, N 11.28.

Preparation of (^{Ph}L)Fe$_3$Cl(acn) (7). To a solution of **1** (50 mg, 31 μmol) in benzene (5 ml) was added 25 drops of acetonitrile. The solution was filtered and the solvent removed under vacuum. The ^{1}H NMR sample was prepared by addition of deuterated solvents to **1**, followed by filtration. No crystals of this material were ever obtained, despite effort. Yield: 51 mg (97%). ^{1}H

NMR (C_6D_6 with 3 drops $NCCH_3$-*d₃*, 500 MHz, δ, ppm): 53, 36, 33, 28, 19, 13.5, 12, 6, -16, -47, -80, -98. Anal. Calcd for $C_{43}H_{39}Fe_3N_7Cl$: C 60.28, H 4.59, N 11.44. Found: C 60.26, H 4.54, N 11.42.

Preparation of $[(^{Ph}L)FeCo_2Cl]_2$ (6). A thawing solution of **1** (140 mg, 86 μmol, 1 equiv) in thf (20 ml) was added to solid $CoCl_2$ (57.1 mg, 443 μmol, 5.1 equiv) and stirred for 5 h. The solvent was removed under vacuum. Acetonitrile (2 ml) was added, briefly dissolving the solid and rapidly crystallizing out **6**. The crystals were washed with acetonitrile (3 ml), then dissolved in benzene and filtered to remove any insoluble material. The solvent was removed under vacuum, more benzene (5 ml) was added and the solution stored overnight. The product crystallized, and was collected on a frit and washed with more benzene, then dried under vacuum. Recrystallized yield: 52 mg (37%). X-ray quality crystals were grown from a concentrated filtered solution in benzene at room temperature. Anal. Calcd for $C_{41}H_{36}FeCo_2N_6Cl$: C 59.91, H 4.41, N 10.22. Found: C 59.94, H 4.47, N 10.08.

^{57}Fe Exchange Experiments. Degenerative exchange of ^{57}Fe-enriched $FeCl_2thf_2$ was observed by Mössbauer spectroscopy. Enriched $FeCl_2thf_2$ (2.5 mg, 0.5 equiv) was dissolved in THF (2 ml) with stirring, chilled, and added to **1** (30 mg, 1 equiv) dissolved in 5 ml thf and frozen. This procedure was repeated three times, and the resulting solution was filtered and dried (with stirring) under vacuum after 0, 2 and 15 h. Mössbauer samples were prepared from the remaining solid (~15 mg).

X-ray Structure Determinations. A single crystal suitable for X-ray analysis was mounted and centered on the tip of a cryoloop attached to a goniometer head. Cell parameters were determined using the program SMART.[17] Data reduction and integration were performed with the software package SAINT,[18] while absorption corrections were applied using the program SADABS.[19] Space groups were assigned unambiguously by analysis of symmetry, and systematic absences were determined by XPREP. The positions of the heavy atoms were found via direct methods using the program SHELXTL.[20] Subsequent cycles of least-squares refinement followed by difference Fourier syntheses revealed the positions of the remaining non-hydrogen atoms. Hydrogen atoms were added in idealized positions. Non-hydrogen atoms were refined with anisotropic displacement parameters. In disordered structures, phenyl rings were constrained to idealized geometries and anisotropic displacement parameters were restrained as necessary. Crystallographic data are given in Tables 4.7 and selected bond distances and angles in Table 4.8.

Modeling of Magnetic Data. The susceptibility and reduced magnetization data were modeled using the package MAGPACK.[16] Simulations were run by canvassing a range of parameter values rather than using a fitting algorithm, due to the computational intensity of the calculations. The spin state values reported are the only ones that produced plausible fits, but the exchange, anisotropy and g parameters reported should not be taken as definitive, as wide ranges of values gave fits of similar quality. (Anisotropy parameters are not in general reliably determined by fitting magnetic data.) In some cases several plots are shown to demonstrate this (see Figures S20-22). As described in the text each trinuclear unit was modeled as a high-spin ferrous unit coupled to the M_2^{5+} pair ($S = 1$, $FeCo^{5+}$; $S = 1/2$, Co_2^{5+}). Where possible, parameter values were chosen to simultaneously optimize the fit to the reduced magnetization and susceptibility data, but no attempt was made to optimize the combined fit in a rigorously quantitative way.

Table 4.7. X-ray Crystallographic Data for **2-6**.

Chemical formula	$C_{90}H_{88}Fe_7N_{12}Cl_4O_2 \cdot 1.25\,(C_6H_6)$	$C_{90}H_{88}Fe_6CoN_{12}Cl_4O_2 \cdot 1.25\,(C_6H_6)$	$C_{43}H_{39}Fe_2CoN_7 \cdot 1.5\,(C_2H_3N)$	$C_{43}H_{39}FeCo_2N_7 \cdot 1.5\,(C_2H_3N)$	$C_{82}H_{72}Fe_2Co_4N_{12}Cl_2 \cdot 9.5\,(C_6H_6)$
FW	2171.95	2175.03	1842.95	1849.11	2385.86
Space group	$P\bar{1}$	$P\bar{1}$	$P\bar{1}$	$P\bar{1}$	$P\bar{1}$
a (Å)	12.761(3)	12.761(3)	12.7540(12)	11.1826(10)	18.0835(10)
b (Å)	13.232(3)	13.232(3)	18.1556(16)	11.8436(11)	19.0729(10)
c (Å)	15.826(4)	15.826(4)	19.2333(17)	17.5880(16)	19.3294(10)
α (deg)	79.669(5)	79.669(5)	72.2376(14)	73.4180(10)	74.2878(9)
β (deg)	74.646(5)	74.646(5)	86.4885(14)	82.2320(10)	67.1492(9)
γ (deg)	79.387(5)	79.387(5)	76.0497(14)	67.0980(10)	80.5020(9)
V (Å^3)	2508.9(10)	2508.9(10)	4115.8(6)	2055.8(3)	5900.6(5)
Z	1	1	2	1	2
d_{calcd} (g·cm^{-3})	1.438	1.440	1.487	1.494	1.343
μ (mm^{-1})	1.147	1.168	1.204	1.256	0.891
T (K)	100(2)	100(2)	100(2)	100(2)	100(2)
R1[a] (wR2[b])	0.0698 (0.1983)	0.0709 (0.1588)	0.0413 (0.1007)	0.0411(0.0948)	0.1010 (0.2914)

[a] $R1 = [\sum w(F_o - F_c)^2 / \sum wF_o^2]^{1/2}$.

[b] $wR2 = [\sum [w(F_o^2 - F_c^2)^2] / \sum w(F_o^2)^2]^{1/2}$, $w = 1/[\sigma^2(F_o^2) + (aP)^2 + bP]$, where $P = [\max(F_o^2,0) + 2(F_c^2)]/3$.

Table 4.8. Selected Core Bond Distances (Å) of **1**-**6**.

	1	**2**	**3**	**4**	**5**	**6**
M(1)–M(2)	2.5889(5)	2.5103(14)	2.5068(17)	2.5427(6) 2.5342(6)	2.5253(6)	2.5101(13)
M(1)–M(3)	2.5801(5)	2.6439(14)	2.5754 (17)	2.5530(6) 2.5221(6)	2.5348(6)	2.5294(14)
M(2)–M(3)	2.3410(5)	2.3177(13)	2.2903(16)	2.2948(6) 2.3013(6)	2.2971(5)	2.2842(13)
M(1)–X	2.3573(6)	2.3246(19)	2.334(2)	2.2413(9) 2.2378(9)	2.2348(9)	2.346(2)
M(1)–L	2.4425(6)	2.403(2)	2.413(2)	2.137(3) 2.125(3)	2.129(3)	2.438(2)
M(1)–N(2)	2.081(2)	2.107(5)	2.069(6)	2.066(2) 2.091(2)	2.068(2)	2.071(6)
M(1)–N(3)	2.092(2)	2.121(5)	2.133(6)	2.085(2) 2.072(2)	2.088(2)	2.084(6)
M(2)–N(1)	1.923(2)	1.979(5)	1.940(6)	1.927(2) 1.948(2)	1.925(2)	1.934(6)
M(2)–N(3)	1.9266(19)	1.912(6)	1.945(7)	1.919(2) 1.913(2)	1.919(2)	1.913(6)
M(2)–N(4)	1.978(2)	2.069(6)	2.029(7)	2.003(2) 2.034(2)	2.001(2)	2.024(6)
M(2)–N(6)	1.8552(19)	1.886(5)	1.843(6)	1.853(2) 1.869(2)	1.855(2)	1.846(6)
M(3)–N(1)	1.965(2)	1.918(5)	1.907(6)	1.955(2) 1.924(2)	1.950(2)	1.901(6)
M(3)–N(2)	1.916(2)	1.932(5)	1.925(6)	1.914(2) 1.926(2)	1.910(2)	1.934(6)
M(3)–N(4)	2.059(2)	1.977(5)	1.979(7)	2.027(2) 2.006(2)	2.025(2)	2.011(6)
M(3)–N(5)	1.872(2)	1.847(5)	1.835(6)	1.861(2) 1.854(2)	1.865(2)	1.840(6)

References Cited

1. Nitrogenase: (a) Howard, J. B.; Rees, D. C. *Chem. Rev.* **1996**, *96*, 2965. (b) Burgess, B. K.; Lowe, D. J. *Chem. Rev.* **1996**, *96*, 2983. (c) Dos Santos, P. C; Igarashi, R. Y.; Lee, H.-I.; Hoffman, B. M.; Seefeldt, L. C.; Dean, D. R. *Acc. Chem. Res.* **2005**, *38*, 208. (d) Hoffman, B. M; Dean, D. R.; Seefeldt, L. C. *Acc. Chem. Res.* **2009**, *42*, 609.

2. Photosystem II: (d) Nugent, J., Ed. *Biochim. Biophys. Acta* **2001**, *1503*, 1. (e) Ferreira, K. N.; Iverson, T. M.; Maghlaoui, K.; Barber, J.; Iwata, S. *Science* **2004**, *303*, 1831. (f) Iwata, S.; Barber, J. *Curr. Opin. Struct. Biol.* **2004**, *14*, 447.

3. Mn/Fe Ribonucleotide reductase: (a) Jiang, W.; Yun, D.; Saleh, L.; Barr, E. W.; Xing, G.; Hoffart, L. M.; Maslak, M.-A.; Krebs, C.; Bollinger, J. M., Jr. *Science* **2007**, *316*, 1188. (b) Jiang, W.; Hoffart, L. M.; Krebs, C.; Bollinger, J. M., Jr. *Biochemistry* **2007**, *46*, 8709.

4. (a) Ghanotakis, D. F.; Babcock, G. T.; Yocum, C. F. *FEBS* **1984**, *167*, 127. (b) Krieger, A.; Weis, E. *Photosynthesis Res.* **1993**, *37*, 117. (c) Renger, C. *Biochim. Biophys. Acta* **2001**, *1503*, 210. (d) McEvoy, J. P.; Brudvig, G. W. *Chem. Rev.* **2006**, *106*, 4455. (e) Siegbahn, P. E. M. *Inorg. Chem.* **2008**, *47*, 1779.

5. (a) Joerger, R. D.; Jacobson, M. R.; Premakumar, R.; Wolfinger, E. D.; Bishop, P. E. *J. Bacteriol.* **1989**, *171*, 1075. (b) Schüdderkopf, K.; Hennecke, S.; Liese, U.; Kutsch, M.; Klipp, W. *Mol. Microbiol.* **1993**, *8*, 673. (c) Zinoni, F.; Robson, R. M.; Robson, R. L. *Biochim. Biophys. Acta.* **1993**, *1174*, 83.

6. (a) Joerger, R. D.; Loveless, T. M.; Pau, R. N.; Mitchenall, L. A.; Simon, B. H.; Bishop, P. E. *J. Bacteriol.* **1990**, *172*, 3400. (b) Robson, R. L.; Woodley, P. R.; Pau, R. N.; Eady, R. R. *EMBO J.* **1989**, *8*, 1217. (c) Theil, T. **1993**, *175*, 6276.

7. (a) Lee, C. C.; Hu, Y.; Ribbe, M. W. *Science* **2010**, *329*, 642. (b) Hu, Y.; Lee, C. C.; Ribbe, M. W. *Dalton Trans.*, **2012**, *41*, 1118.

8. (a) Tulsky, E. G.; Long, J. R. *Inorg. Chem.* **2001**, *40*, 6990. (b) Caulton, K. G.; Hubert-Pfalzgraf, L. G. *Chem. Rev.* **1990**, *90*, 969. (c) Sappa, E.; Tiripicchio, A.; Braunstein, P. *Chem. Rev.* **1983**, *83*, 203.

9. (a) Rao, P. V.; Holm, R. H. *Chem. Rev.* **2004**, *104*, 527. (b) Lee, S. C.; Holm. R. H. *Chem. Rev.* **2004**, *104*, 1135. (c) Kanady, J. S.; Tsui, E. Y.; Day, M. W.; Agapie, T. *Science* **2011**, *333*, 733. (d) Hernandez-Molina, R.; Sokolov, M. N.; Sykes, A. G. *Acc. Chem. Res.* **2001**, *34*, 223. (e) Clérac, R.; Cotton, F. A.; Dunbar, K. R.; Murillo, C. A.; Wang, X. *Inorg. Chem.* **2001**, *40*, 420. (f) Nippe, M.; Berry, J. F. *J. Am. Chem. Soc.* **2007**, *129*, 12684. (g) Nippe, M.; Victor, E.; Berry, J. F. *Eur. J. Inorg. Chem.* **2008**, 5569.

10. (a) Greenwood, B. P.; Forman, S. I.; Rowe, G. T.; Chen, C.-H.; Foxman, B. M.; Thomas, C. M. *Inorg. Chem.* **2009**, *48*, 6251. (b) Slaughter, L. M.; Wolczanski, P. T. *Chem. Commun.*

1997, 2109. (c) Glaser, T.; Kesting, F.; Beissel, T.; Bill, E.; Weyhermüller, T.; Meyer-Klaucke, W.; Wieghardt, K. *Inorg. Chem.* **1999**, *38*, 722. (d) Beissel, T.; Birkelbach, F.; Bill, E.; Glaser, T.; Kesting, F.; Krebs, C.; Weyhermüller, T.; Wieghardt, K.; Butzlaff, C.; Trautwein, A. X. *J. Am. Chem. Soc.* **1996**, *118*, 12376. (e) Akine, S.; Taniguchi, T.; Nabeshima, T. *Inorg. Chem.* **2008**, *47*, 3255.

11. (a) Zhao, Q.; Betley, T. A. *Angew. Chem. Int. Ed.*, **2011**, *50*, 709. (b) (c) Zhao, Q.; Harris, T. D.; Betley, T. A. *J. Am. Chem. Soc.* **2011**, *133*, 8293. (d) Harris, T. D.; Zhao, Q.; Hernández Sánchez, R.; Betley, T. A. *Chem. Commun.* **2011**, *47*, 6344.
12. Eames, E. V.; Betley, T. A. *Submitted*.
13. Eames, E. V.; Harris, T. D.; Betley, T. A. *Chem. Sci.* **2012**, *3*, 407.
14. Pokhodnya, K. I.; Bonner, M.; DiPasquale, A. G.; Rheingold, A. L.; Her, J.-H.; Stephens, P. W.; Park, J.-W.; Kennon, B. S.; Arif; A. M.; Miller, J. S. *Inorg. Chem.* **2007**, *46*, 2471.
15. (a) Balch, A. L.; Holm, R. H. *J. Am. Chem. Soc.* **1966**, *88*, 5201; (b) Warren, L. F. *Inorg. Chem.* **1977**, *16*, 2814; (c) Chaudhuri, P.; Verani, C. N.; Bill, E.; Bothe, E.; Weyhermüller, T.; Wieghardt, K. *J. Am. Chem. Soc.* **2001**, *123*, 2213; (d) Anillo, A; Diaz, M. R.; Garcia-Granda, S.; Obeso-Rosete, R.; Galindo, A.; Ienco, A.; Mealli, C. *Organometallics* **2004**, *23*, 471; (d) Bill, E.; Bothe, E.; Chaudhuri, P.; Chlopek, K.; Herebian, K.; Kokatam, S.; Ray, K.; Weyhermüller, T.; Neese, F.; Wieghardt, K. *Chem. Eur. J.* **2005**, *11*, 204; (e) Chlopek, K.; Bill, E.; Weyhermüller, T.; Wieghardt, K. *Inorg. Chem.* **2005**, *44*, 7087.
16. Borrás-Almenar, J. J.; Clemente-Juan, J. M.; Coronado, E.; Tsukerblat, B. S. *J. Comput. Chem.* **2001**, *22*, 985.
17. SMART V 5.05 Software for the CCD Detector System; Bruker Analytical X-ray System, Inc.: Madison, WI, 1998.
18. SAINT. Data Reduction Software. V 6.36A; Bruker Analytical X-ray System, Inc.: Madison, WI, 2002.
19. SADABS. Bruker/Siemens Area Detector Absorption and Other Corrections. V2.03; Bruker Analytical X-ray System, Inc.: Madison, WI, 2002.
20. Sheldrick, G. M., *SHELXTL. V 6.12*; Bruker Analytical X-ray Systems, Inc.: Madison, WI, 2000.

Appendix A: Supplementary Figures for Chapter 2

Figure A1. UV-vis spectra of $(^{Ph}L)Fe_3(thf)_3$ in thf (green), $(^{Ph}L)Fe_3(py)_3$ in benzene (red) and $(^{Ph}L)Fe_3(PMe_2Ph)_3$ in benzene (blue).

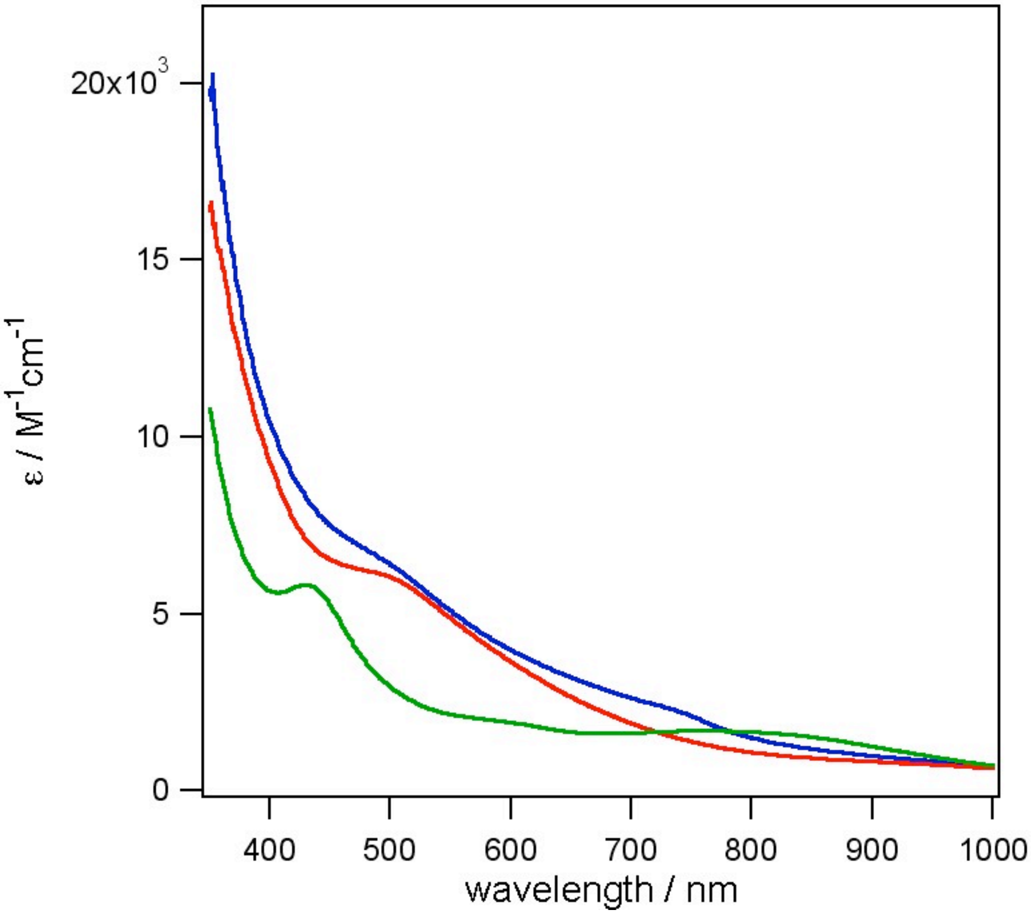

Figure A2. Variable-temperature magnetic susceptibility data for $(^{Ph}L)Fe_3(PMe_2Ph)_3$ collected under a field of 1 T. The solid lines correspond to various simulations, as described in the text, with *J* given in cm^{-1}.

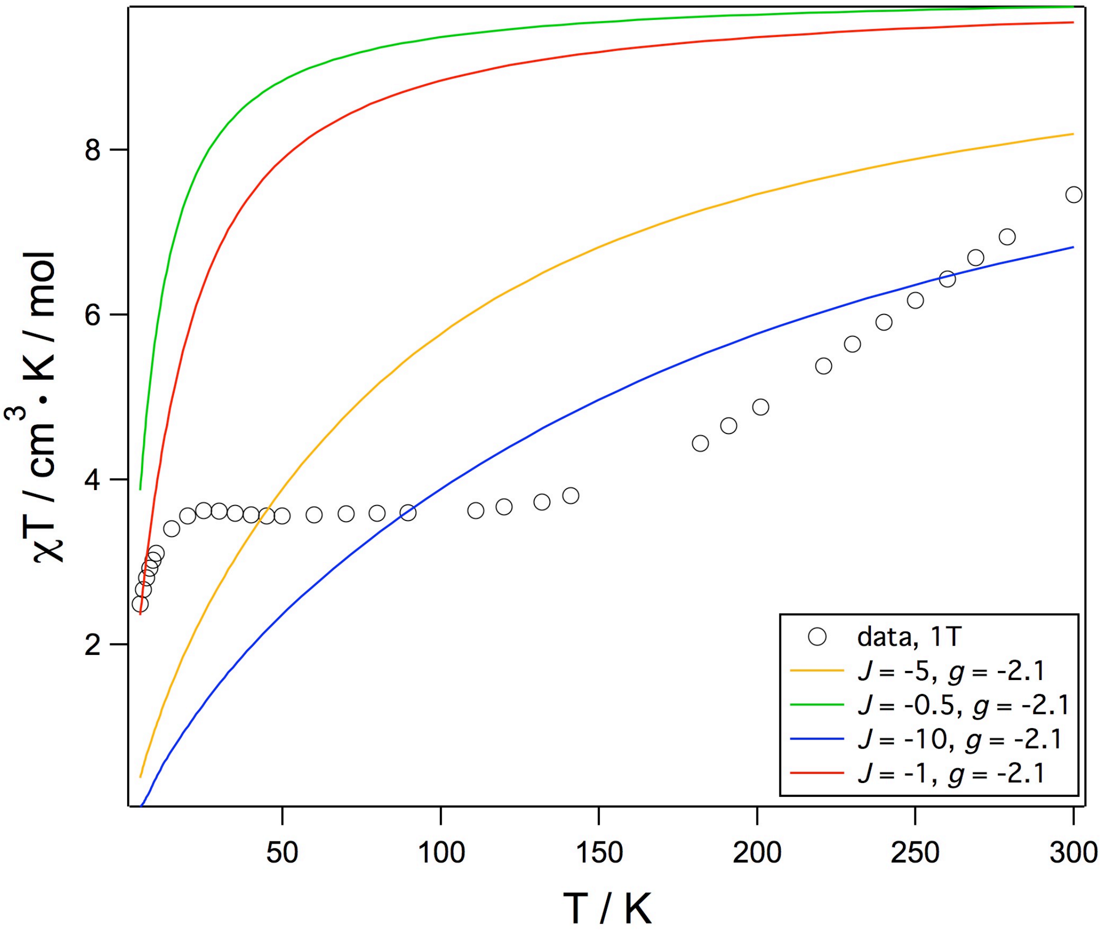

Figure A3. Variable-temperature magnetic susceptibility data for $(^{Ph}L)Fe_3(PMe_2Ph)_3$ collected under a field of 1 T. The solid lines correspond to various simulations, as described in the text, with J given in cm^{-1}.

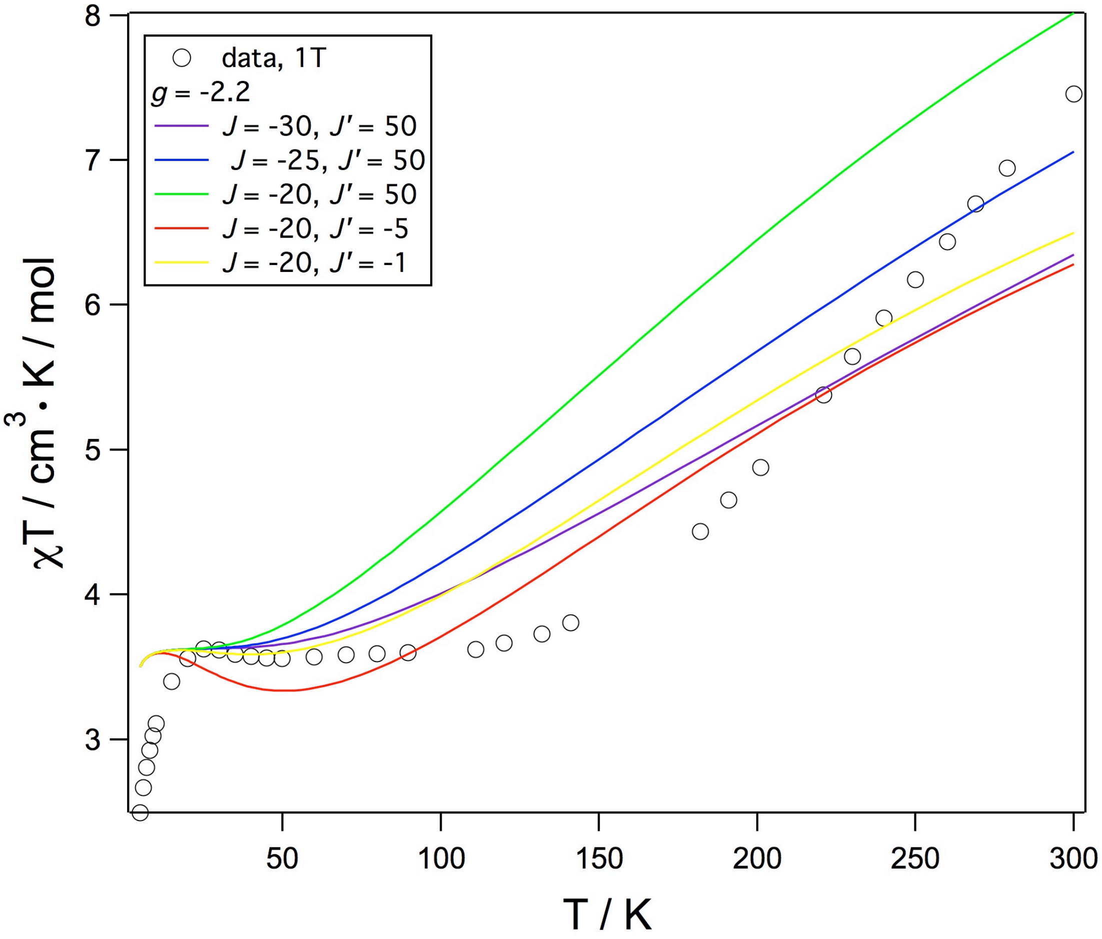

Figure A4. Variable-temperature magnetic susceptibility data for $(^{Ph}L)Fe_3(PMe_2Ph)_3$ collected under a field of 1 T. The solid lines correspond to various simulations, as described in the text, with *J* given in cm^{-1}.

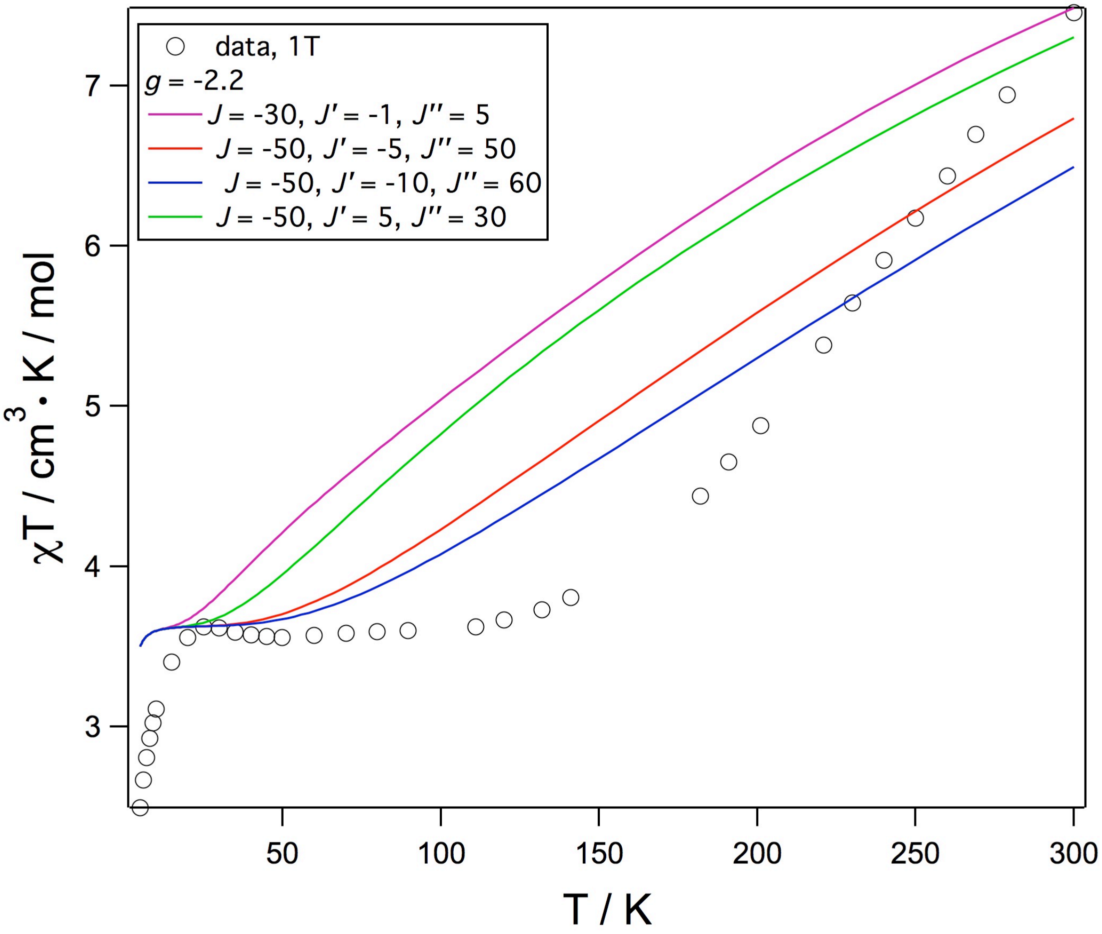

Appendix B: Supplementary Figures for Chapter 3

Figure B1. UV-vis spectra of $[(^{Ph}L)Fe_3(\mu\text{-}Cl)]_2$ in thf (green) and $(^{Ph}L)Fe_3I(thf)$ in thf (purple). Complex **3** is expected to be in a monomeric thf-bound form in thf solution. Near-IR studies reveal no additional bands between 1000-1500 nm.

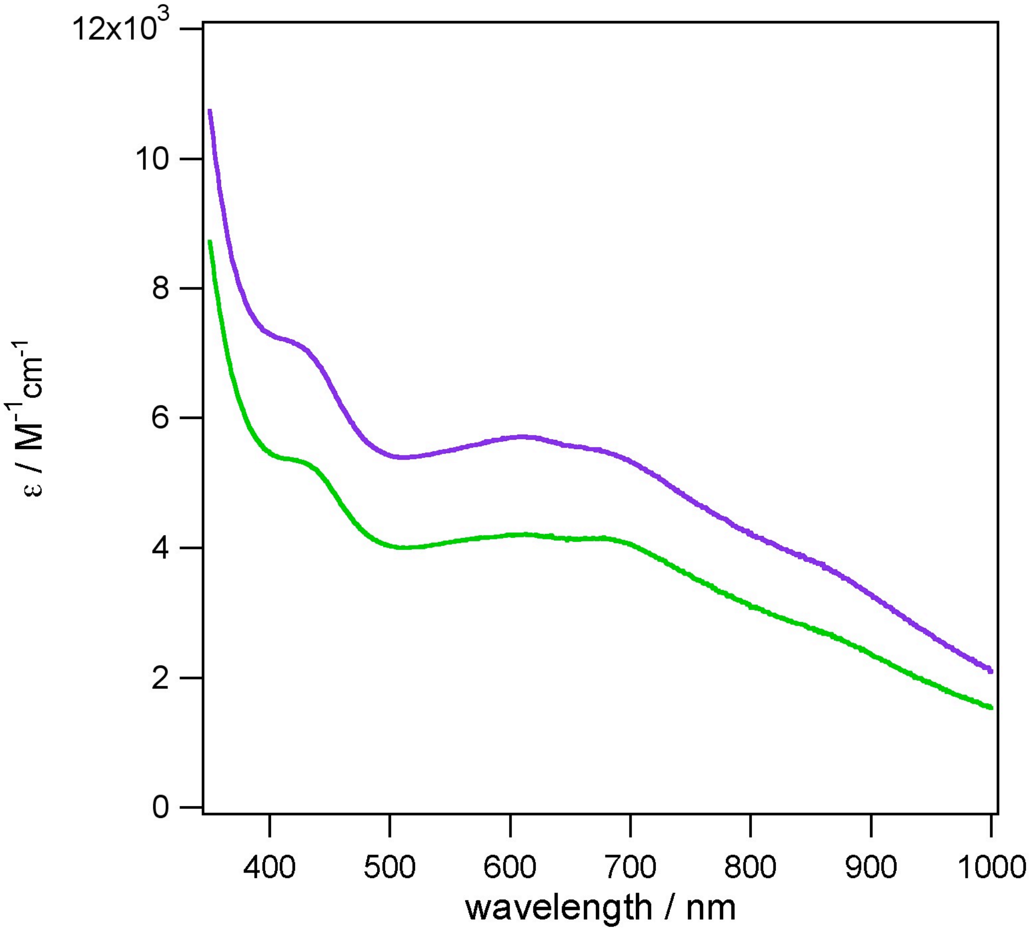

Figure B2. Zero-field ^{57}Fe Mössbauer spectrum of (^{Ph}L)Fe$_3$Cl(py). Simulation yields the following parameters: (blue, 33.3%) $\delta = 0.23$ mm/s, $\Delta E_Q = 2.86$ mm/s, $\gamma = 0.14$ mm/s; (green, 33.3%) $\delta = 0.29$ mm/s, $\Delta E_Q = 2.43$ mm/s, $\gamma = 0.14$ mm/s; (gold, 33.3%) $\delta = 0.80$ mm/s, $\Delta E_Q = 1.60$ mm/s, $\gamma = 0.13$ mm/s.

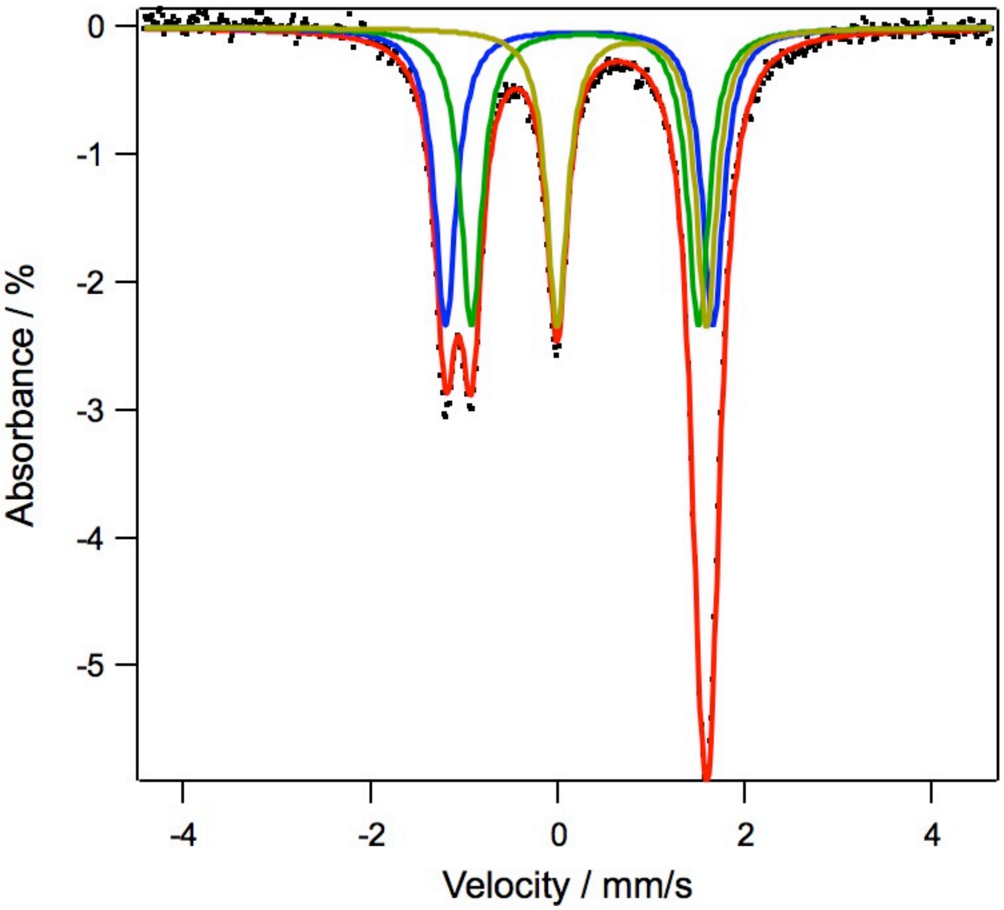

Figure B3. Zero-field ^{57}Fe Mössbauer spectrum of $[(^{Ph}L)Fe_3(\mu\text{-}Cl)]_2$. Simulation yields the following parameters: (blue, 33.3%) δ = 0.22 mm/s, ΔE_Q = 2.72 mm/s, γ = 0.14 mm/s; (green, 33.3%) δ = 0.26 mm/s, ΔE_Q = 2.43 mm/s, γ = 0.23 mm/s; (gold, 33.3%) δ = 0.79 mm/s, ΔE_Q = 1.54 mm/s, γ = 0.18 mm/s.

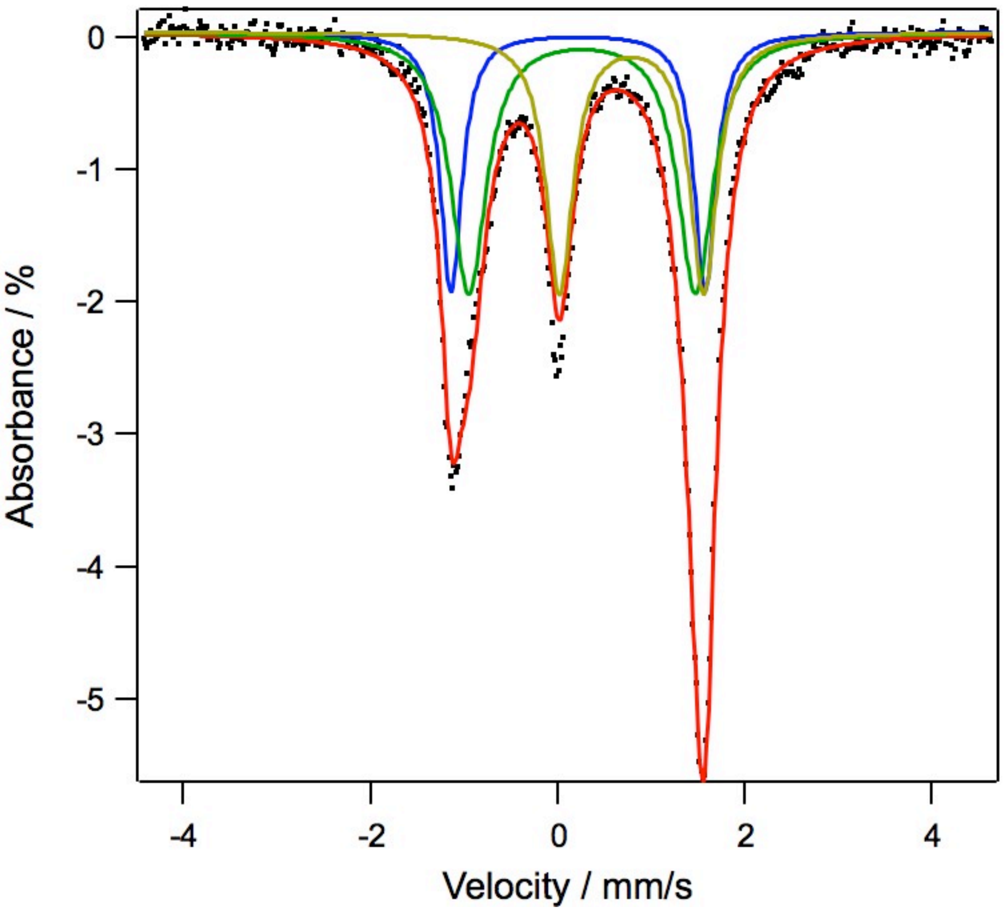

Figure B4. Zero-field ^{57}Fe Mössbauer spectrum of (^{Ph}L)Fe$_3$Br(thf). Simulation yields the following parameters: (blue, 64.0%) $\delta = 0.26$ mm/s, $\Delta E_Q = 2.76$ mm/s, $\gamma = 0.18$ mm/s; (green, 36.0%) $\delta = 0.74$ mm/s, $\Delta E_Q = 1.67$ mm/s, $\gamma = 0.14$ mm/s.

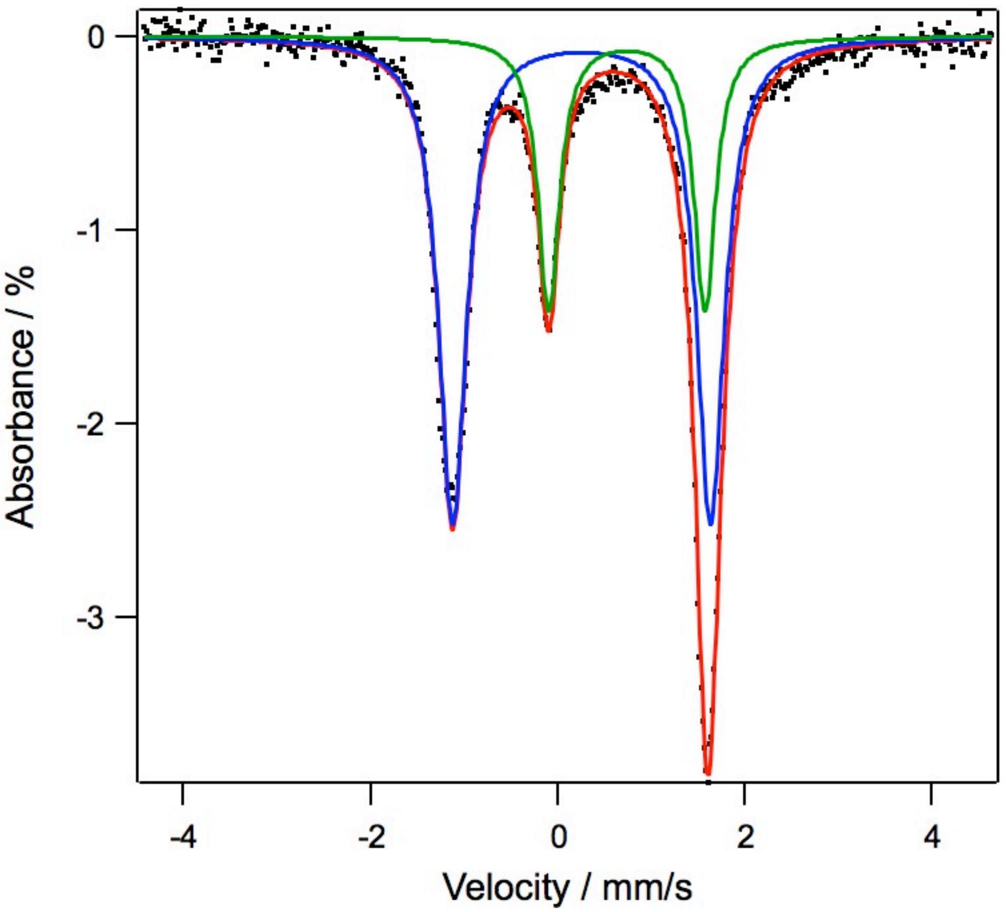

Figure B5. Zero-field ^{57}Fe Mössbauer spectrum of $[(^{Ph}L)Fe_3(\mu\text{-}Br)]_2$. Simulation yields the following parameters: (blue, 36.2%) δ = 0.22 mm/s, ΔE_Q = 2.76 mm/s, γ = 0.12 mm/s; (green, 31.9%) δ = 0.31 mm/s, ΔE_Q = 2.46 mm/s, γ = 0.13 mm/s; (gold, 31.9%) δ = 0.75 mm/s, ΔE_Q = 1.49 mm/s, γ = 0.14 mm/s.

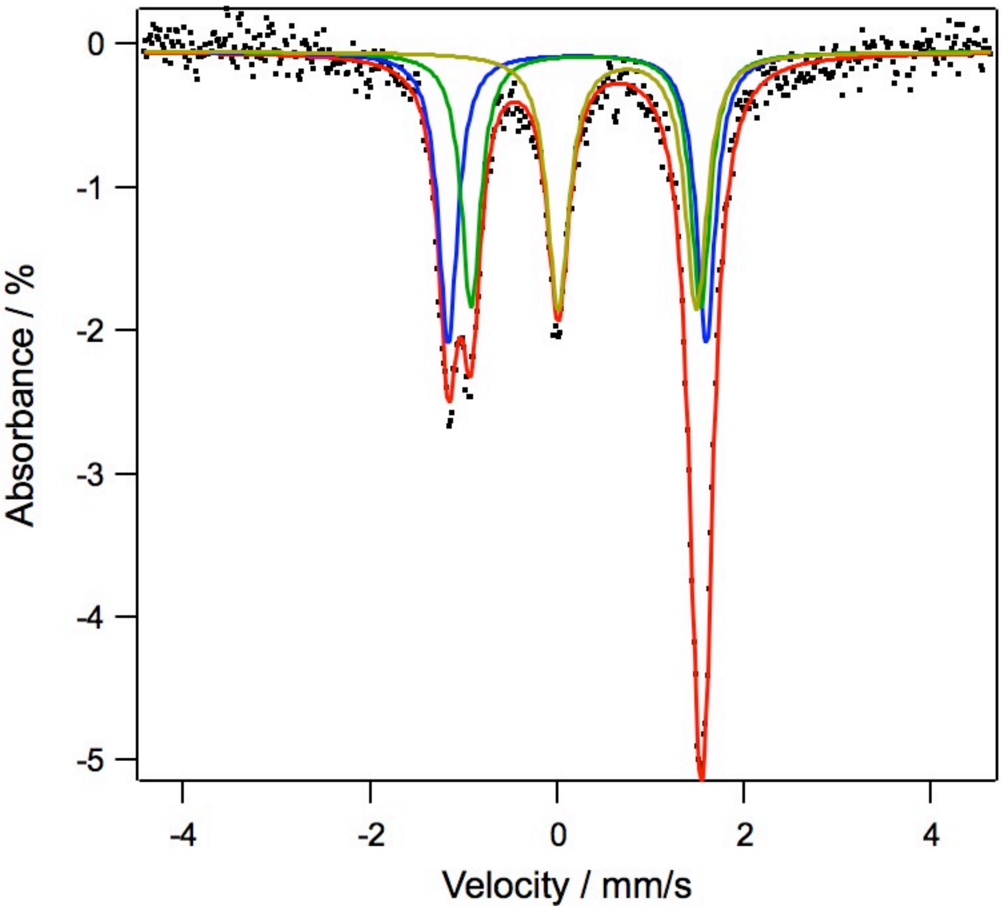

Figure B6. Zero-field ^{57}Fe Mössbauer spectrum of (^{Ph}L)Fe$_3$I(thf). Simulation yields the following parameters: (blue, 64.3%) $\delta = 0.22$ mm/s, $\Delta E_Q = 2.70$ mm/s, $\gamma = 0.15$ mm/s; (green, 35.7%) $\delta = 0.81$ mm/s, $\Delta E_Q = 1.74$ mm/s, $\gamma = 0.14$ mm/s.

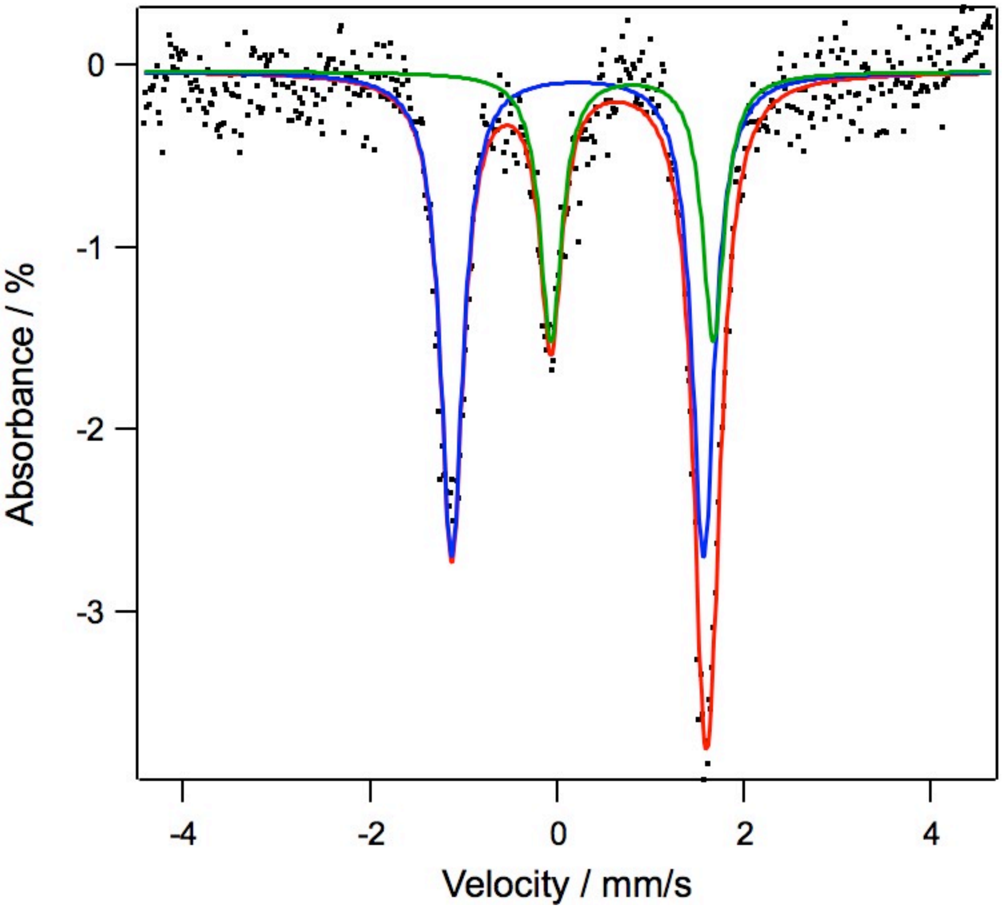

Appendix C: Supplementary Figures for Chapter 4

Figure C1. UV-vis spectra of $[(^{Ph}L)Fe_3(\mu\text{-}Cl)]_2$ (red), $(^{Ph}L)Fe_2CoCl(acn)$ (green), $(^{Ph}L)FeCo_2Cl(acn)$ (blue). All samples were prepared with a stock solution of 2.5% acetonitrile in benzene (wt/wt). Near IR studies reveal no additional bands between 1000-2400 nm.

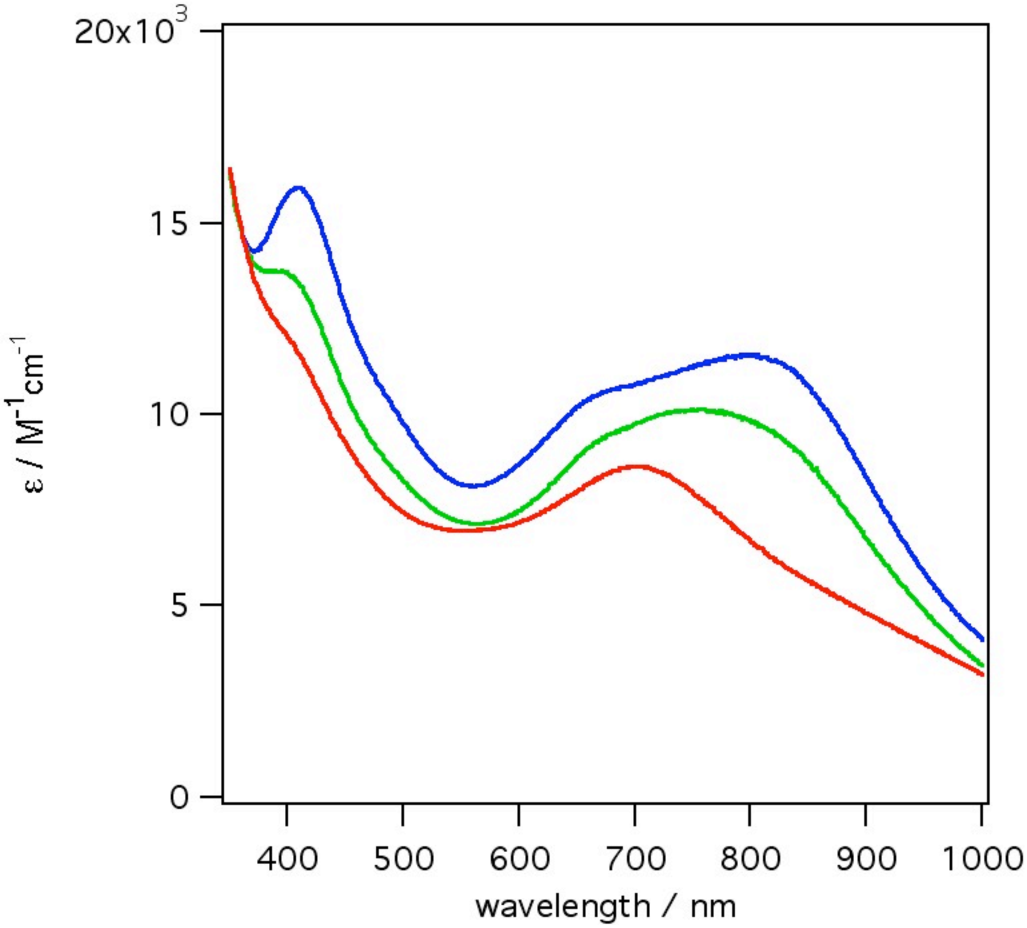

Figure C2. Zero-field ^{57}Fe Mössbauer spectrum of (^{Ph}L)FeCo$_2$Cl(acn). Simulation yields the following parameters: $\delta = 0.72$ mm/s, $\Delta E_Q = 1.05$ mm/s, $\gamma = 0.23$ mm/s.

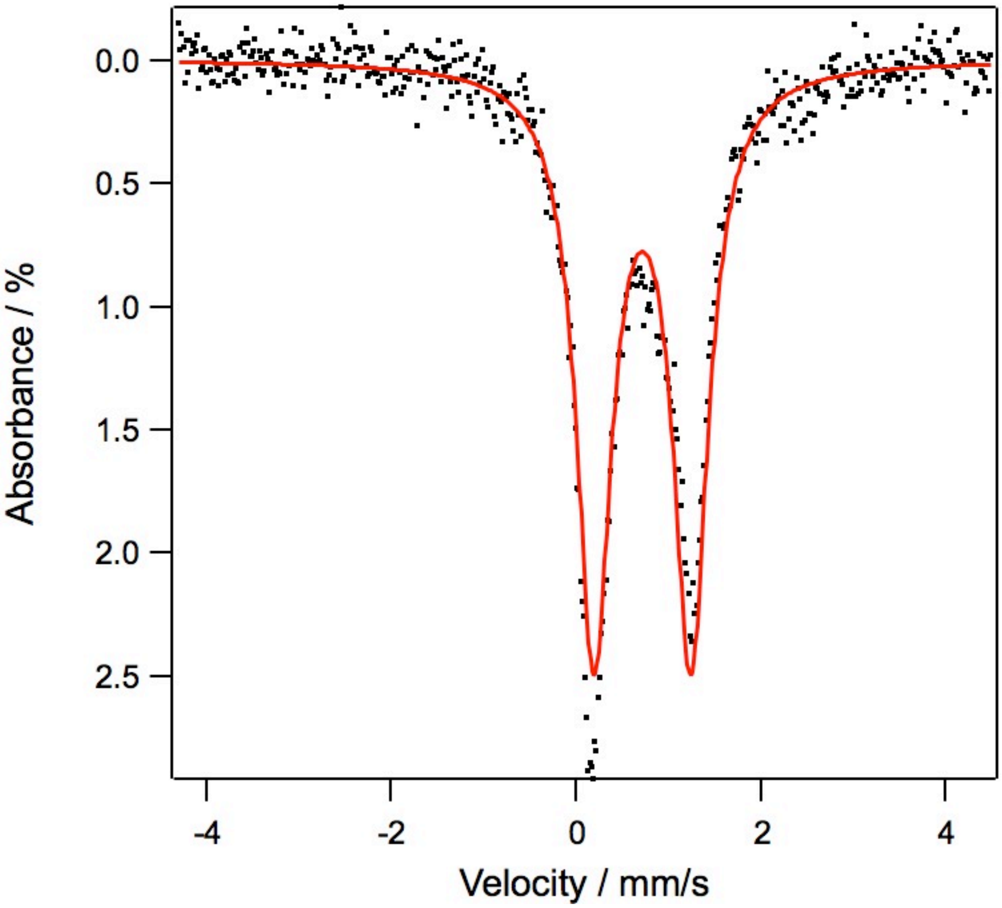

Figure C3. Calibration curve for Fe and Co quantification by X-ray fluorescence. Linear fit shown (y = 0.626x).

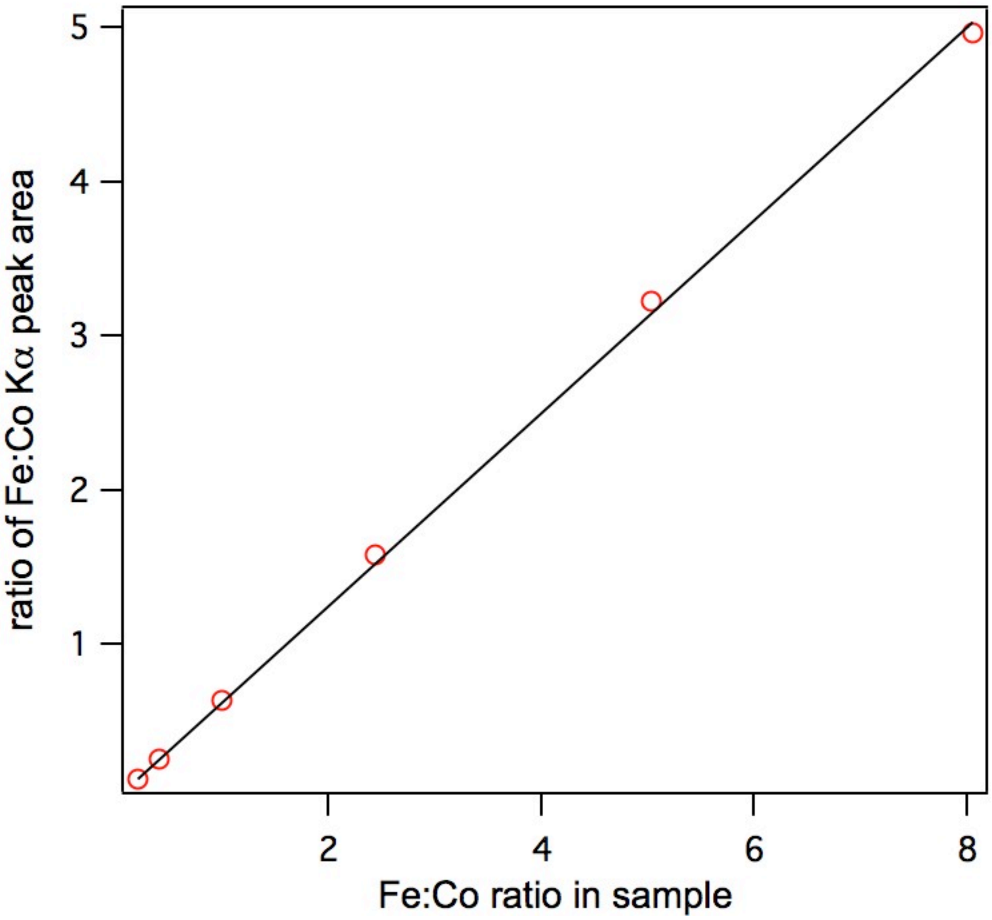

Figure C4. X-ray fluorescence spectrum of $(^{Ph}L)_2Fe_6Co(\mu\text{-}Cl)_4(thf)_2$. Data (black circles); fit (blue), Fe component of fit (dashed red), Co component of fit (dashed green).

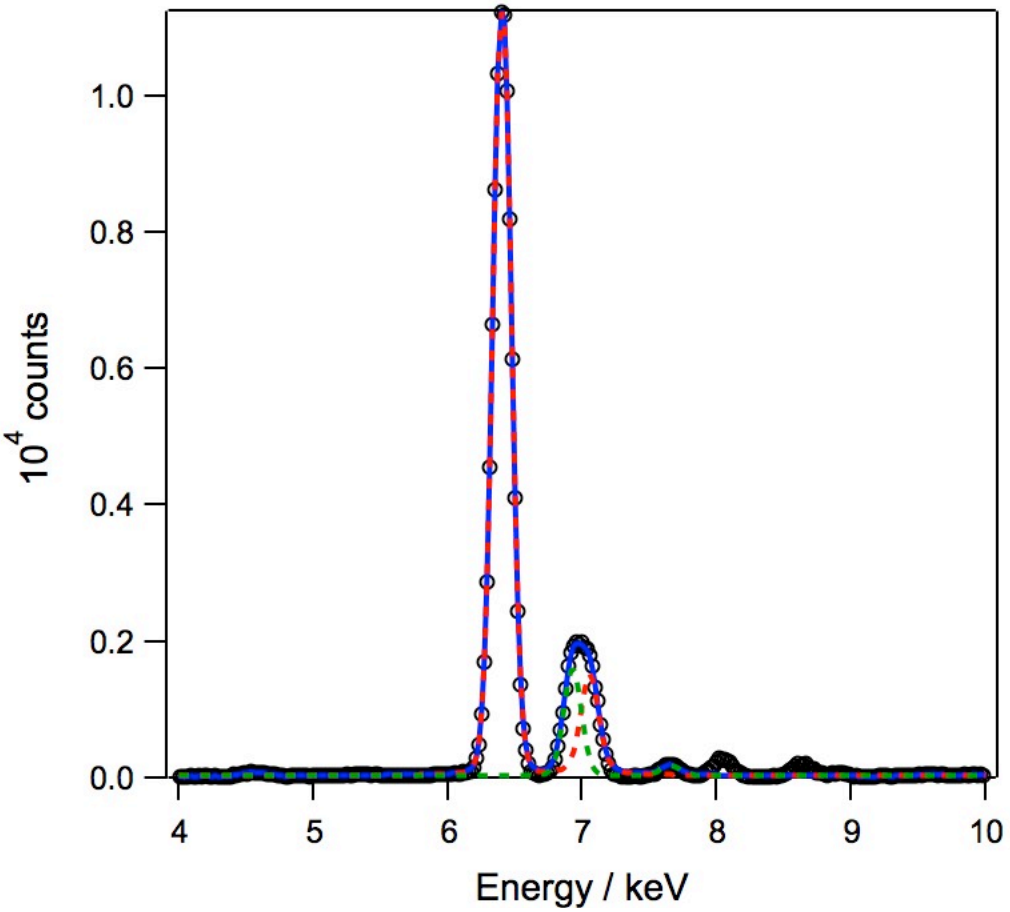

Figure C5. X-ray fluorescence spectrum of (^{Ph}L)Fe$_2$CoCl(acn). Data (black circles); fit (blue), Fe component of fit (dashed red), Co component of fit (dashed green).

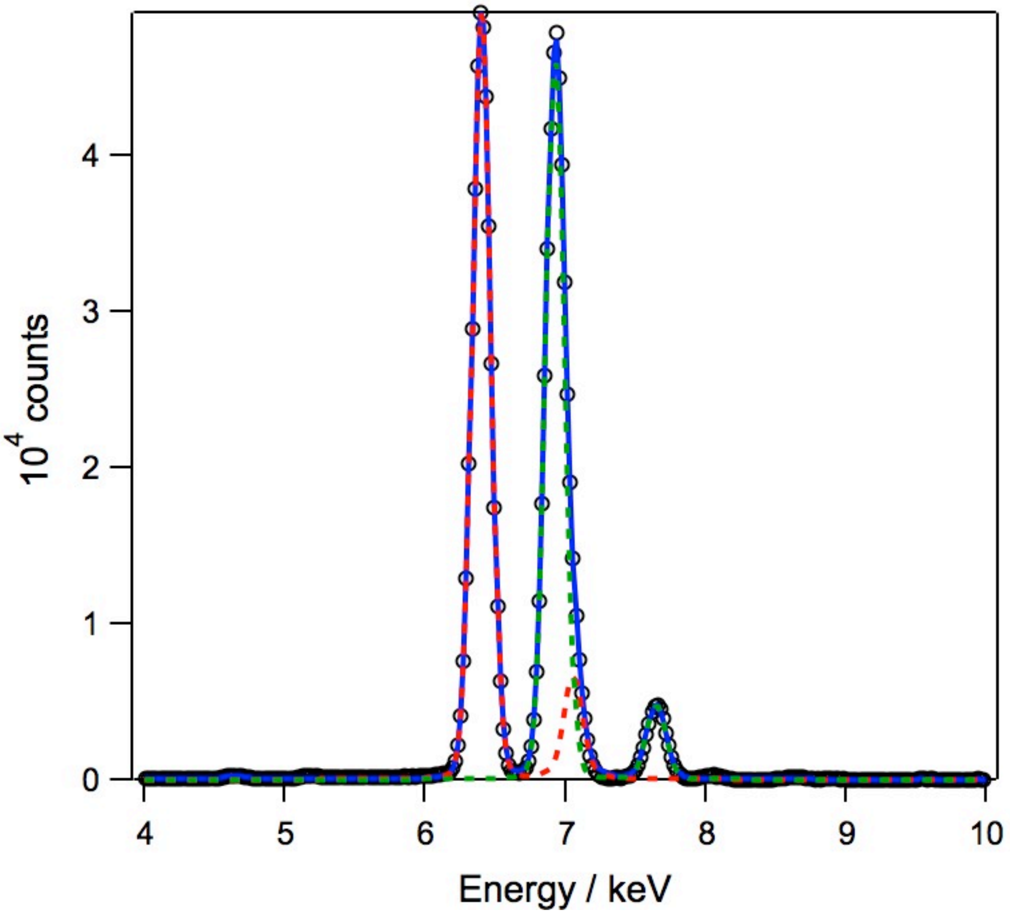

Figure C6. X-ray fluorescence spectrum of (^{Ph}L)FeCo$_2$Cl(acn). Data (black circles); fit (blue), Fe component of fit (dashed red), Co component of fit (dashed green).

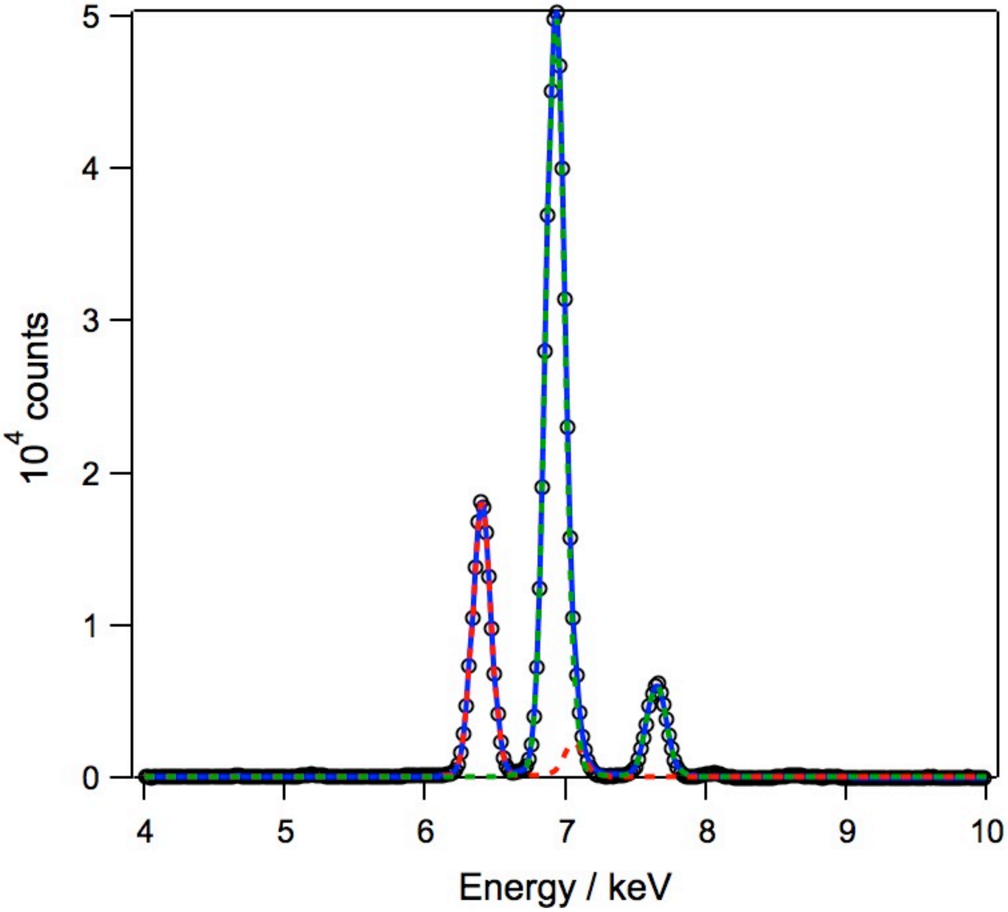

Figure C7. X-ray fluorescence spectrum of [(^{Ph}L)FeCo$_2$(μ-Cl)]$_2$. Data (black circles); fit (blue), Fe component of fit (dashed red), Co component of fit (dashed green).

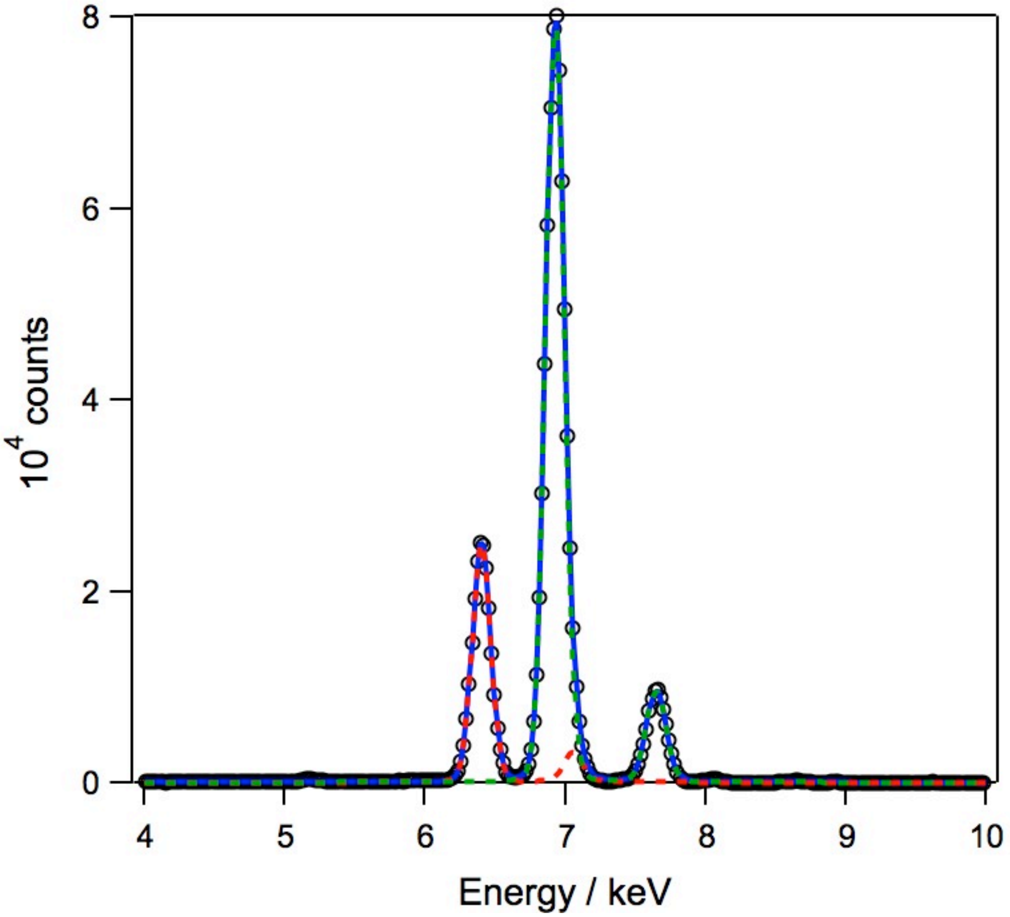

Figure C8. Variable-temperature magnetic susceptibility and reduced magnetization data for (^{Ph}L)FeCo$_2$Cl(acn) with simulation parameters chosen to optimize susceptibility fit ($\boldsymbol{S}_1 = 2$, $\boldsymbol{S}_2 = 1/2$, $J = -6.25$ cm^{-1}, $D_1 = 2.5$ cm^{-1}, $g = 2.35$ (susceptibility), $g = 2.16$ (reduced magnetization)).

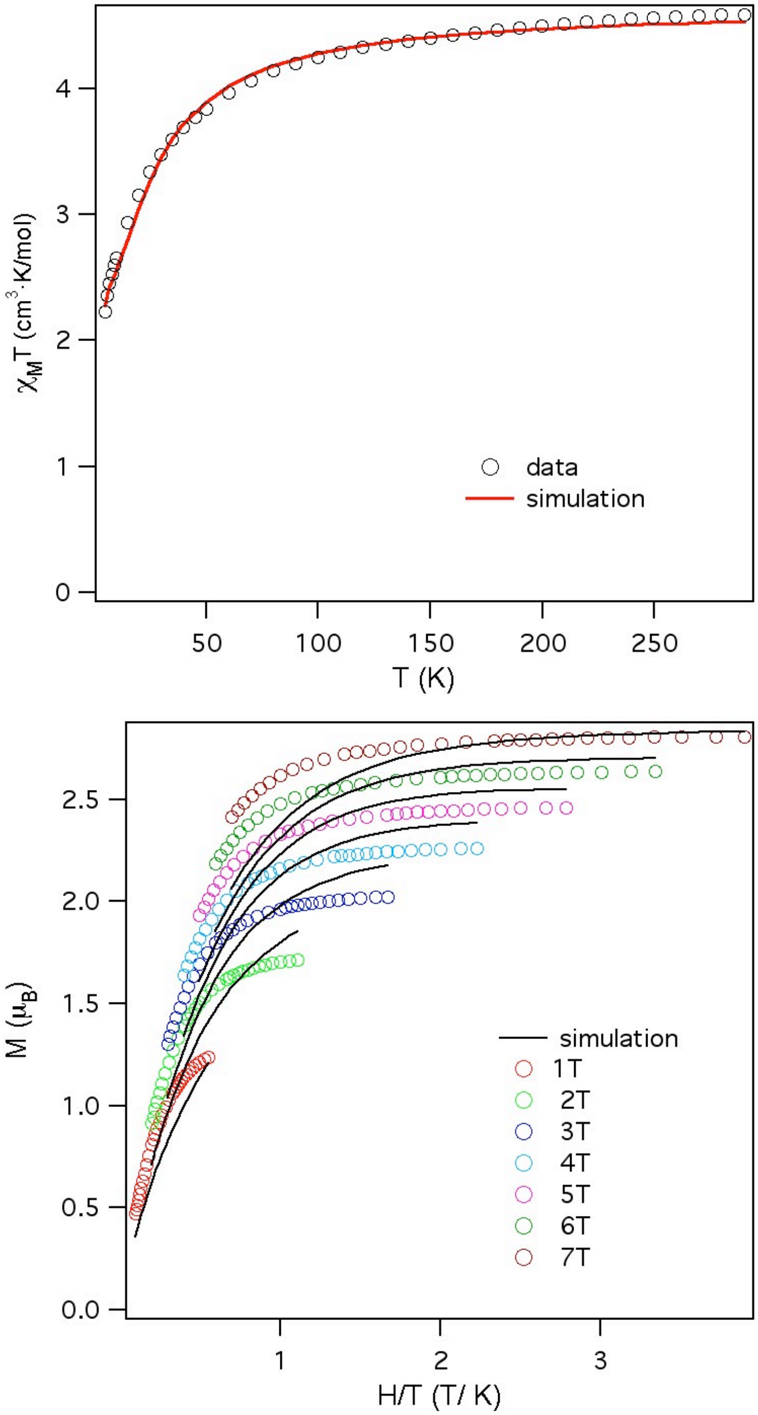

Figure C9. Zero-field ^{57}Fe Mössbauer spectrum of $(^{Ph}L)_2Fe_7(\mu\text{-}Cl)_4(thf)_2$ after stirring for 2.5 h with 0.5 eq ^{57}Fe-enriched $FeCl_2thf_2$. Simulation yields the following parameters: (blue, 35.4%) δ = 0.58 mm/s, ΔE_Q = 1.40 mm/s, γ = 0.22 mm/s; (green, 35.4%) δ = 0.19 mm/s, ΔE_Q = 2.66 mm/s, γ = 0.29 mm/s; (gold, 29.2%) δ = 1.16 mm/s, ΔE_Q = 2.11 mm/s, γ = 0.26 mm/s.